Dynamical decoupling in water-glycerol glasses: a comparison of nitroxides, trityl radicals and gadolinium complexes

Janne Soetbeer,[a] Marthe Millen,[a] Konstantin Zouboulis,[a] Miriam Hülsmann,[b] Adelheid Godt,[b] Yevhen Polyhach,[a] and Gunnar Jeschke*[a]

*gunnar.jeschke@phys.chem.ethz.ch
[a]Laboratory of Physical Chemistry, ETH Zürich, Vladimir-Prelog-Weg 2, CH-8093 Zürich, Switzerland.
[b]Bielefeld University, Department of Chemistry, Universitätsstr. 25, D-33615 Bielefeld, Germany.

1 Syntheses of nitroxides H-mNOPEG and D-mNOPEG

1.1 Scheme of the synthesis of iodide R^1-PEP_{R1}-I 2

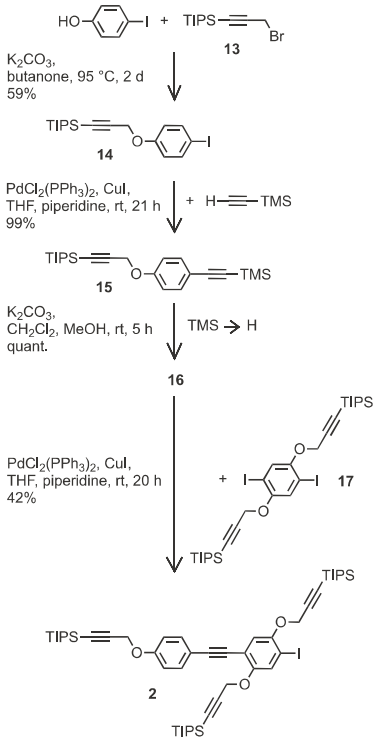

Figure Sa1 Assembly of iodide R^1-PEP_{R1}-I **2**.

1.2 Nomenclature

To denominate the compounds in the experimental part we use the following nomenclature: The 1,4-phenylene and ethynylene units are abbreviated with P and E, respectively. These letters are only used to describe the stiff, linear unit of the compounds. They have a different meaning in the established abbreviations PEG and TIPS. R^1, R^2 and R^3 denominate the substituents at benzene rings. These substituents are shown in Fig. 2 of the main manuscript. P_{R1} stands for a benzene ring with two substituents of type R^1 in 2- and 6-position. NO• denominates the nitroxide moiety including the atoms linking the nitroxide moiety to the benzene ring.

1.3 Experimental part

1.3.1 General

Unless otherwise stated, reactions were performed under argon and in case of the syntheses of alkyne H-EP-NO• **3** and nitroxide D-mNOPEG **D-1** in dried glassware, using the Schlenk technique. The argon (4.6 technical grade) was passed through anhydrous $CaCl_2$ prior to its use. Solutions were degassed through several freeze-pump-thaw cycles. For reactions, commercially available solvents and reagents were used as obtained: 4-ethynylaniline, > 98%, obtained from TCI; 3-carbamoyl-2,2,5,5-tetramethyl-3-pyrrolin-1-oxyl, > 99%, obtained from Alfa Aesar; anhydrous THF, CH_2Cl_2, and toluene over molecular sieve was obtained from Acros. The solvents used for extraction and chromatography were of technical grade and were distilled prior to their use. $PdCl_2(PPh_3)_2$ was synthesized according to literature,[1] however using 2.1 times the given amount of methanol. Perdeuterated 3-carbamoyl-2,2,5,5-tetramethyl-3-pyrrolin-1-oxyl was provided by H. Zimmermann. The starting compounds (3-bromoprop-1-yn-1-yl)triisopropylsilane

(**13**), diiodobenzene **14** (I-P_{R1}-I, R1 = $OCH_2CCTIPS$), and PEG-N_3 **6** were obtained as described elsewhere.[2] As reported,[2] (3-bromoprop-1-yn-1-yl)triisopropylsilane was obtained in mixture with hept-1-ynyltriisopropylsilane. The latter is of no concern in the use of (3-bromoprop-1-yn-1-yl)triisopropylsilane (**13**) described herein.
Temperatures reported for the reactions refer to the bath temperatures. Solvents were removed at a bath temperature of ca. 40 °C and reduced pressure. The products were dried at room temperature at ca. 0.05 mbar. The ratio of the components in a mixture was determined by ^{1}H NMR spectroscopy and is given in a molar ratio.
Column chromatography was carried out on silica gel 60 M (Macherey Nagel) applying slight pressure. The size of the silica gel column is given as diameter × length. The material was loaded onto the column dissolved in a small quantity of the eluent, if no other information is given. Thin layer chromatography (TLC) was performed on silica gel coated aluminum foil (Merck, 60 F254). The spots were detected with UV light of $\lambda = 254$ and 366 nm. The compositions of solvent mixtures are given in volume ratios. ^{1}H NMR and ^{13}C NMR spectra were calibrated using the solvent signal as an internal standard [$CDCl_3$: $\delta(^1H) = 7.25$, $\delta(^{13}C\{^1H\}) = 77.00$; CD_2Cl_2: $\delta(^1H) = 5.32$, $\delta(^{13}C\{^1H\}) = 53.80$]. Signal assignments are supported by DEPT-135, HMBC and HMQC spectra. ESI mass spectra were recorded using an Esquire 3000 ion trap mass spectrometer (Bruker Daltonik GmbH, Bremen, Germany) equipped with a nano-ESI source. ESI accurate mass measurements were acquired using an Agilent 6220 time-of-flight mass spectrometer (Agilent Technologies, Santa Clara, CA, USA) in extended dynamic range mode equipped with a Dual-ESI source or using a Q-IMS-TOF mass spectrometer Synapt G2Si (Waters GmbH, Manchester, UK) in resolution mode interfaced to a nano-ESI ion source.

1.3.2 Syntheses of building blocks H-11, D-11, and 3

Perdeuterated 2,2,5,5-tetramethyl-3-pyrrolin-1-oxyl-3-carboxylic acid (D-11). We used experimental procedures of Oyaizu *et al.*[3] and Kirilyuk *et al.*[4] as guidelines. HPLC was used to proof the purity. Perdeuterated 3-carbamoyl-2,2,5,5-tetramethyl-3-pyrrolin-1-oxyl (53.4 mg, 0.272 mmol) was suspended in aqueous NaOH solution (10 wt%; 800 μL, 22.2 mmol) and the suspension was stirred at 120 °C for 3 h at ambient atmosphere. The yellow solution was diluted with water and washed with Et_2O. The organic phase was discarded. The pH of the aqueous phase was brought to 2 through addition of an aqueous solution of $NaHSO_4$ (10 wt%, 3 mL). Then Et_2O was added. The phases were separated, and the aqueous phase was extracted with Et_2O. The organic phases which had been obtained during extraction of the acidic aqueous phase with Et_2O, were combined, washed with water, dried over $MgSO_4 \bullet x\ H_2O$, and filtered. The solvents were removed from the filtrate providing perdeuterated 2,2,5,5-tetramethyl-3-pyrrolin-1-oxyl-3-carboxylic acid (**D-11**) (43.7 mg, 81%) as a pale yellow solid. Analytical HPLC: retention time 4.4 min (HPLC-column: Luna® Silica (2) Phenomenex, particle size 5 μm, pore size 100 Å, length 250 mm, internal diameter 4.6 mm; elution: room temperature, flow rate 1.0 mL/min, linear gradient: CH_2Cl_2/EtOH: 0-10 min 10% EtOH, 10-20 min 10%→20%, 20-30 min 20%→40%; detection: UV at 210 nm).

2,2,5,5-Tetramethyl-3-pyrrolin-1-oxyl-3-carboxylic acid (H-11). Spin label **H-11** was synthesized in the same way as the perdeuterated spin label **D-11** starting from 3-carbamoyl-2,2,5,5-tetramethyl-3-pyrrolin-1-oxyl. Analytical HPLC: retention time 4.6 min (HPLC-column: Luna® Silica (2) Phenomenex, particle size 5 μm, pore size 100 Å, length 250 mm, internal diameter 4.6 mm; elution: room temperature, flow rate 1.0 mL/min, linear gradient: CH_2Cl_2/EtOH: 0-10 min 10% EtOH, 10-20 min 10%→20%, 20-30 min 20%→40%; detection: UV at 210 nm). For comparison the starting compound 3-carbamoyl-2,2,5,5-tetramethyl-3-pyrrolin-1-oxyl was eluted at 7.7 min. Comment on the analysis of spin label **H-11**: We tested the option of compound identification through ^{1}H NMR spectroscopy after addition of a mild reducing agent for converting the nitroxide radical into a hydroxylamine. Experiments with $SnCl_2$ in aqueous acetone revealed an extremely slow reaction, being incomplete even after 21 h at room temperature. 1,2,3,4,5-Pentafluorophenylhydrazine in in chloroform provided a mixture of products. $Na_2S_2O_4$ in aqueous acetone worked best, however the reaction needed a little more than 50 min at room temperature (no further more detailed experiments were performed) and at a much longer reaction time of 21 h a side reaction became obvious.

H-EP-NO• 3. We applied a procedure described for structurally closely related compounds.[5,6] 2,2,5,5-Tetramethyl-3-pyrrolin-1-oxyl-3-carboxylic acid (**H-11**) (144 mg, 0.782 mmol) and DMAP (220 mg, 1.80 mmol) were dissolved in anhydrous CH_2Cl_2 (5 mL) and the yellow solution was cooled with an icebath. $SOCl_2$ (55.0 μL, 0.758 mmol) was added, whereupon the solution immediately changed its color from yellow to orange-red. After stirring the solution at room temperature for 45 min, a solution of 4-ethynylaniline (46 mg, 0.393 mmol) in anhydrous CH_2Cl_2 (2 mL) was added and the orange solution was stirred at room temperature for 50 min. Then it was filtered through silica gel (2 cm × 3 cm, rinsing with CH_2Cl_2/Et_2O 25:1). The solvent was removed from the eluate. Column chromatography (1.5 cm × 25 cm, CH_2Cl_2/Et_2O 25:1; compound was loaded onto the silica gel column as a solution in $CDCl_3$) of the residual orange oil gave H-EP-NO• **3** (110 mg, 99%; R_f = 0.11) as a yellow solid. ^{1}H NMR (500 MHz, CD_2Cl_2): δ 7.54 (broad and featureless "s" with shoulder, 4 H, H_{Ar}), 3.10 (s, 1 H, C≡CH). ^{13}C NMR (126 MHz, CD_2Cl_2): δ 132.4 (C_{Ar}H *meta* to N), 121.0 (C_{Ar}H *ortho* to N), 118.1 ($\underline{C}_{Ar}C\equiv C$), 82.5 (C≡$\underline{C}$H), 77.1 ($\underline{C}\equiv$CH).

1.3.3 Synthesis of iodide 2

(3-(4-Iodophenoxy)prop-1-yn-1-yl)triisopropylsilane (R^1-P-I, 14) K_2CO_3 (980 mg, 7.09 mmol) was suspended in a solution of 4-iodophenol (759 mg, 3.45 mmol) and a mixture (969 mg) of (3-bromoprop-1-yn-1-yl)triisopropylsilane

(**13**; 3.13 mmol) and hept-1-ynyltriisopropylsilane (0.42 mmol) in butanone (100 mL). The suspension was stirred at 95 °C for 43 h. After the brown-orange suspension had cooled down to room temperature, it was filtered through silica gel (4.5 cm × 4 cm, rinsing with Et_2O (100 mL)). The solvent was removed from the eluate. Column chromatography (3 cm × 28 cm, ca. 600 mL pentane, then pentane/Et_2O 30:1) of the brown liquid residue gave R^1-P-I **14** (613 mg, 47%; R_f = 0.50) as a colorless liquid. A later eluted fraction (388 mg of yellow liquid) contained also R^1-P-I **14**. This latter fraction was submitted to column chromatography with pentane/Et_2O 50:1 and a subsequent column chromatography with pentane/CH_2Cl_2 50:1. Only with the last column chromatography the unidentified by-component was removed and additional R^1-P-I **14** (165 mg, 12%) was obtained as a colorless liquid. For ^1H and ^{13}C NMR data, see Tables Sa1 and Sa2. Accurate MS (EI): m/z calcd for $[M]^+$ $C_{18}H_{27}IOSi^+$, 414.08704; found, 414.08688.

Triisopropyl(3-(4-((trimethylsilyl)ethynyl)phenoxy)prop-1-yn-1-yl)silane (R^1-PE-TMS, 15). To a degassed solution of R^1-P-I **14** (730 mg, 1.76 mmol) and trimethylsilylethyne (370 µL, 2.67 mmol) in THF (25 mL) and piperidine (5 mL, 51 mmol) were added $PdCl_2(PPh_3)_2$ (25 mg, 0.036 mmol) and CuI (13 mg, 0.068 mmol). After stirring the reaction mixture at room temperature for 21 h, Et_2O and then water were added. The phases were separated, and the aqueous phase was extracted with Et_2O. The combined organic phases were washed with 2 N HCl and brine, dried over $MgSO_4$ • x H_2O, and filtered. The solvents of the filtrate were removed. Column chromatography (2.5 cm × 28 cm, pentane/Et_2O 50:1) gave R^1-PE-TMS **15** (671 mg, 99%; R_f = 0.33) as a yellow oil. For ^1H and ^{13}C NMR data, see Tables Sa1 and Sa2. Accurate MS (EI): m/z calcd for $[M]^+$ $C_{23}H_{36}OSi_2{}^+$, 384.22992; found, 384.22861.

(3-(4-Ethynylphenoxy)prop-1-yn-1-yl)triisopropylsilane (R^1-PE-H, 16). K_2CO_3 (33 mg, 0.24 mmol) was added to a solution of R^1-PE-TMS **15** (60 mg, 0.156 mmol) in CH_2Cl_2 (7.0 mL) and methanol (7.0 mL). The suspension was stirred at room temperature for 5 h. Filtration through silica gel (2 cm × 5 cm, rinsing with Et_2O (12 mL)) gave R^1-PE-H **16** in mixture with a trace of TMS-OH/-F as a colorless film (51 mg) in the flask. This material was used as obtained. For ^1H NMR data, see Table Sa1.

R^1-PEPR^1-I 2 (iodide 2). To a degassed solution of diiodobenzene I-P_{R1}-I **17** (167 mg, 0.222 mmol) and the material that had been obtained through TMS removal from R^1-PE-TMS **15** (44 mg, containing max. 0.133 mmol R^1-PE-H **16**) in THF (5 mL) and piperidine (1 mL, 10.1 mmol) were added $PdCl_2(PPh_3)_2$ (2.4 mg, 3.4 µmol) and CuI (1.2 mg, 6.3 µmol). After stirring the yellow solution, which turned into a suspension over time, at room temperature for 20 h, all volatiles were removed at room temperature and reduced pressure. The residue was taken up in Et_2O and filtered through silica gel (2 cm × 2 cm, rinsing with Et_2O (10 mL)). Removal of the solvent from the eluate gave an orange-brown oil. Column chromatography (2 cm × 33 cm, pentane/CH_2Cl_2 10:4) of this oil gave diiodobenzene I-P_{R1}-I **17** (85 mg, 51%; R_f = 0.57) as a slightly yellowish solid, a yellow-orange oil (63 mg; R_f = 0.40) consisting mainly of R^1-PEP$_{R1}$-I **2**, and the dicoupling product R^1-PEP$_{R1}$EP-R^1 (11 mg, 4% referring to diiodobenzene I-P_{R1}-I **17**; R_f = 0.20) as a yellow film in the flask. Column chromatography (2 cm × 30 cm, pentane/CH_2Cl_2 10:3) of the yellow-orange oil gave R^1-PEP$_{R1}$-I **2** (53 mg, 42% referring to R^1-PE-H **16**; R_f = 0.22) as a colorless oil. Analytical data of R^1-PEP$_{R1}$-I **2**: for ^1H and ^{13}C NMR data, see Tables Sa1 and Sa2. Accurate MS (ESI): m/z calcd for $[M + Na]^+$ $C_{50}H_{75}O_3Si_3INa^+$, 957.39609; found, 957.3951. Analytical data of dicoupling product R^1-PEP$_{R1}$EP-R^1: for ^1H and ^{13}C NMR data, see Tables Sa1 and Sa2. Accurate MS (ESI): m/z calcd for $[M + Na]^+$ $C_{70}H_{102}O_4Si_4Na^+$, 1141.67474; found, 1141.6727.

1.3.4 Protonated nitroxide H-mNOPEG (H-1)

R^1-PEP$_{R1}$EP-NO• 4. To a degassed solution of R^1-PEP$_{R1}$-I **2** (75 mg, 0.080 mmol) and H-EP-NO• **3** (24.5 mg, 0.086 mmol) in THF (3 mL) and piperidine (0.5 mL, 5.0 mmol) were added $PdCl_2(PPh_3)_2$ (2.3 mg, 3.3 µmol) and CuI (1.3 mg, 6.8 µmol). After stirring the reaction mixture for 18 h at room temperature, all volatiles were removed from the suspension at room temperature and reduced pressure. The residue was taken up in Et_2O and filtered through silica gel (2 cm × 4 cm, rinsing with Et_2O (10 mL)). The solvent was removed from the eluate. Column chromatography (2 cm × 32 cm, CH_2Cl_2/Et_2O 25:1) gave R^1-PEP$_{R1}$EP-NO• **4** (52 mg, 59%; R_f = 0.34) as a yellow film. For ^1H and ^{13}C NMR data, see Tables Sa1 and Sa2. Accurate MS (ESI) obtained from a subsequently eluted chromatographic fraction which shows the same thin layer chromatogram and ^1H NMR spectrum as the earlier eluted fraction: m/z calcd for $[M + Na]^+$ $C_{67}H_{93}N_2O_5Si_3Na^+$, 1112.62845; found, 1112.6282.

R^2-PEP$_{R2}$EP-NO• 5. R^1-PEP$_{R1}$EP-NO• **4** (52 mg, 0.048 mmol) was dissolved in THF (5 mL) and n−Bu_4NF (1 M in THF; 172 µL, 0.172 mmol) was added whereupon the reaction solution immediately changed its color from pale yellow to yellow-brown. The solution was stirred at room temperature for 10 min. The solution was filtered through silica gel (2 cm × 4 cm, rinsing with THF (12 mL)). Removal of the solvent from the eluate gave a beige solid (32 mg) consisting of R^2-PEP$_{R2}$EP-NO• **5**, TIPS-OH/-F, Bu_4NX (X = F, OH), and THF. This material was used as obtained. For ^1H NMR data of R^2-PEP$_{R2}$EP-NO• **5**, see Table Sa3.

H-mNOPEG (R^3-PEP$_{R3}$EP-NO•, H-1). To a degassed suspension of PEG-N_3 **6** (72.6 mg, 0.171 mmol) and the material that had been obtained through desilylation of R^1-PEP$_{R1}$EP-NO• **4** (32 mg, containing max. 0.048 mmol of R^2-PEP$_{R2}$EP-NO• **5**) in anhydrous toluene (8 mL) was added $[Cu(phen)(PPh_3)_2]NO_3$•0.5 CH_2Cl_2 (2.897 mg, 3.5

μmol). The reaction mixture was stirred for 43 h at 40 °C. The yellow-brown solution was exposed to air for 2 h at room temperature for oxidation of possibly formed[5] hydroxylamine. Then, the flask was filled with argon and metal scavenger QuadraPure TU (70 mg) was added. The suspension was stirred for 20 h at room temperature. Metal scavenger QuadraPure BzA (5 mg) was added, and the suspension was stirred for another 2 h at room temperature. The suspension was filtered through silica gel (2 cm × 3 cm, rinsing with CH_2Cl_2/EtOH 5:1 (10 mL)). The solvent was removed from the eluate. Preparative HPLC (HPLC-column: Luna® Silica (2) Phenomenex, particle size 5 μm, pore size 100 Å, length 250 mm, internal diameter 21.2 mm; elution: room temperature, flow rate 15 mL/min, linear gradient: CH_2Cl_2/EtOH: 0-10 min 5% EtOH, 10-20 min 5%→10%, 20-30 min 10%→20%, 30-40 min 20%; detection: UV at 220 nm; the eluate between 15.1 min and 20.1 min was collected) gave R^3-PEP$_{R3}$EP-NO• (H-mNOPEG, **H-1**) (65 mg, 71% referring to R^1-PEP$_{R1}$EP-NO• **4**) as a yellow film. For ^{1}H and ^{13}C NMR data, see Tables ZSa3a,b. Accurate MS (ESI): m/z calcd for $[M + 2H]^{2+}$ $C_{94}H_{144}N_{11}O_{29}H_{22}^+$, 946.51385; found, 946.51140.

1.3.5 Perdeuterated nitroxide D-mNOPEG (D-1)

R^1-PEP$_{R1}$EP-NH$_2$ 8. To a degassed solution of R^1-PEP$_{R1}$-I **2** (59.8 mg, contaminated with silicon grease and unidentified compounds; for ^{1}H NMR spectrum see Supporting Information Part B; containing max. 0.057 mmol of R^1-PEPR^1-I 2) and 4-ethynylaniline (**7**) (7.4 mg, 0.063 mmol) in THF (2 mL) and piperidine (0.5 mL, 5.0 mmol) were added $PdCl_2(PPh_3)_2$ (1.326 mg, 1.9 μmol) and CuI (0.761 mg, 4.0 μmol). After stirring the reaction mixture for 24 h at room temperature, all volatiles were removed from the suspension at room temperature and reduced pressure. Column chromatography (2 cm × 37 cm, pentane/CH_2Cl_2 1:2) gave R^1-PEP$_{R1}$EP-NH$_2$ **8** (23 mg, 43%; R_f = 0.47) as a yellow film. For ^{1}H and ^{13}C NMR data, see Tables Sa1 and Sa2. Accurate MS (ESI): m/z calcd for $[M + H]^+$ $C_{58}H_{81}NO_3Si_3H^+$, 924.55970; found, 924.5583.

R^2-PEP$_{R2}$EP-NH$_2$ 9. R^1-PEP$_{R1}$EP-NH$_2$ **8** (22 mg, 0.024 mmol) was dissolved in THF (3 mL) and n−Bu_4NF (1 M in THF; 85.7 μL, 0.086 mmol) was added whereupon the reaction solution changed its color immediately from yellow to orange-brown. The solution was stirred at room temperature for 10 min. It was filtered through silica gel (2 cm × 3 cm, rinsing with THF (7 mL)). Removal of the solvent from the eluate gave a yellow solid (13.6 mg) consisting of R^2-PEP$_{R2}$EP-NH$_2$ **9** and TIPS-OH/-F. This material was used as obtained. Analytical data of R^2-PEP$_{R2}$EP-NH$_2$ **9**: for ^{1}H NMR data, see Table Sa3.

R^3-PEP$_{R3}$EP-NH$_2$ 10. To a degassed suspension of PEG-N_3 **6** (36.6 mg, 0.086 mmol) and the material that had been obtained through desilylation of R^1-PEP$_{R1}$EP-NH$_2$ **8** (13.6 mg, containing max. 0.024 mmol R^2-PEP$_{R2}$EP-NH$_2$ **9**) in anhydrous toluene (4 mL) was added $[Cu(phen)(PPh_3)_2]NO_3$•0.5 CH_2Cl_2 (1.335 mg, 1.6 μmol). The reaction mixture was stirred for 67 h at 40 °C. Metal scavenger QuadraPure TU (54 mg) was added at room temperature. The suspension was stirred for 25 h and filtered through silica gel (2 cm × 2 cm, rinsing with CH_2Cl_2/EtOH 5:1 (12 mL)). The solvent was removed from the eluate. Preparative HPLC (HPLC-column: Luna® Silica (2) Phenomenex, particle size 5 μm, pore size 100 Å, length 250 mm, internal diameter 21.2 mm; elution: room temperature, flow rate 15 mL/min, linear gradient: CH_2Cl_2/EtOH: 0-10 min 5% EtOH, 10-20 min 5%→10%, 20-30 min 10%→20%, 30-40 min 20%; detection: UV at 220 nm; the eluate between 24.5 min and 27.2 min was collected) gave R^3-PEP$_{R3}$EP-NH$_2$ **10** (28.5 mg, 69% refering to R^1-PEP$_{R1}$EP-NH$_2$ **8**) as a yellow oil. For ^{1}H and ^{13}C NMR data, see Tables Sa4 and Sa5. Accurate MS (ESI): m/z calcd for $[M + 2Na]^{2+}$ $C_{85}H_{132}N_{10}O_{27}Na_{22}^+$, 885.45239; found, 885.4514.

D-mNOPEG (R^3-PEP$_{R3}$EP-NO•perdeuterated, D-1). We applied a procedure described for structurally closely related compounds,[5,6] however using a very large excess of spin label **D-11** to cope with the challenge of handling tiny amounts of $SOCl_2$ and of the highly water sensitive intermediate **D-12**. Perdeuterated 2,2,5,5-tetramethyl-3-pyrrolin-1-oxyl-3-carboxylic acid (**D-11**) (55.6 mg, 0.282 mmol) and DMAP (78 mg, 0.638 mmol) were dissolved in anhydrous CH_2Cl_2 (2 mL) and the solution was cooled with an icebath. $SOCl_2$ (20.4 μL, 0.281 mmol) was added whereupon the solution immediately changed its color from yellow to red-orange. After stirring the reaction mixture at room temperature for 52 min, a solution of R^3-PEP$_{R3}$EP-NH$_2$ **10** (15.4 mg, 8.9 μmol) in anhydrous CH_2Cl_2 (0.8 mL) was added and the reaction mixture was stirred at room temperature for another 2.5 h. Aqueous basic workup as outlined in Fig. Sa2 gave spin label **D-11** (45.6 mg, 82%; identification via analytical HPLC through comparison with an authentic sample) as a pale yellow solid, and R^3-PEP$_{R3}$EP-NO•perdeuterated (D-mNOPEG, **D-1**) contaminated with DMAP as a yellow solid (79 mg). Preparative HPLC (HPLC-column: Luna® Silica (2) Phenomenex, particle size 5 μm, pore size 100 Å, length 250 mm, internal diameter 21.2 mm; elution: room temperature, flow rate 15 mL/min, linear gradient: CH_2Cl_2/EtOH: 0-10 min 5% EtOH, 10-20 min 5%→10%, 20-30 min 10%→20%, 30-40 min 20%; detection: UV at 220 nm; the eluate between 23.9 min and 25.3 min was collected) of the product containing material gave D-mNOPEG (**D-1**) (9.5 mg, 56%) as a yellow solid. For ^{1}H NMR data, see Table Sa4. Accurate MS (ESI): m/z calcd for $[M + 2Na]^{2+}$ $C_{94}H_{131}D_{13}N_{11}O_{29}Na_{22}^+$, 975.03659; found, 975.0353. Analytical HPLC: retention time 31.1 min (HPLC-column: Luna® Silica (2) Phenomenex, particle size 5 μm, pore size 100 Å, length 250 mm, internal diameter 4.6 mm; elution: room temperature, flow rate 1.0 mL/min, linear gradient: CH_2Cl_2/EtOH: 0-10 min 5% EtOH, 10-20 min 5%→10%, 20-30 min 10%→20%, 30-40 min 20%; detection: UV at 220 nm).

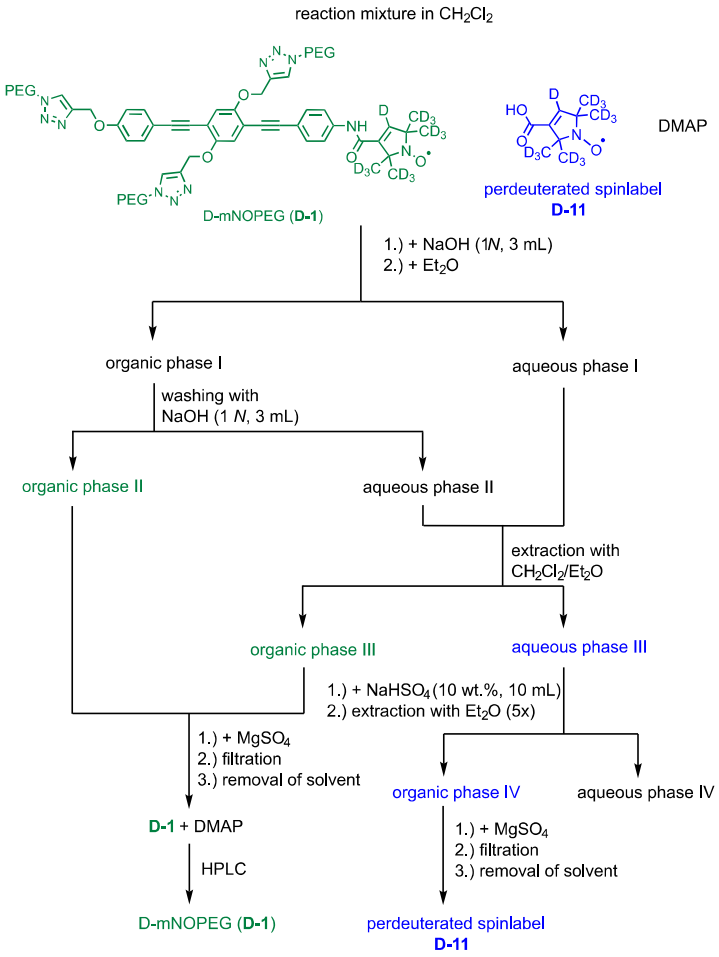

Figure Sa2 Workup of the reaction mixture obtained through spinlabeling of R^3-PEP_{R3}EP-NH2 **10** to obtain perdeuterated m-NOPEG (**D-1**).

1.4 Tabulated NMR data

For information on the effect of the paramagnetic moiety on the NMR signals of close by atoms see Supporting Information Part 2 of Ritsch *et al.* [5]

Table Sa1 ^{1}H NMR data (500 MHz) of compounds with substituent R^1 ($OCH_2C{\equiv}C$-TIPS).

compound solvent	H_{benz} of R^1-P (AA'XX')	H_{benz} of P_R (s)	$C_{benz}OCH_2$ (s)	NH_2 (broad s)	C≡CH	TIPS (s)	TMS (s)
14 $CDCl_3$	7.54 and 6.77 (2H each, *meta* and *ortho* to O)	-	4.68 (2H)	-	-	1.02 (21H)	-
15 $CDCl_3$	7.39 and 6.91 (2H each, *meta* and *ortho* to O)	-	4.71 (2H)	-	-	1.02 (21H)	0.23 (9H)
16 $CDCl_3$	7.41 and 6.94 (2H each, *meta* and *ortho* to O)	-	4.72 (2H)	-	2.99 (1H)	1.02 (21H)	-
2 CD_2Cl_2	7.46 and 7.00 (2H each, *meta* and *ortho* to O)	7.55 (*ortho* to I, 1H), 7.23 (*meta* to I, 1H)	4.81 (2H), 4.769 and 4.767 (2s with overlap, 2H each)	-	-	1.07, 1.054, and 1.046 (21H each)	-
R^1-PEP_{R1}EP-R^1 CD_2Cl_2	7.46 and 7.00 (4H each, *meta* and *ortho* to O)	7.27 (2H)	4.83 (4H), 4.77 (4H)	-	-	1.06 and 1.05 (42H each)	-
4 CD_2Cl_2	7.50 and 7.03 (broadened, 2H each, *meta* and *ortho* to O) 7.61 (very br s, 3.4H, *meta* and *ortho* to N)	7.31 (br, 2H)	4.85 (br, 4H), 4.79 (2H)	-	-	1.10 (42H), 1.08 (21H)	-
8 CD_2Cl_2	7.47 and 7.00 (2H each, *meta* and *ortho* to O) 7.32 and 6.65 (2H each, *meta* and *ortho* to N)	7.26 (4H), 7.24 (2H)	4.82 (4H), 4.77 (2H)	3.94 (2H)	-	1.07 (42H), 1.05 (21H)	-

benz = benzene

Table Sa2 ^{13}C NMR data (126 MHz) of compounds with substituent R^1 ($OCH_2C{\equiv}C$-TIPS).

compound solvent	$C_{benz}O$	$C_{benz}NH_2$	$C_{benz}H$	$\underline{C}_{benz}C{\equiv}C$	$CH_2\underline{C}{\equiv}C$	$C_{benz}\underline{C}{\equiv}\underline{C}$ $CH_2C{\equiv}\underline{C}$	$C_{benz}I$	$\underline{C}H_2C{\equiv}C$	$CH\underline{Me_2}$	$\underline{C}HMe_2$	TMS
14 $CDCl_3$	157.5	-	138.0 (*ortho* to I), 117.7	-	101.4	89.8	83.6	56.8	18.5	11.1	-
15 $CDCl_3$	157.8	-	133.3 (*ortho* to C≡C), 115.0	115.8	101.5	105.1, 92.5, 89.6	-	56.6	18.5	11.1	0.1
2 CD_2Cl_2	158.2 153.3 151.6	-	133.2 (of R^1-P, *meta* to O), 125.7 (*ortho* to I), 118.3 (*meta* to I), 115.6 (of R^1-P, *ortho* to O)	116.2, 114.7	102.0, 101.9, 101.8	94.8, 90.7, 90.4, 89.9, 84.2	86.9	58.9, 58.7, 57.0	18.73, 18.67, 18.6	11.49 11.47	-
R^1-PEP$_{R1}$EP-R^1 CD_2Cl_2	158.2 152.6	-	133.2 (of R^1-P, *meta* to O), 119.0 (of P_{R1}), 115.6 (of R^1-P, *ortho* to O)	116.3, 114.5	102.2, 102.0	95.3, 90.3, 89.9, 84.7	-	58.5, 57.1	18.7, 18.6	11.50, 11.46	-
4 CD_2Cl_2	157.1, 151.7, 151.4	not found	132.1, 131.6, 121.5 (br, C_{benz}, *ortho* to N), 118.1, 117.8, 114.5	119.1, 115.1, 113.7, 112.9	101.00, 100.97, 100.90	94.4, 93.6, 89.3, 89.2, 88.8, 84.8, 83.5	- - - -	57.7, 56.3	17.62, 17.55	10.4, 10.3	-
8 CD_2Cl_2	158.2, 152.7, 152.5	147.7	133.3 (*meta* to N), 133.2 (*meta* to O) 119.2 (of R_{R1}) 118.8 (of R_{R1}) 115.6 (*ortho* to O) 114.9 (*ortho* to N)	116.4, 115.1, 114.0, 112.5	102.3, 102.2, 102.0	96.4, 95.1, 90.2, 89.9, 84.7, 83.7	-	58.51, 58.48, 57.10	18.7, 18.6	11.51, 11.47	-

benz = benzene; *triaz* = triazole

Table Sa3 ^{1}H NMR data (500 MHz) of compounds with substituent R^2 ($OCH_2C{\equiv}C{-}H$).

compound solvent	H_{benz} of R^2-P (AA'XX')	H_{benz} of P-NH_2 or P-NO• (AA'XX')	H_{benz} of P_R (s)	$C_{benz}OCH_2$	NH_2 (s)	C≡CH
5 CD_2Cl_2	7.53 and 6.99 (slightly broadened, 2H each, *meta* and *ortho* to O)	7.59 (very br s, 3.9H, *meta* and *ortho* to N)	7.18 (2H)	4.82 (br s, 4H), 4.75 (d, J = 2.2 Hz, 2H)	-	2.64 (br s, 2H), 2.61 (t, J = 2.2 Hz, 1H)
9 CD_2Cl_2	7.51 and 6.98 (2H each, *meta* and *ortho* to O)	7.35 and 6.66 (2H each, *meta* and *ortho* to N)	7.15 (1H) 7.14 (1H)	4.80 (2 d with large overlap, J = 2.4 Hz, 2H each), 4.74 (d, J = 2.4 Hz, 2H)	3.96 (2H)	2.63 (2t with large overlap, J = 2.4 Hz, 1H each), 2.61 (t, J = 2.4 Hz, 1H)

benz = benzene

Table Sa4 ^{1}H NMR data (500 MHz) of compounds with substituent R^3 (pegylated compounds).

compound solvent	$C_{triaz}H$ (s)	H_{benz} of R^3-P (AA'XX')	H_{benz} of P-NH_2 or P-NO• (AA'XX')	H_{benz} of P_R (s)	$C_{benz}OCH_2$	$N_{triaz}CH_2$	NH_2 (s)	CH_2 of PEG	OMe	CH of PEG
H-1 CD_2CL_2	7.91 (1H), 7.89 (1H), 7.85 (br, 1H)	7.47 (2H, *meta* to O), 7.01 (2H, *ortho* to O)	7.65 (very br s, 1.3H, *ortho* to N), 7.47 (br s, overlapping with H *meta* to O, 2H, *meta* to N)	7.20 (1H), 7.18 (1H)	5.29 (2H), 5.25 (2H), 5.20 (2H)	4.52 (d overlapping with d at 4.50 ppm, J = 5.8 Hz, 2H), 4.50 (d, J = 5.2 Hz, 2H) 4.47 (br s, 2H)	-	3.60-3.35 (several m, 84H)	3.31 (s, 6H), 3.30 (br s, 12H)	2.48 (m, 2H), 2.37 (br s, 1H)
10 CD_2Cl_2	7.90 (1H), 7.88 (1H), 7.87 (1H)	7.45 (2H *meta* to O), 6.63 (2H, *ortho* to O)	7.25 (2H, *meta* to N) 6.99 (2H, *ortho* to N)	7.15 (1H) 7.13 (1H)	5.26 (2H), 5.24 (2H), 5.19 (2H)	4.51, 4.50 and 4.48 (3d with overlapping, J = 6.3 Hz, 2H each)	4.10 (2H)	3.61-3.34 (several m, 84H)	3.302 3.295 and 3.29 (3s, 6H each)	2.46 (m, 3H)
D-1 CD_2Cl_2	7.91 (1H), 7.89 (1H), 7.85 (br, 1H)	7.46 (2H *meta* to O), 7.01 (2H, *ortho* to O)	7.66 (very br s, 1.3 H, *ortho* to N), 7.46 (br s, overlapping with H *meta* to O, 2H, *meta* to N)	7.20 (1H) 7.18 (1H)	5.28 (2H), 5.24 (2H), 5.20 (2H)	4.52 (d overlapping with d at 4.50 ppm, J = 5.8 Hz, 2H), 4.50 (d, J = 5.2 Hz, 2H), 4.46 (br s, 2H)	-	3.60-3.34 (several m, 84H)	3.31 (s, 6H), 3.29 (br s, 12H)	2.48 (m, 2H), 2.37 (br s, 1H)

benz = benzene; triaz = triazole

Table Sa5 ^{13}C NMR data (126 MHz) of compounds with substituent R^3 (pegylated compounds).

compound solvent	$C_{benz}O$	$C_{benz}NH_2$	C_{triaz}	HC_{triaz}	$C_{benz}H$	$\underline{C}_{benz}C\equiv C$	$C_{benz}\underline{C}\equiv\underline{C}$	$\underline{C}H_2$ of PEG	$C_{triaz}\underline{C}H_2$	OCH_3	$N_{triaz}\underline{C}H_2$	$\underline{C}HCH_2O$
H-1 CD_2Cl_2	158.8, 153.6, 153.2	not found	143.7, 143.2, 143.0	125.1, 124.5	133.2, 131.9, 120.5 (br, C_{benz}) *ortho* to N), 118.4, 118.2, 115.03	119.0 (br), 115.6, 115.04, 114.4	95.3, 94.8, 85.5, 84.5	72.00, 71.98, 70.71, 70.67, 70.64, 70.60, 70.53, 70.47, 70.45, 70.38, 70.33, 69.04, 68.97	64.3, 63.9, 62.1	58.8, 58.7	48.71, 48.68, 48.60´	40.75, 40.70, 40.69
10 CD_2Cl_2	159.0, 153.5, 153.4	148.0	143.8, 143.5, 143.2	125.34, 125.30, 125.10	133.4 (of R^3-P, *meta* to O), 133.2 (of P-NH_2, *meta* to N), 118.6 (of P_{R3}), 118.4 (of P_{R3}), 115.3 (of P-NH_2, *ortho* to N), 114.8 (of R^3-P, *ortho* to O)	116.0, 115.5, 114.4, 112.0	96.7, 95.2, 84.9, 83.8	72.20, 70.94, 70.90, 70.87, 70.83, 70.82, 70.70, 70.68, 70.62, 70.59, 70.57, 69.30, 69.20	64.2, 64.1, 62.3	58.93, 58.91	48.91, 48.90, 48.80	40.97, 40.96, 40.95

benz = benzene; *triaz* = triazole

2 Characterization of H-mNOPEG aggregates by 4-pulse DEER

Concentration-dependent 4-pulse DEER measurements characterize the aggregate formation of H-mNOPEG as shown in Fig. 2**(b)**, main text. Fig. Sa3 displays the dipolar signal of the 80 μM sample along with the data analysis performed with the open-source MATLAB toolbox DeerLab[7] (DL, version 0.9.2.), using the single-pathway 4-pulse DEER experiment model (ex_4pdeer) combined with a stretched exponential background model (bg_strexp, $B(t) = \exp(-\lambda\kappa|t|^d)$). The parameter-free distance distributions $P(r)$ was computed via Tikhonov regularization, while generalized cross-validation (GCV) selected the optimal regularization parameter. All fitting parameters (the modulation depth λ, the decay rate κ and the stretch factor d) were validated with bootstrapping in the following parameter ranges: $\lambda = 0.2-0.3, \kappa = 0.005-0.5\ \mu s^{-d}$, $d = 0.9-1.2$. 500 bootstrapping samples correspond to converged 95% confidence intervals, and the resulting upper and lower bounds in the time- and distance-domain are displayed in Fig. Sa3 **(a)** and **(b)**, respectively. The obtained distance distribution features peaks at multiple distances with the largest contribution at 3.6 nm. We cannot state with certainty how many H-mNOPEG molecules form these aggregates or whether different aggregate sizes or arrangements contribute to the dipolar signal and multi-spin effects introduce uncertainty in the distance distribution.[8]

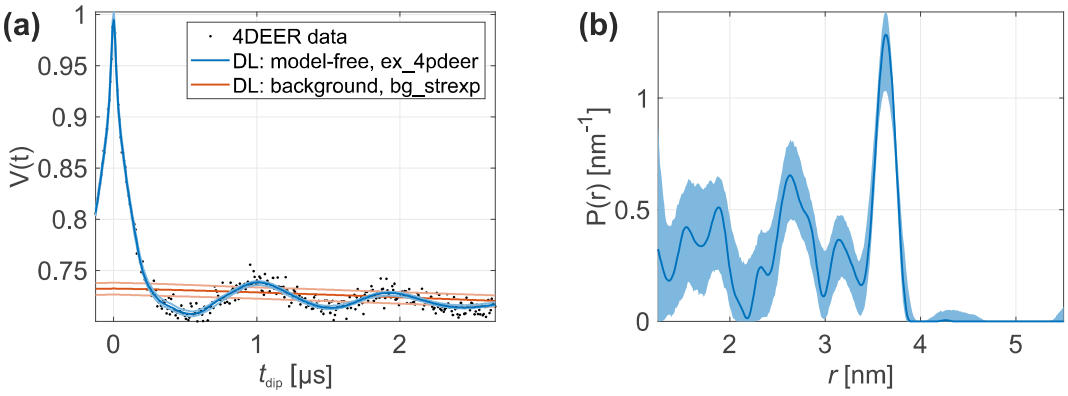

Figure Sa3 (a) 4-pulse DEER measurement $V(t)$ of 80 μM H-mNOPEG in H_2O:glycerol at 60 K (black dots). Time-domain parameter-free fit (dark blue) along with the stretched exponential background model (dark orange) with $\lambda = 0.268, \kappa = 0.0195\ \mu s^{-d}, d = 1.2$. The lighter colors indicate the 95% confidence interval associated with the following 95% confidence intervals: $\lambda = 0.262-0.274, \kappa = 0.015-0.029\ \mu s^{-d}$, $d = 0.9-1.2$. **(b)** Parameter-free distance distribution $P(r)$ (dark blue) with 95% confidence interval (shaded blue area).

3 Fitting procedure for Hahn echo and DD relaxation traces

Experimental Hahn echo and DD relaxation traces were fitted using an SE and SSE model, as defined in the main text. A home-written Matlab script was used based on the non-linear least square solver `lsqcurvefit`. Properties of the decay curves, *i.e.* the initial intensity and the last recorded time point, defined generous upper limits as well as bounds for initial values of the fitting parameters c_i and T_{m_i}. N fit results were obtained from launching the least square minimization with N initial parameter value combinations from uniformly distributed pseudo-random numbers within these bounds. The initial parameter range for T_{m_1} was set to a tenth of the respective T_{m_2} bounds. This procedure was implemented to avoid local minima of the objective function, and consequently the fit associated with the smallest root-mean-square deviation (RMSD) was chosen from the N results. In order to provide information on the uncertainty of the selected parameter values, the 95% confidence interval were computed from the Jacobian using the Matlab function `nlparci` for the dephasing time(s) and stretch parameter value(s). Note, that the fitting parameters of the SSE model include the two absolute amplitudes c_1 and c_2, from which the normalized amplitude of the fast relaxation process is computed with $A_1 = c_1/(c_1+c_2)$ to facilitate a more intuitive understanding. The uncertainty associated with the A_1 parameter results from error propagation according to Eq. (1)

$$\sigma_{A_1} = \sqrt{\sum_{i=1}^{2}\left(\frac{\partial A_1}{\partial c_i}\right)^2 \cdot \sigma_{c_i}^2} = \sqrt{\left[\frac{c_2}{(c_1+c_2)^2}\right]^2 \cdot \sigma_{c_1}^2 + \left[\frac{-c_1}{(c_1+c_2)^2}\right]^2 \cdot \sigma_{c_2}^2}, \tag{1}$$

where σ corresponds to the standard error, from which the 95 % confidence interval of A_1 can be obtained. Note that upper or lower confidence bounds that extend beyond the physically possible values of 1 and 0 were limited to these values.

In cases where electron spin echo envelope modulation (ESEEM) was present in the relaxation traces, only the modulation maxima were fed into the fitting procedure.[9] The Matlab function `findpeaks` helped to identify these

data points. Uniform sampling was ensured by using the same sampling frequency in the time window beyond the pronounced nuclear modulations.

3.1 Comparison: SE and SSE parameterization

The following sections 4, 5 and 6 show relaxation data along with SE and SSE fits for nitroxides, trityl radicals and gadolinium complexes, respectively. In each case, the appropriate parameterization was chosen based on a comparison between the fit quality of the SE and SSE parameterization. Specifically, Fig. Sa5 to Sa8 display fits to temperature-dependent Hahn echo relaxation of H-NO and D-NO in H_2O:glycerol and D_2O:glycerol-d_8, and Fig. Sa12 to Sa15 compares the fits to DD data sets of H-mNOPEG and D-mNOPEG in the same solvents at 40 K. The comparison for DD data of OX063 and OX071 at 110 K is presented in Fig. Sa22 to Sa25. Finally, Fig. Sa29 to Sa32 contrasts the two relaxation models for DD data of Gd-NO_3Pic, Gd-DOTA-M and Gd-PCTA in H_2O:glycerol and Gd-DOTA-M in D_2O:glycerol-d_8 at 10 K, recorded at the maximum of the gadolinium line (B_{max}). For Gd-NO_3Pic, Gd-DOTA-M and Gd-PCTA in H_2O:glycerol the same comparison was also performed for DD data acquired at the kink of the corresponding gadolinium Q-band spectrum (B_{kink}), shown in Fig. Sa36 to Sa38. In all these figures, the experimental data is shown in blue, the fit in red and the associated residual in black. The dashed black line extends the fitted model into the non-accessible dead time. Each subfigure title specifies the employed fit model, while the addition "(max)" indicates pronounced nuclear modulation so that only the maxima served as input to the fit procedure as described in Section 3. The titles also specify the variable experimental condition, *i.e.* the specific temperature for the series of Hahn echo measurements, or the employed pulse sequence for a DD data set at a fixed temperature. In the latter case, CP*n* stands for Carr-Purcell and U*n* abbreviates Uhrig, while n indicates the number of used π pulses. In addition, the underlying parameter values for the displayed fits are listed, rounded to two decimal points. The two contributions of the SSE model are sorted by T_{m_i} values, where index $i = 1$ marks the fast relaxation process identified by $T_{\mathrm{m}_1} < T_{\mathrm{m}_2}$, and corresponds to the first elements in the reported c, A, T_{m} and ξ vectors. Two green lines illustrate the two contributions to the overall SSE fit in red.

4 Nitroxides

Based on the temperature-dependent Hahn relaxation of H-NO and D-NO in water-glycerol glass two distinct temperature regimes are defined in the main text in section 3.2.1 in analogy to previous results in *o*-terphenyl.[10] Section 4.1 shows the underlying experiment data along with SE/SSE fits and the resulting temperature-dependent stretched exponential(s) parameter values. In the low-temperature regime (10-60 K) two separable relaxation pathways contribute to the transverse relaxation as is evident from the prevailing SSE model and the selective effects from pulse length variations shown in section 4.2. The SSE model was consequently applied to characterize the relaxation behavior of all four sample compositions featuring H- or D-mNOPEG in H_2O:glycerol or D_2O:glycerol-d_8 at 40 K as shown in detail in section 4.3. Additional DD experiments at 60 K were carried for H-mNOPEG in both H_2O:glycerol and D_2O:glycerol-d_8 to illustrate the difference in temperature-dependence between protonated and deuterated solvents arising somewhat above 40 K as also observed in case of *o*-terphenyl.[10] Section 4.4 presents the resulting DD data. Finally, the relaxation behavior of the small nitroxide H-NO is compared to the larger nitroxide H-mNOPEG at 40 and 60 K in section 4.5 to evaluate to what extent local motions in the glass voids influence the decoupling effect.

4.1 Temperature-dependent Hahn relaxation (10-140 K)

The individual Hahn relaxation traces along with fits based on the SE and SSE model are shown for H-NO in H_2O:glycerol in Fig. Sa5, for H-NO in D_2O:glycerol-d_8 in Fig. Sa6, for D-NO in H_2O:glycerol in Fig. Sa7 and for D-NO in D_2O:glycerol-d_8 in Fig. Sa8 for temperatures between 10 and 140 K. A yellow highlight of a subplot's title indicates that the SSE model is clearly superior in fitting the experimental Hahn data, as the SE model underfits the data visible from the strongly oscillating fit residuals. Instead, a blue highlight covering the two adjacent SE and SSE subplots for a given temperature marks that both models lead to comparable fit qualities. In this case the simpler SE model is chosen motivated by the parsimony principle. Fig. Sa4 compares the SE/SSE parameterization of the temperature-dependent Hahn relaxation for a given nitroxide (H-NO or D-mNO) or matrix type (H_2O:glycerol or D_2O:glycerol-d_8.)

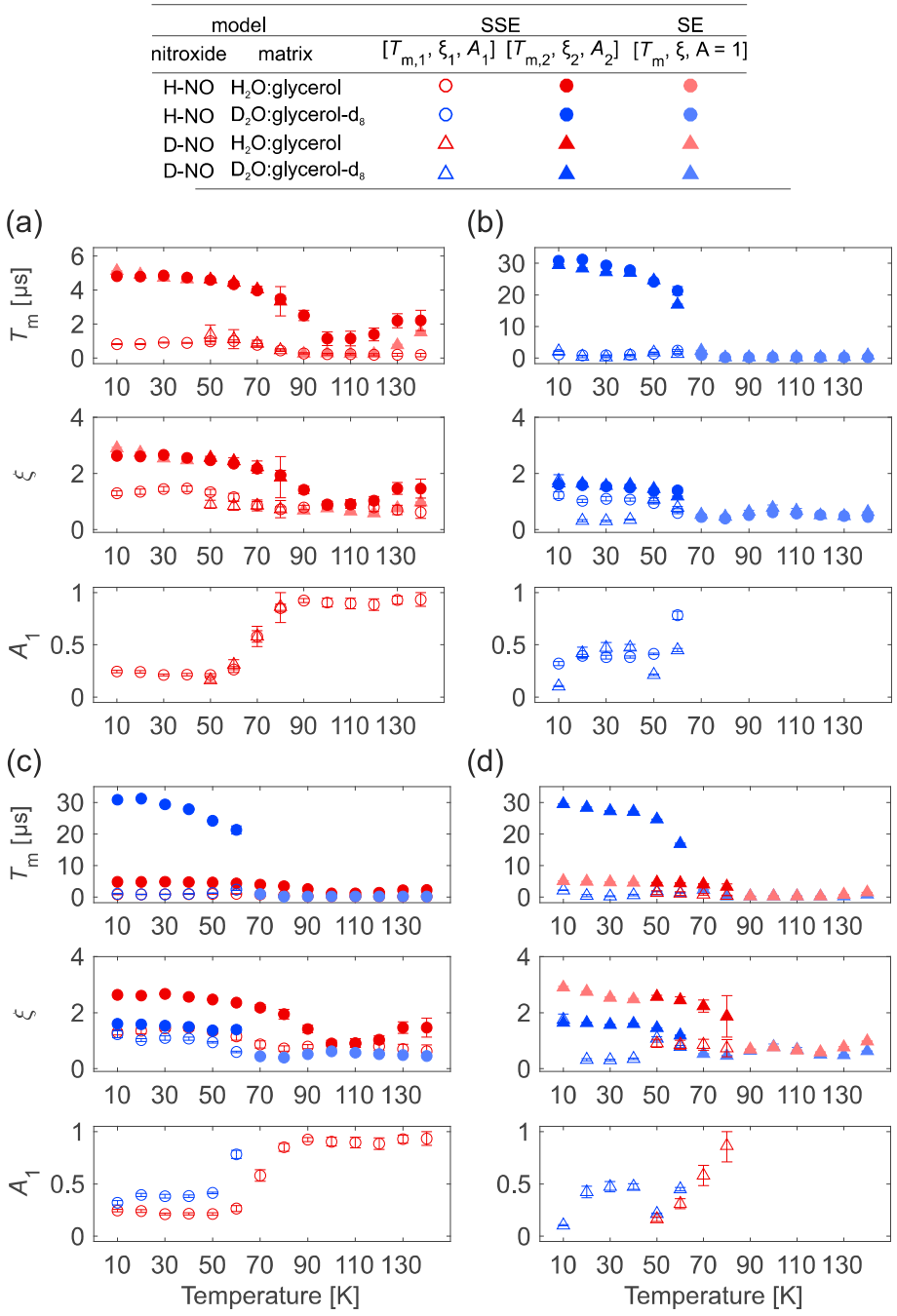

Figure Sa4 SSE and SE parameterization of temperature-dependent Hahn echo relaxation recorded at a spin concentration of 100 μM using pulse lengths of $t_\pi = 2 \cdot t_{\pi/2} = 12$ ns. The table at the top defines how the markers encode the nitroxide and matrix type, along with the appropriate relaxation model. Each subplot **(a)** to **(d)** compares the (S)SE parameters T_m (top), ξ (middle) and A_1 (bottom, only shown for the SSE model) as a function of temperature for a given matrix or nitroxide. The error bars mark the 95% confidence intervals. **(a)** H-NO compared to D-NO in H_2O:glycerol, **(b)** H-NO compared to D-NO in D_2O:glycerol-d_8, **(c)** H-NO in H_2O:glycerol compared to D_2O:glycerol-d_8 and **(d)** D-NO in H_2O:glycerol compared to D_2O:glycerol-d_8.

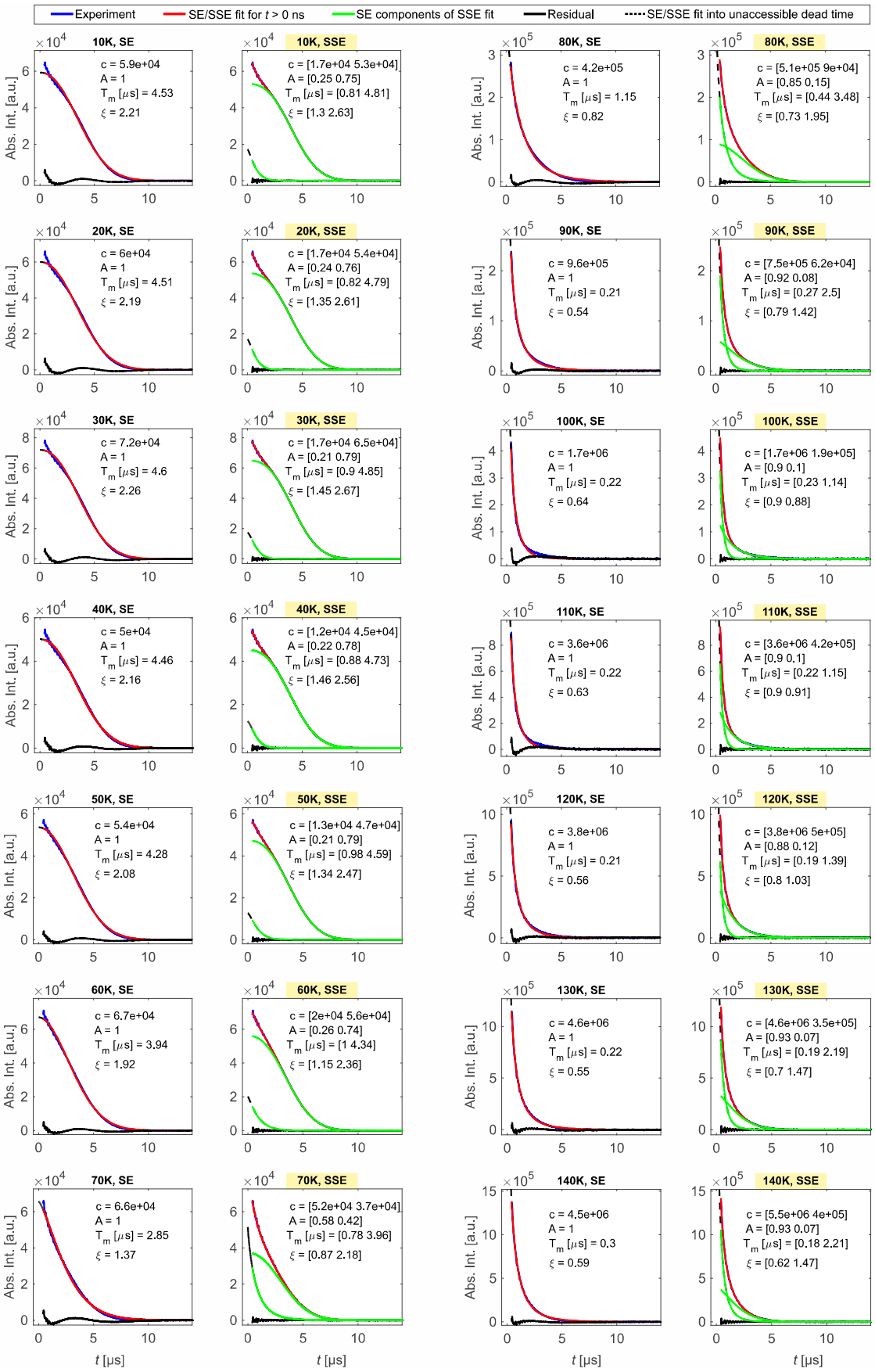

Figure Sa5 Comparison of an SE and SSE fit to the temperature-dependent Hahn relaxation of 100 μM H-NO in H_2O:glycerol recorded at B_{max} with $t_\pi = 2 \cdot t_{\pi/2} = 12$ ns.

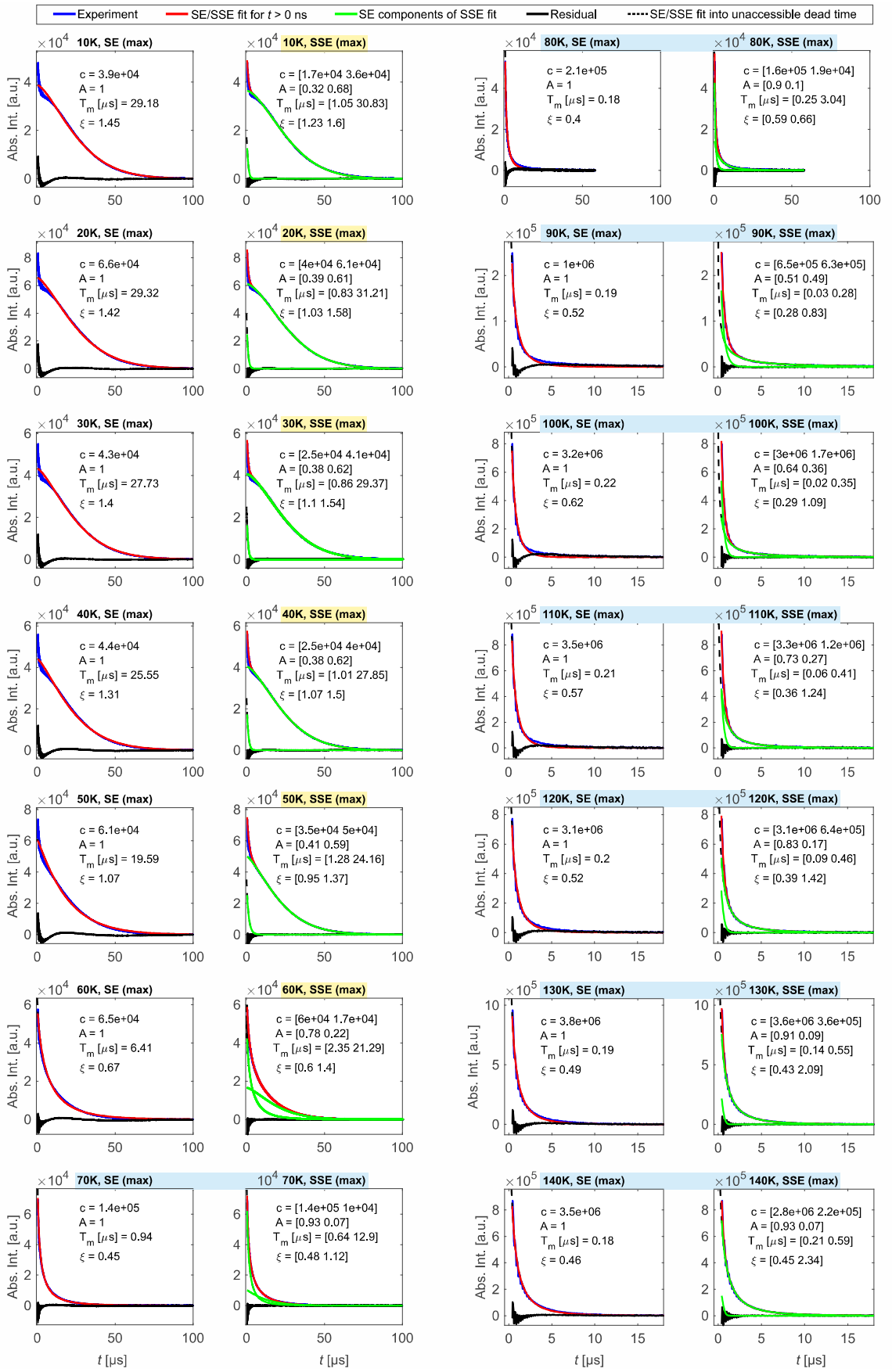

Figure Sa6 Comparison of an SE and SSE fit to the temperature-dependent Hahn relaxation of 100 μM H-NO in D_2O:glycerol-d_8 recorded at B_{max} with $t_\pi = 2 \cdot t_{\pi/2} = 12$ ns.

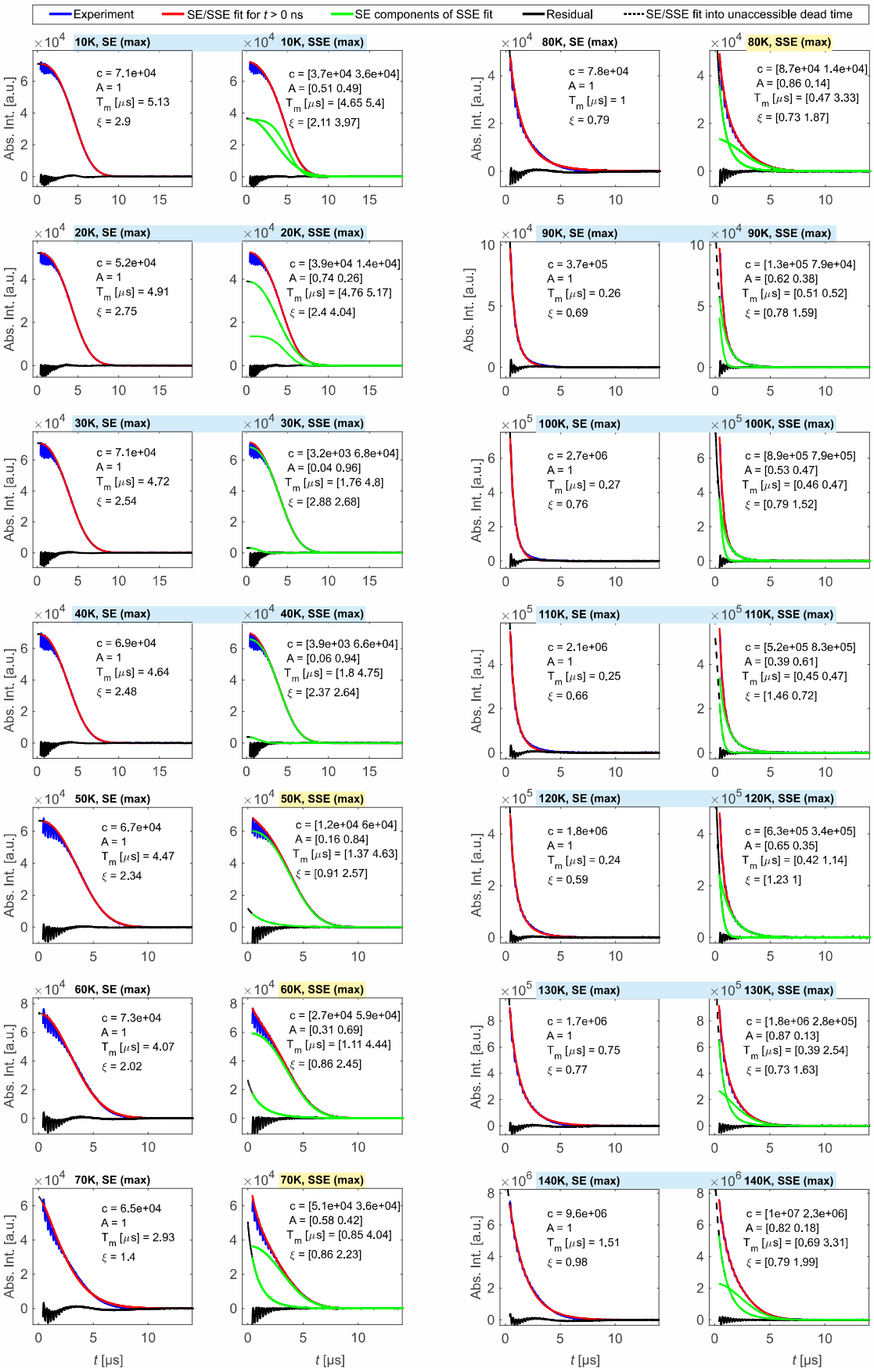

Figure Sa7 Comparison of an SE and SSE fit to the temperature-dependent Hahn relaxation of 100 μM D-NO in H_2O:glycerol recorded at B_{max} with $t_\pi = 2 \cdot t_{\pi/2} = 12$ ns.

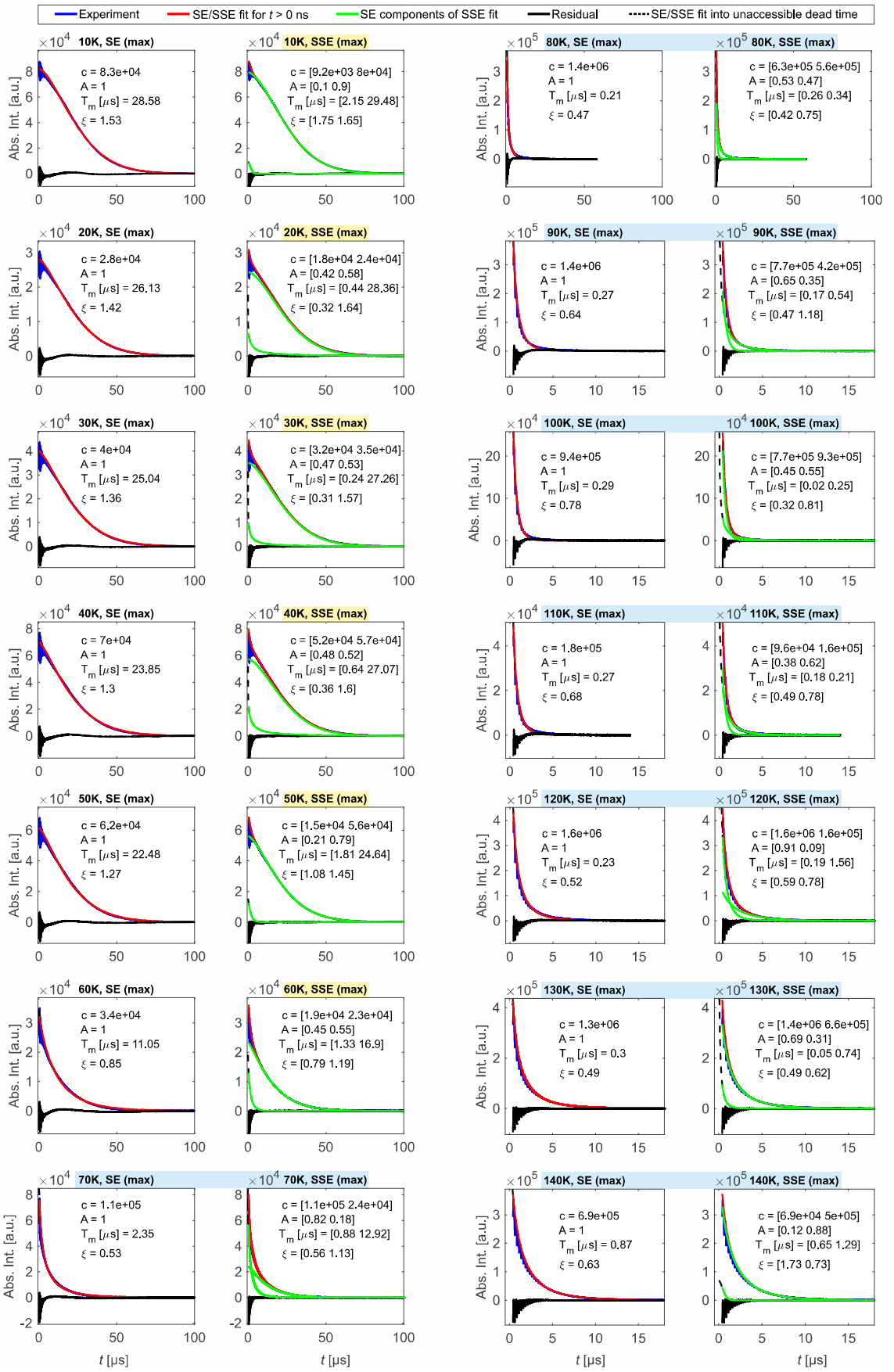

Figure Sa8 Comparison of an SE and SSE fit to the temperature-dependent Hahn relaxation of 100 μM D-NO in D_2O:glycerol-d_8 recorded at B_{max} with $t_\pi = 2 \cdot t_{\pi/2} = 12$ ns.

4.2 Pulse length variation at 40 K

In both water-glycerol and *o*-terphenyl glass, SSE fits to low-temperature Hahn relaxation reveal two separate relaxation contributions that can be assigned based on nitroxide and/or solvent deuteration. Additionally, pulse length variation can experimentally distinguish between the fast and slow relaxation pathway as already demonstrated for *o*-terphenyl.[10] Fig. Sa9 shows the effect of a reduced excitation bandwidth with $t_\pi = 2 \cdot t_{\pi/2} = 96$ ns relative to strong pulses with $t_\pi = 2 \cdot t_{\pi/2} = 12$ ns. While nuclear spin diffusion (NSD) dominates the fast and/or slow relaxation component in case of protonated nitroxide and/or solvent, the pulse length variation probes the contribution from instantaneous diffusion (ID). The latter mechanisms dominates at sufficient high spin concentration, *e.g.* if NSD is suppressed by deuteration. Consequently, pulse length variation affects the entire Hahn relaxation in case of D-NO in D_2O:glycerol-d_8, while no difference between strong and soft pulses are observed for H-NO in H_2O:glycerol. For H-NO in D_2O:glycerol-d_8 only the solvent-driven slow relaxation pathway is slowed by a reduced excitation pathway. The limited pulse length effect on the fast relaxation process in D-NO in H_2O:glycerol (also compared to D-mNOHex in dOTP[10]) is in line with the comparable fit quality for the SE and SSE model as shown in Fig. Sa7. As discussed in the main text, the Hahn experiment is not able to fully resolve the two underlying processes, while experiments with multiple refocusing pulses can do so, as demonstrated in Fig. Sa14 and Sa11 for D-mNOPEG in H_2O:glycerol at 40 K.

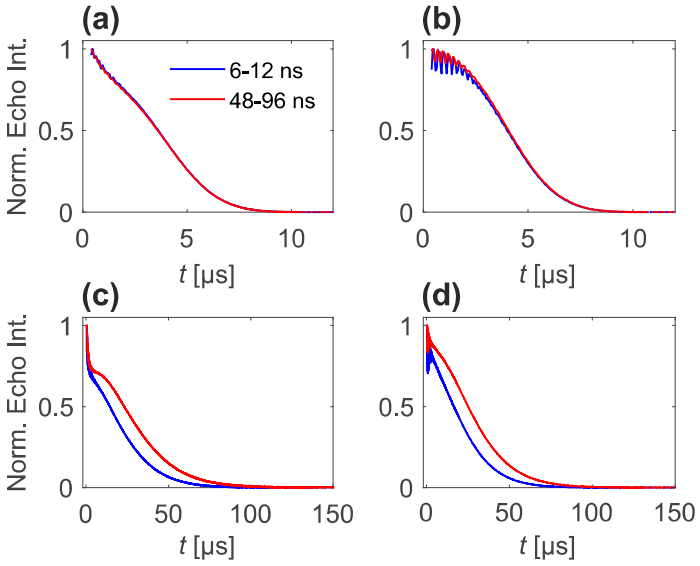

Figure Sa9 Pulse-length dependent Hahn relaxation recorded at a spin concentration of 100 μM and a temperature of 40 K at B_{max}. **(a)** H-NO in H_2O:glycerol, **(b)** D-NO in H_2O:glycerol, **(c)** H-NO in D_2O:glycerol-d_8 and **(d)** D-NO in D_2O:glycerol-d_8.

4.3 Dynamical decoupling at 40 K

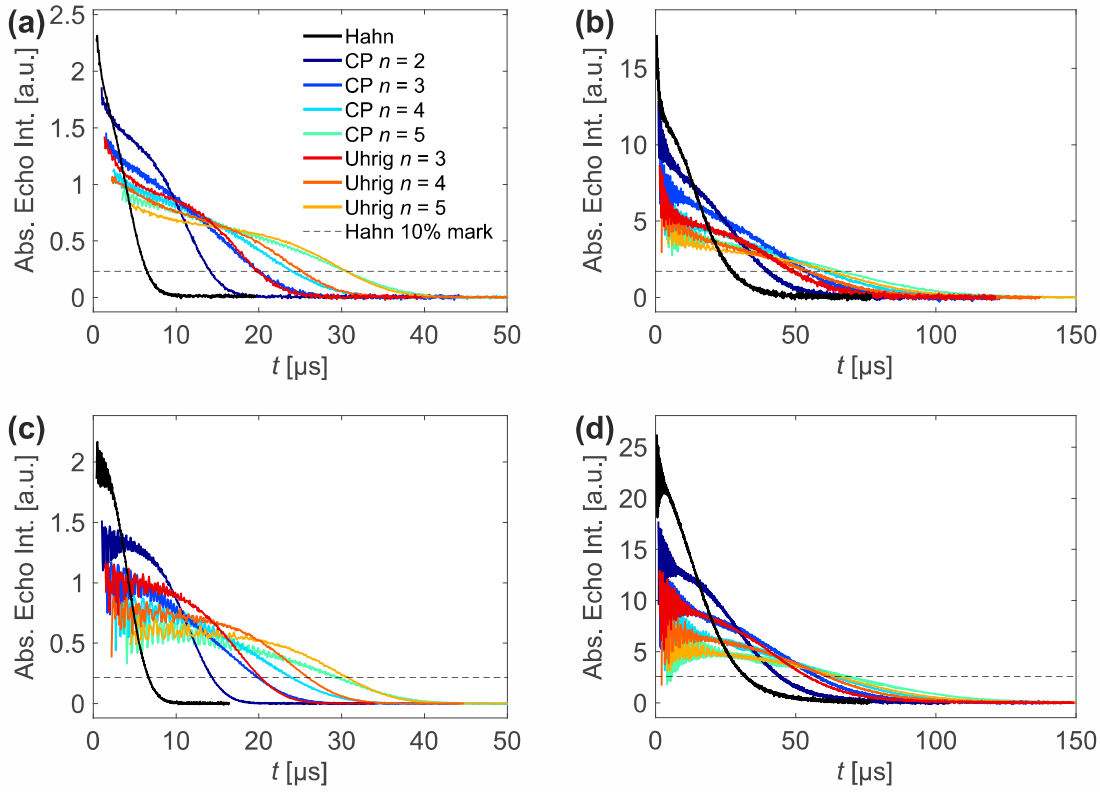

Figure Sa10 DD data sets of H- and D-mNOPEG recorded at a spin concentration of 10 μM and a temperature of 40 K at $B_{\max}$ using pulse lengths of $t_\pi = t_{\pi/2} = 12$ ns. **(a)** H-mNOPEG in H_2O:glycerol along with a legend that defines the color code for the DD experiments. **(b)** H-mNOPEG in D_2O:glycerol-d_8, **(c)** D-mNOPEG in H_2O:glycerol and **(d)** D-mNOPEG in D_2O:glycerol-d_8.

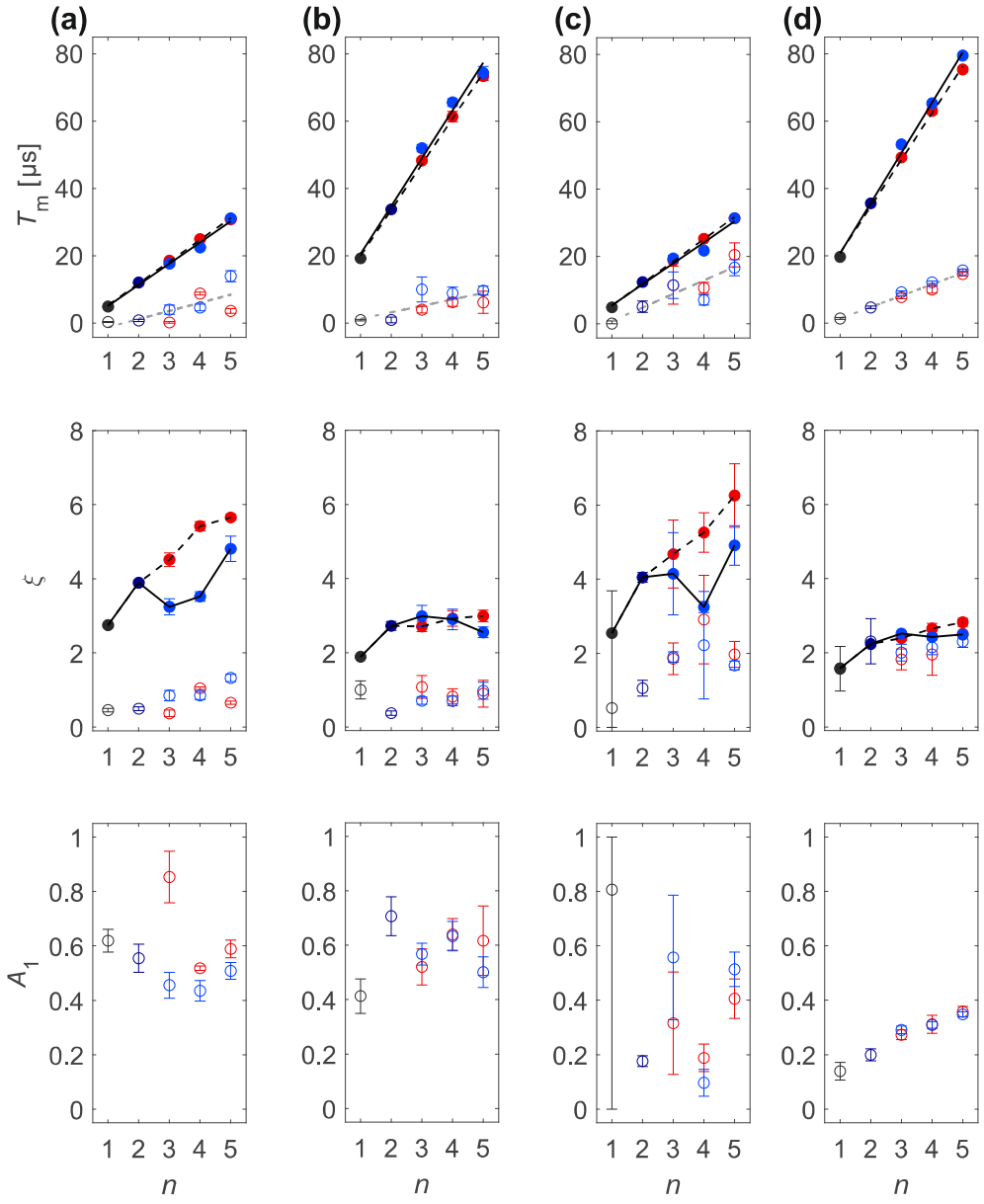

Figure Sa11 SSE parameterization of DD data recorded at B_{max} and 40 K for H- and D-mNOPEG (10 μM) in water-glycerol glass: (a) H-mNOPEG in H_2O:glycerol, (b) H-mNOPEG in D_2O:glycerol-d_8, (c) D-mNOPEG in H_2O:glycerol, (d) D-mNOPEG in D_2O:glycerol-d_8. Each column displays the fitting parameters T_{m_i}, ξ_i, A_1 (top to bottom) with the associated 95% confidence intervals for a particular sample as a function of n. The color encodes the DD experiment with Hahn (●), CP/Uhrig $n = 2$ (●), CP $n > 2$ (●) and Uhrig $n > 2$ (●), while empty circles correspond to the fast ($i = 1$), and filled to the slow ($i = 2$) relaxation contribution. Lines in the T_{m_i} subplots report linear regression results for experiment-specific T_{m_2} increase with n for CP (black, solid) and Uhrig (black, dashed), whereas a common T_{m_1} gain with n (grey, dashed) was determined. All resulting slopes are summarized in Table 1 in the main text. Black lines shown in the ξ_i subplot serve as a guide for the eye to indicate ξ_2 dependence on n for CP (solid) and Uhrig (dashed) experiments.

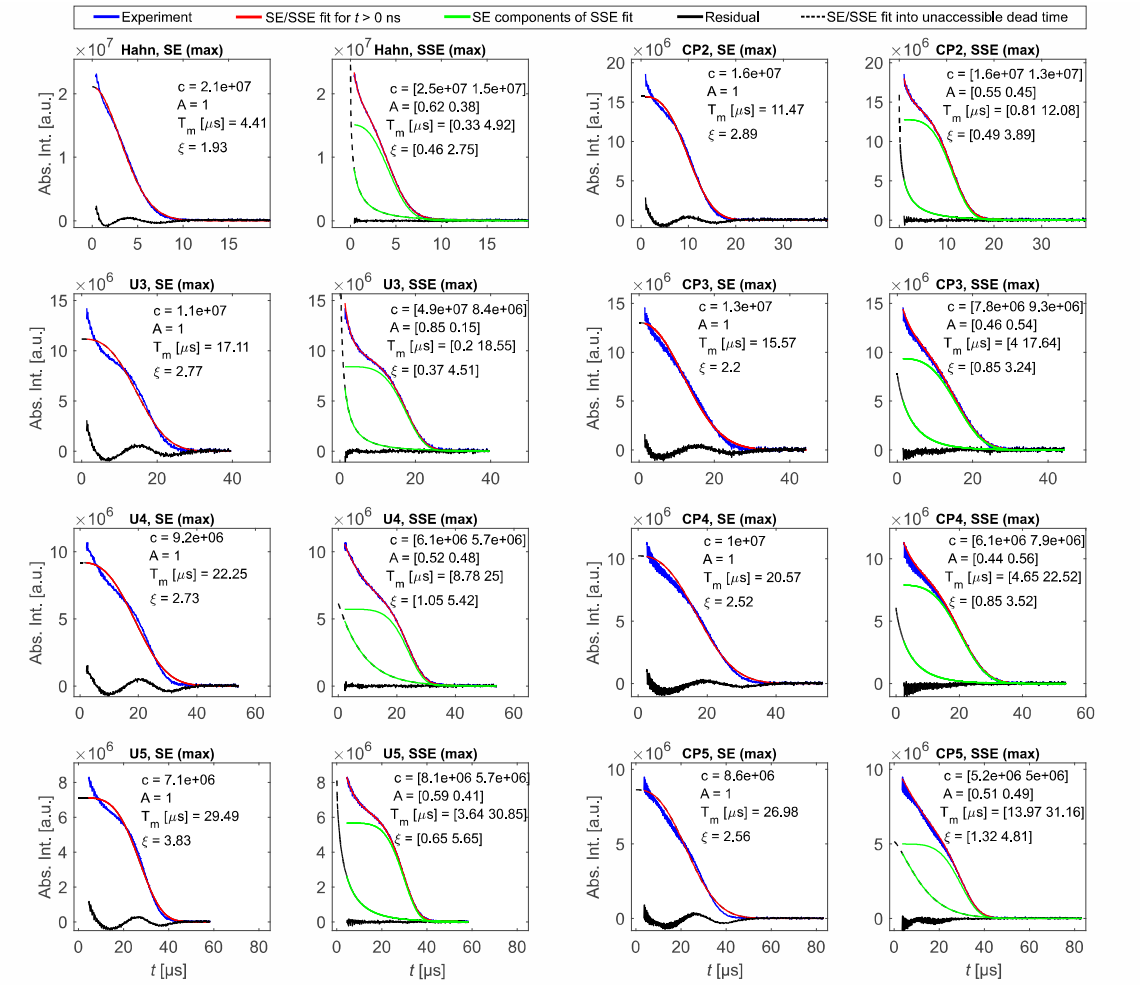

Figure Sa12 Comparison of an SE and SSE fit to the DD data of 10 μM H-mNOPEG in H_2O:glycerol recorded at 40 K and B_{max} with $t_\pi = t_{\pi/2} = 12$ ns.

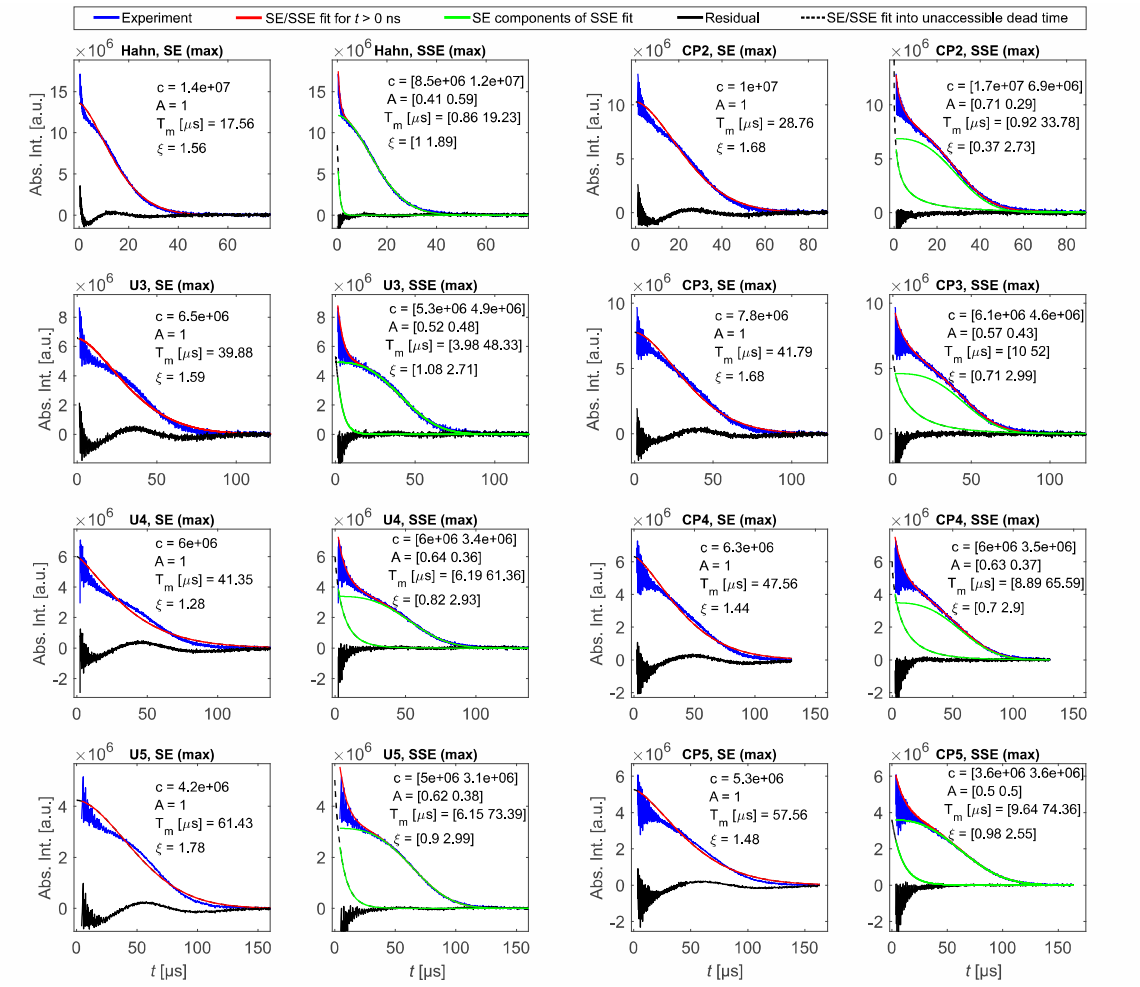

Figure Sa13 Comparison of an SE and SSE fit to the DD data of 10 μM H-mNOPEG in D_2O:glycerol-d_8 recorded at 40 K and B_{max} with $t_\pi = t_{\pi/2} = 12$ ns.

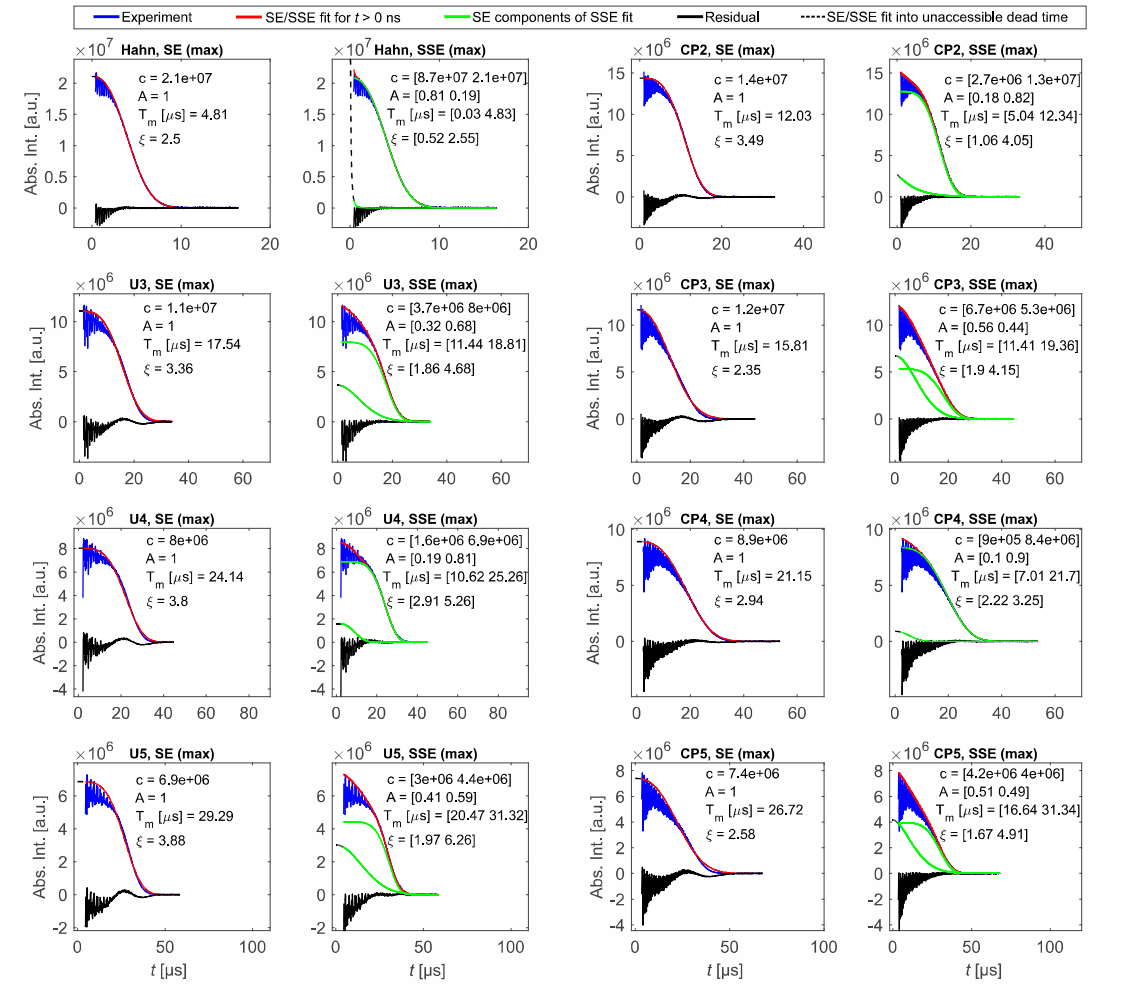

Figure Sa14 Comparison of an SE and SSE fit to the DD data of 10 μM D-mNOPEG in H_2O:glycerol recorded at 40 K and B_{max} with $t_\pi = t_{\pi/2} = 12$ ns.

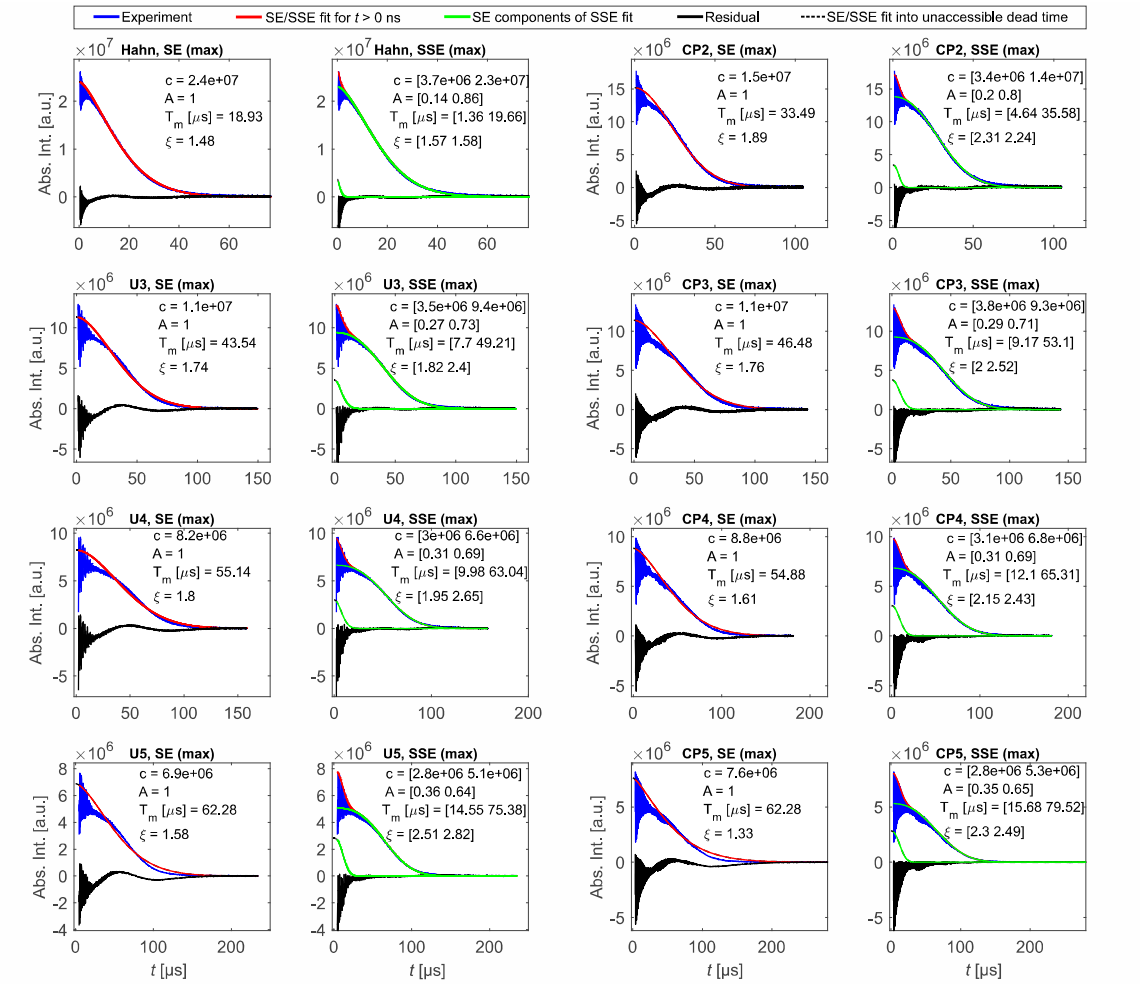

Figure Sa15 Comparison of an SE and SSE fit to the DD data of 10 μM D-mNOPEG in D_2O:glycerol-d_8 recorded at 40 K and B_{max} with $t_\pi = t_{\pi/2} =$ 12 ns.

4.4 Dynamical decoupling at 60 K

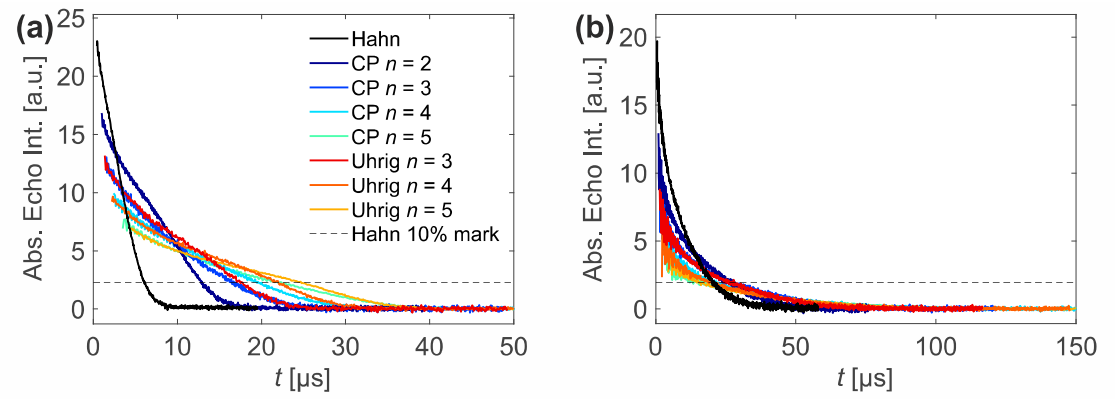

Figure Sa16 DD data sets of H-mNOPEG recorded at a spin concentration of 10 μM and a temperature of 60 K at $B_{\max}$ using pulse lengths of $t_\pi = t_{\pi/2} = 12$ ns. **(a)** H-mNOPEG in H_2O:glycerol along with a legend that defines the color code for the DD experiments, **(b)** H-mNOPEG in D_2O:glycerol-d_8.

4.5 Dynamical decoupling comparison at 40 and 60 K

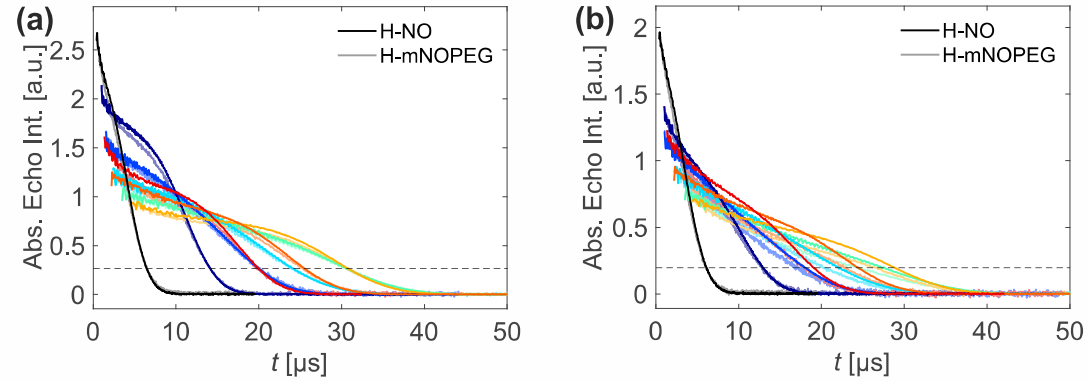

Figure Sa17 DD data set comparison between H-NO (dark colors) and H-mNOPEG (light colors) in H_2O:glycerol. Recorded at a spin concentration of 10 μM at $B_{\max}$ using pulse lengths of $t_\pi = t_{\pi/2} = 12$ ns at temperatures **(a)** 40 K and **(b)** 60 K. For a legend that defines the color code for the DD experiments, see *e.g.* Fig. Sa10**(a)**.

5 Trityl radicals: OX063 and OX071

The Hahn decays of OX063 and OX071 in D_2O:glycerol-d_8 were used to optimize the experimental conditions for DD experiments. In section 5.1 the temperature is screened, while section 5.2 identifies the concentration that sufficiently suppresses ID and addresses the effect of dissolved oxygen on the transverse relaxation of glassy trityl samples. Section 5.3 provides all experimental DD data, SE/SSE fits and scaling of the resulting stretched exponential(s) parameter values with n for the four sample compositions of OX063 and OX071 in H_2O:glycerol and D_2O:glycerol-d_8.

5.1 Temperature-dependent Hahn relaxation (50-120 K)

The temperature range of 50 to 120 K was screened to identify a convenient shot repetition time (SRT) for the DD experiments at some expense of the dephasing time as shown for OX063 in D_2O:glycerol-d_8 in Fig. Sa18**(a)**. Solvent deuteration clearly narrows the echo-detected linewidth of OX063 as presented in Fig. Sa18 by scaling the unresolved hyperfine (HF) couplings to the solvent nuclei.

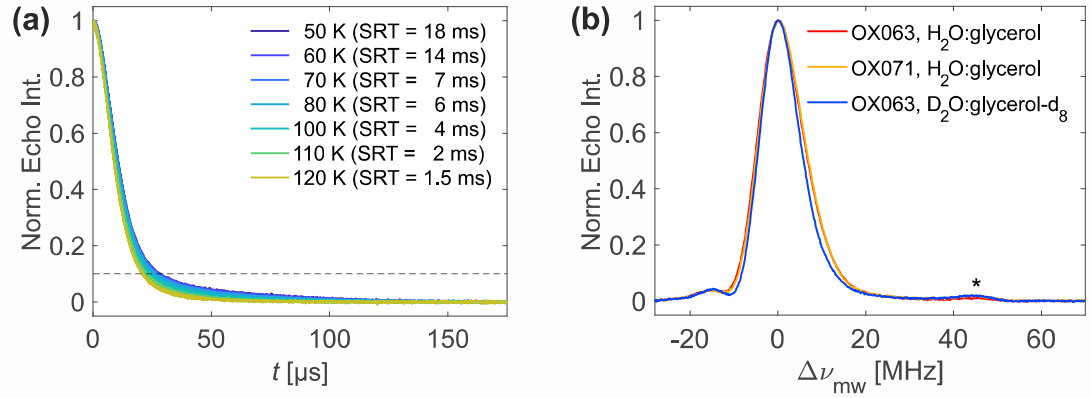

Figure Sa18 (a) Temperature-dependent Hahn echo relaxation of OX063 in D_2O:glycerol-d_8 recorded at a spin concentration of 10 μM at B_{max} using pulse lengths of $t_\pi = t_{\pi/2} = 12$ ns. The dashed line marks the 10% reference level to determine $T_{10\%}^{Hahn}$, and the appropriate SRT for each temperature is reported in the legend. **(b)** Hahn-echo detected fieldsweep (shown on a relative frequency axis with respect to B_{max}) recorded at spin concentration of 10 μM and a temperature of at 110 K. The asterisk marks a small peak that originates from E' centers in the quartz capillaries.

5.2 Concentration and oxygen effect

The trityl sample with the strongest NSD suppression was chosen, *i.e.* OX071 in D_2O:glycerol-d_8, to detect the largest possible effect of ID and oxygen on the low-temperature transverse relaxation of trityl radicals. The pulse-length dependent Hahn relaxation in Fig. Sa19**(a)** demonstrates that ID is a relevant dephasing mechanism at 20 μM and even at 10 μM a residual effect is visible. Dissolved oxygen induces an additional relaxation pathway if the atmosphere is saturated by oxygen gas prior to flash-freezing the sample as evident from Fig. Sa19**(b)**. However, degassing the sample by ten freeze-pump-thaw cycles, nominally achieving 0 volume % oxygen, does not affect the Hahn relaxation significantly as shown in Fig. Sa19**(c)**. Therefore, a certain oxygen concentration in the atmosphere beyond 20 volume % is required to activate this mechanism in the frozen state to an extent exceeding experimental uncertainty.

5.3 Dynamical decoupling at 110 K

DD data sets of OX063 and OX071 in both H_2O:glycerol and D_2O:glycerol-d_8 were acquired at B_{max} under optimized experimental conditions, namely at 110 K, 10 μM spin concentration and flash-freezing the sample under normal atmospheric conditions. Fig. Sa20 presents the experimental results. As described in the main text, the required fitting expression switches for the Hahn and DD experiments with $n > 1$. In the protonated solvent, the SSE model is required for $n > 1$ as visible in Fig. Sa22 for OX063 and in Fig. Sa24 for OX071. Yet, SSE fits to the Hahn decay result for both trityl radicals in highly uncertain A_1 (and ξ_1) parameter values along with a T_{m_1} of close to 0 μs as shown in Fig. Sa21**(a)** and **(c)** so that the SE model suffices. According to Fig. Sa23 and Sa25 the deuterated solvent leads to the opposite observation as only the SSE expression can model the Hahn relaxation of OX063 and OX071, while the SE model fits the remaining DD data well.

The dependence of the stretched exponential(s) parameters on n is discussed without taking the described model switching into account. Therefore, Fig. Sa21 relies on the SSE parameterization in case of H_2O:glycerol, while for D_2O:glycerol-d_8 the SE model is exclusively used.

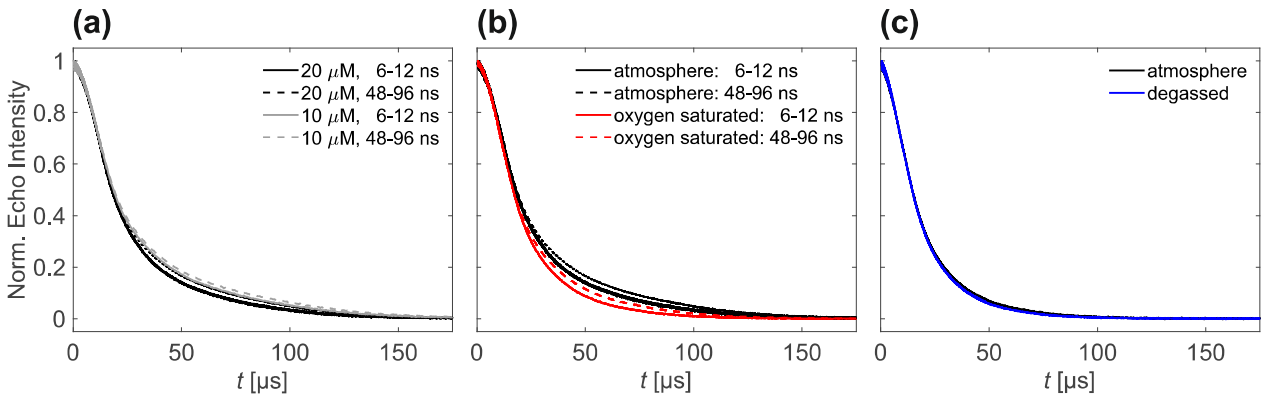

Figure Sa19 Hahn relaxation of OX071 in D_2O:glycerol-d_8 recorded at B_{max}. **(a)** Pulse-length dependent measurements acquired at 50 K for spin concentrations of 10 and 20 μM. **(b)** Comparison of flash-freezing under normal or an oxygen-saturated atmosphere by pulse-length dependent measurements acquired at 50 K for a spin concentration of 20 μM. **(c)** Effect of degassing the sample by ten freeze-pump-thaw cycles relative to flash-freezing the sample under ambient atmosphere. The measurement was performed at 110 K for a spin concentration of 10 μM and using pulse lengths of $t_\pi = t_{\pi/2} = 12$ ns.

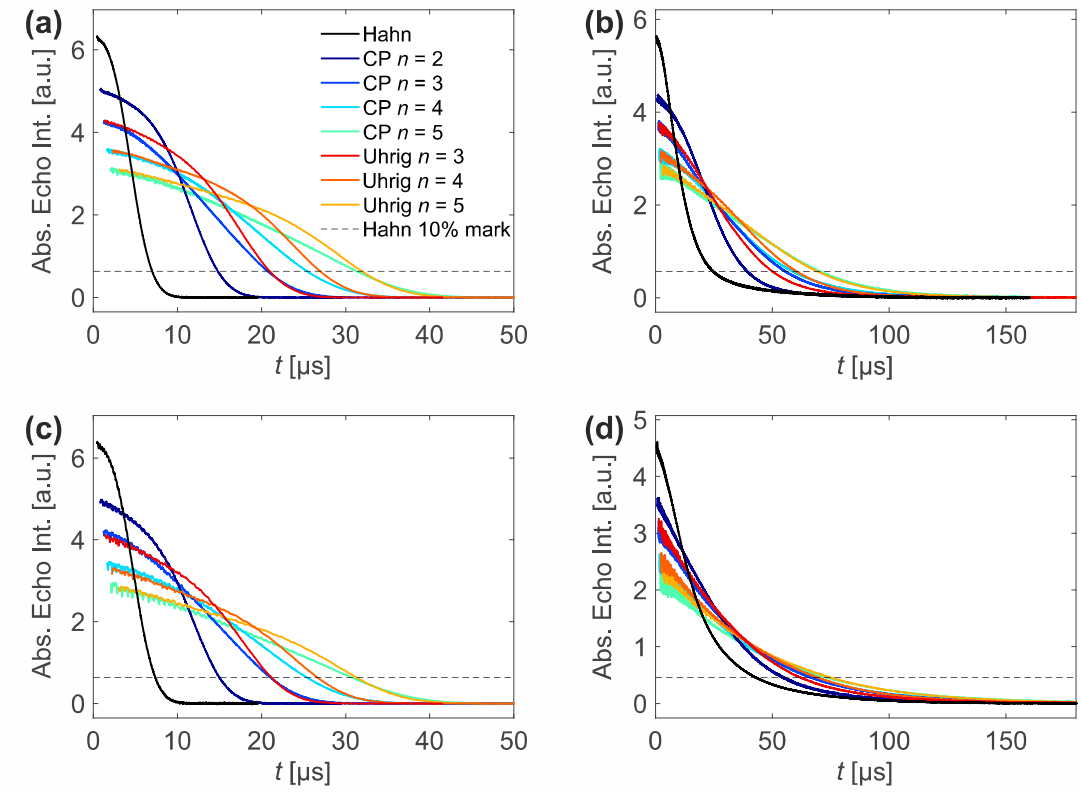

Figure Sa20 DD data sets of OX063 and OX071 recorded at a spin concentration of 10 μM and a temperature of 110 K at B_{max} using pulse lengths of $t_\pi = t_{\pi/2} = 12$ ns. **(a)** OX063 in H_2O:glycerol along with a legend that defines the color code for the DD experiments. **(b)** OX063 in D_2O:glycerol-d_8, **(c)** OX071 in H_2O:glycerol and **(d)** OX071 in D_2O:glycerol-d_8.

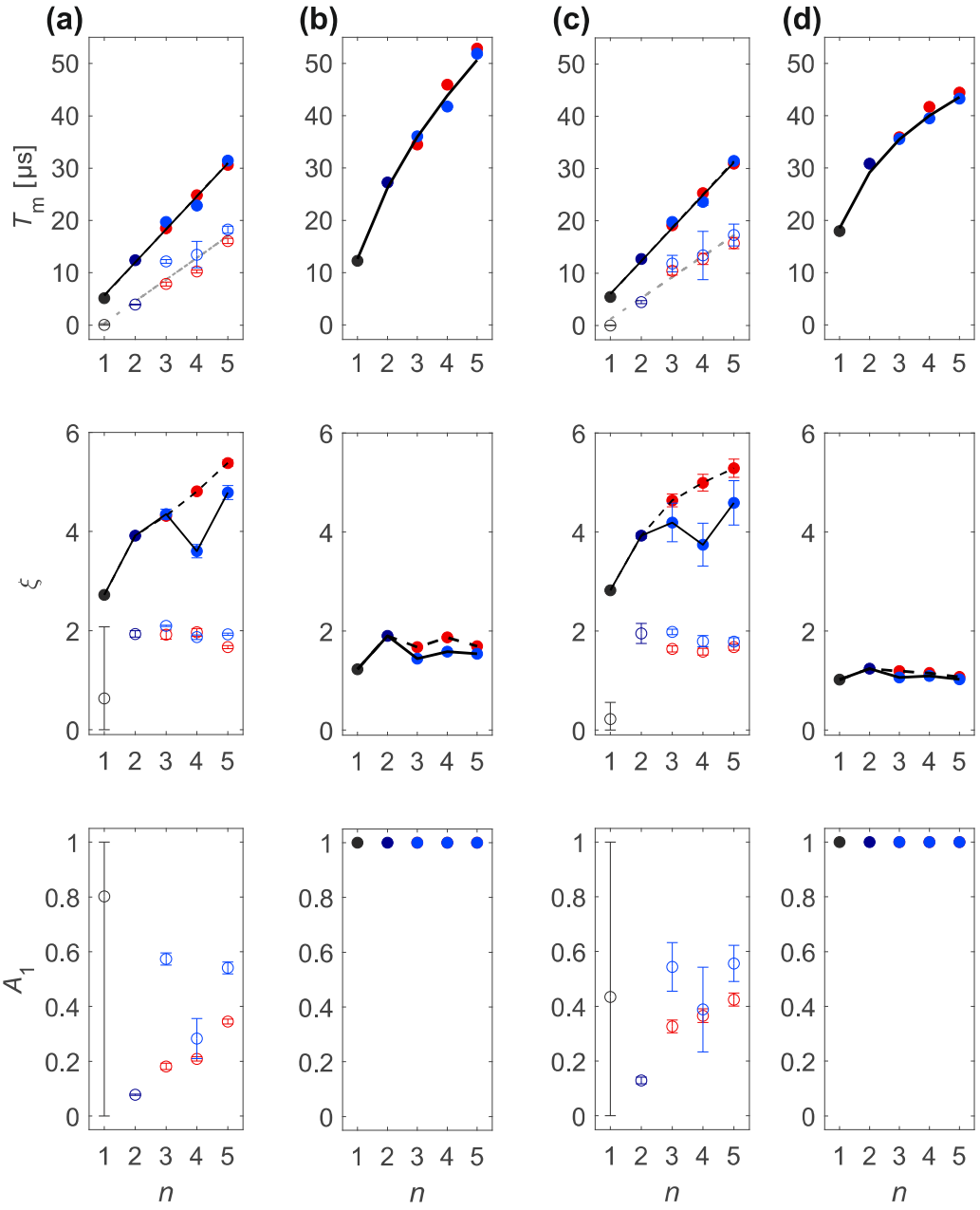

Figure Sa21 Stretched exponential(s) parameterization of DD data recorded at B_{max} and 110 K for OX063 and OX071 (10 μM) in water-glycerol glass: (a) SSE for OX063 in H_2O:glycerol, (b) SE for OX063 in D_2O:glycerol-d_8, (c) SSE for OX071 in H_2O:glycerol, (d) SE for OX071 in D_2O:glycerol-d_8. Each column displays the fitting parameters T_m, ξ, A_1 (top to bottom) with the associated 95% confidence intervals for a particular sample as a function of n. The color encodes the DD experiment with Hahn (●), CP/Uhrig $n = 2$ (●), CP $n > 2$ (●) and Uhrig $n > 2$ (●). SE parameters values are marked by filled circles, while for the SSE model empty circles correspond to the fast ($i = 1$), and filled to the slow ($i = 2$) relaxation contribution. Black lines shown in the ξ_i subplot serve as a guide for the eye to indicate the ξ_2 dependence on n for CP (solid) and Uhrig (dashed) experiments. For subplot corresponding to trityls in H_2O:glycerol, lines in the T_{m_i} subplots report linear regression results for experiment-specific T_{m_2} increase with n for CP (black, solid) and Uhrig (black, dashed), whereas a common T_{m_1} gain with n (grey, dashed) was determined and summarized in Table 1 in the main text. The SE model for trityls in D_2O:glycerol-d_8 results in a sub-linear increase of T_m with n, that is modeled by a power-law $\propto n^{\gamma}$ as reported in the main text.

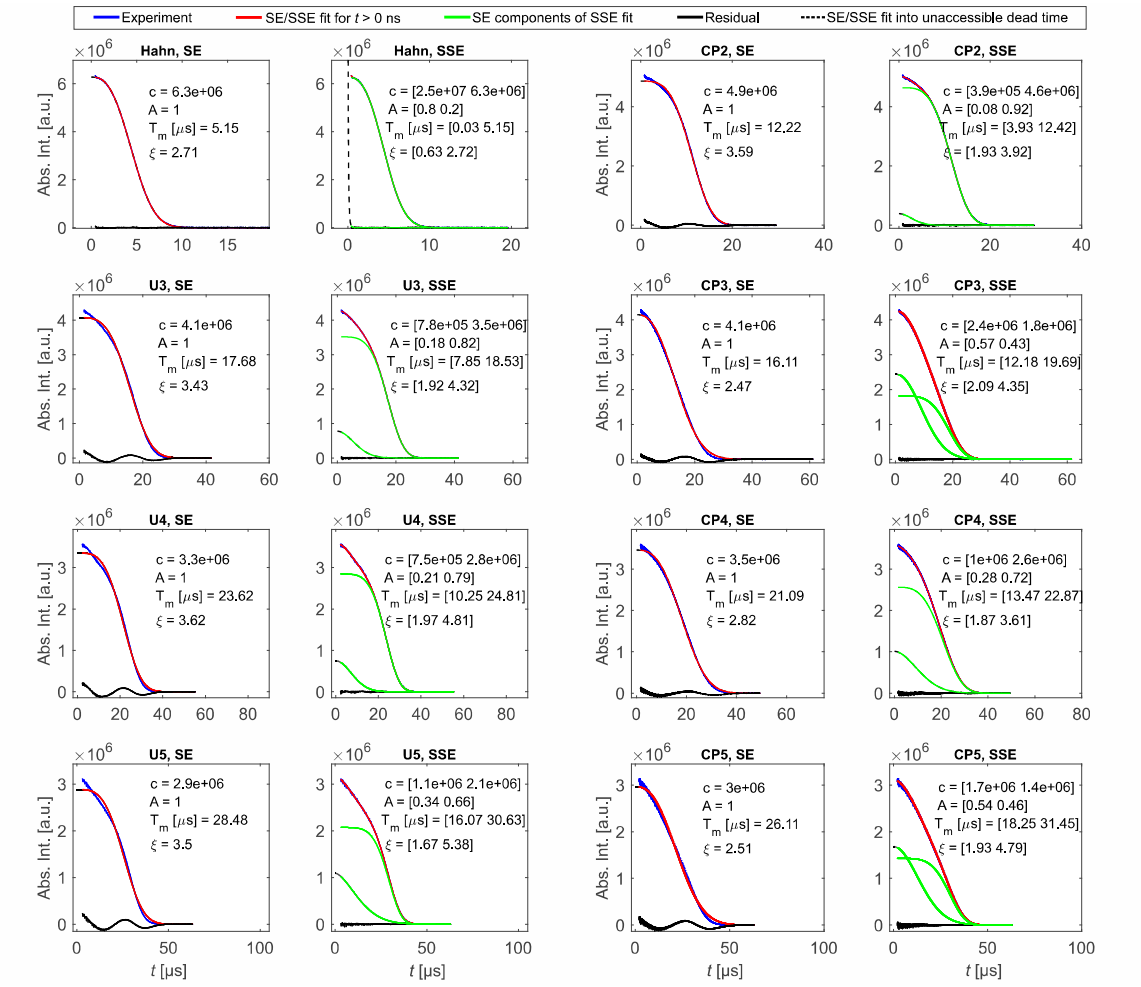

Figure Sa22 Comparison of an SE and SSE fit to the DD data of 10 μM OX063 in H_2O:glycerol recorded at 110 K and B_{max} with $t_\pi = t_{\pi/2} = 12$ ns.

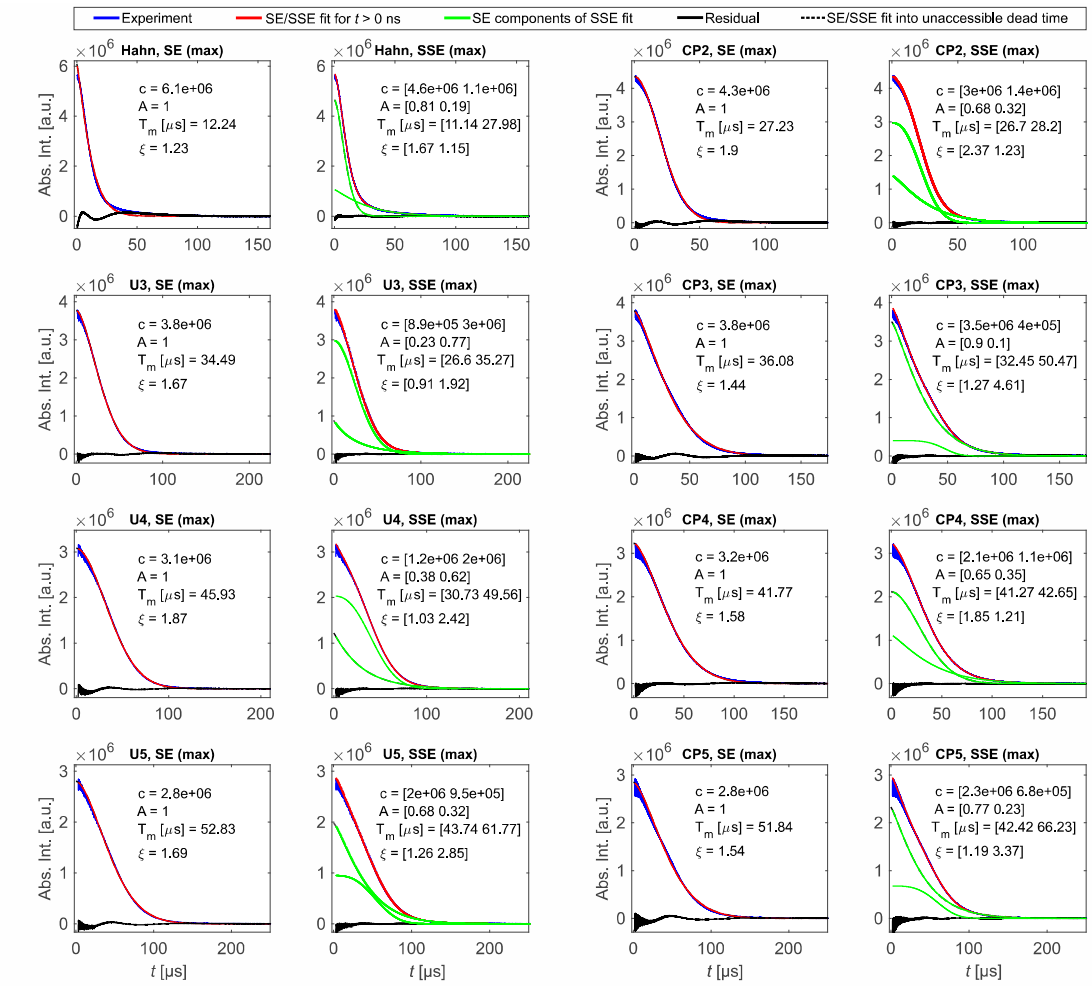

Figure Sa23 Comparison of an SE and SSE fit to the DD data of 10 μM OX063 in D_2O:glycerol-d_8 recorded at 110 K and B_{max} with $t_\pi = t_{\pi/2} = 12$ ns.

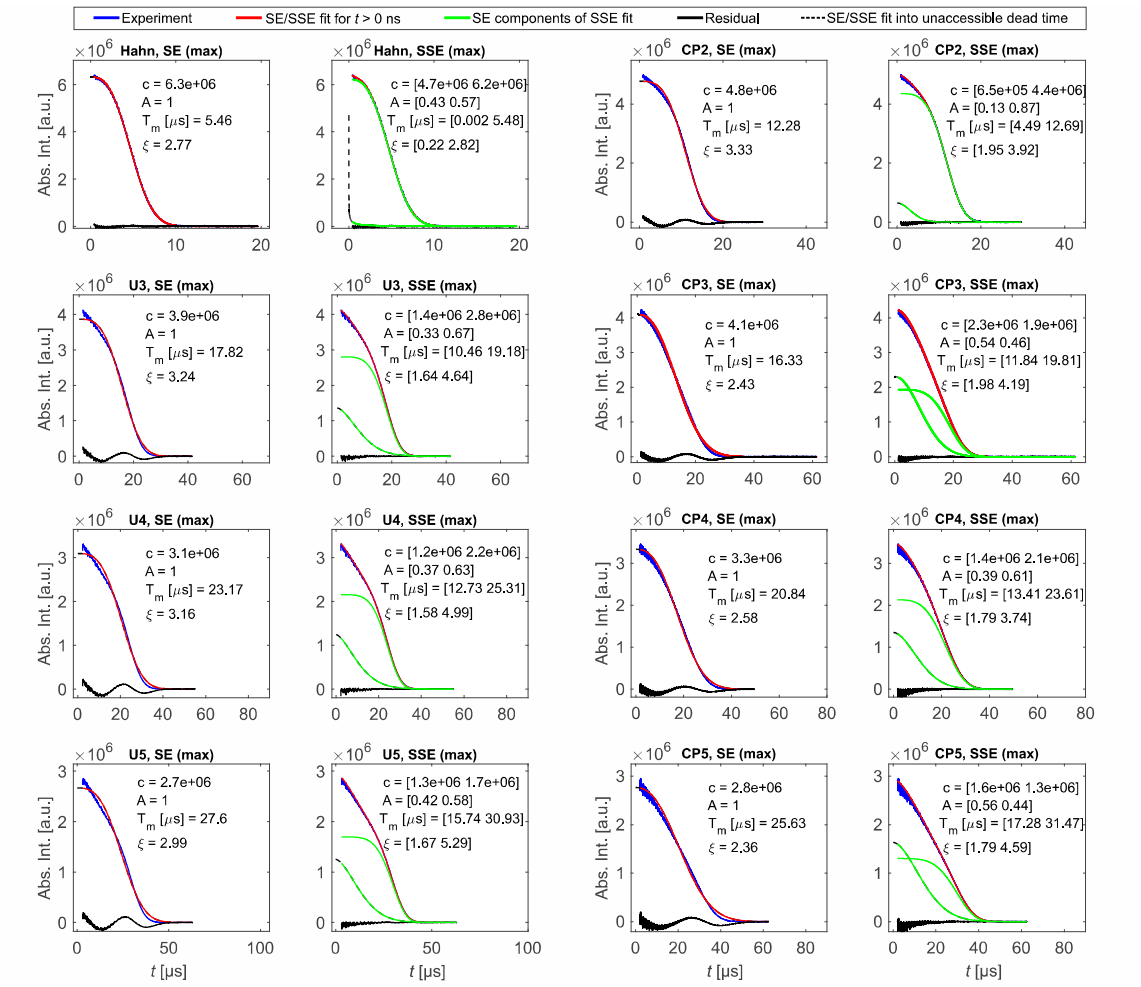

Figure Sa24 Comparison of an SE and SSE fit to the DD data of 10 μM OX071 in H_2O:glycerol recorded at 110 K and B_{max} with $t_\pi = t_{\pi/2} = 12$ ns.

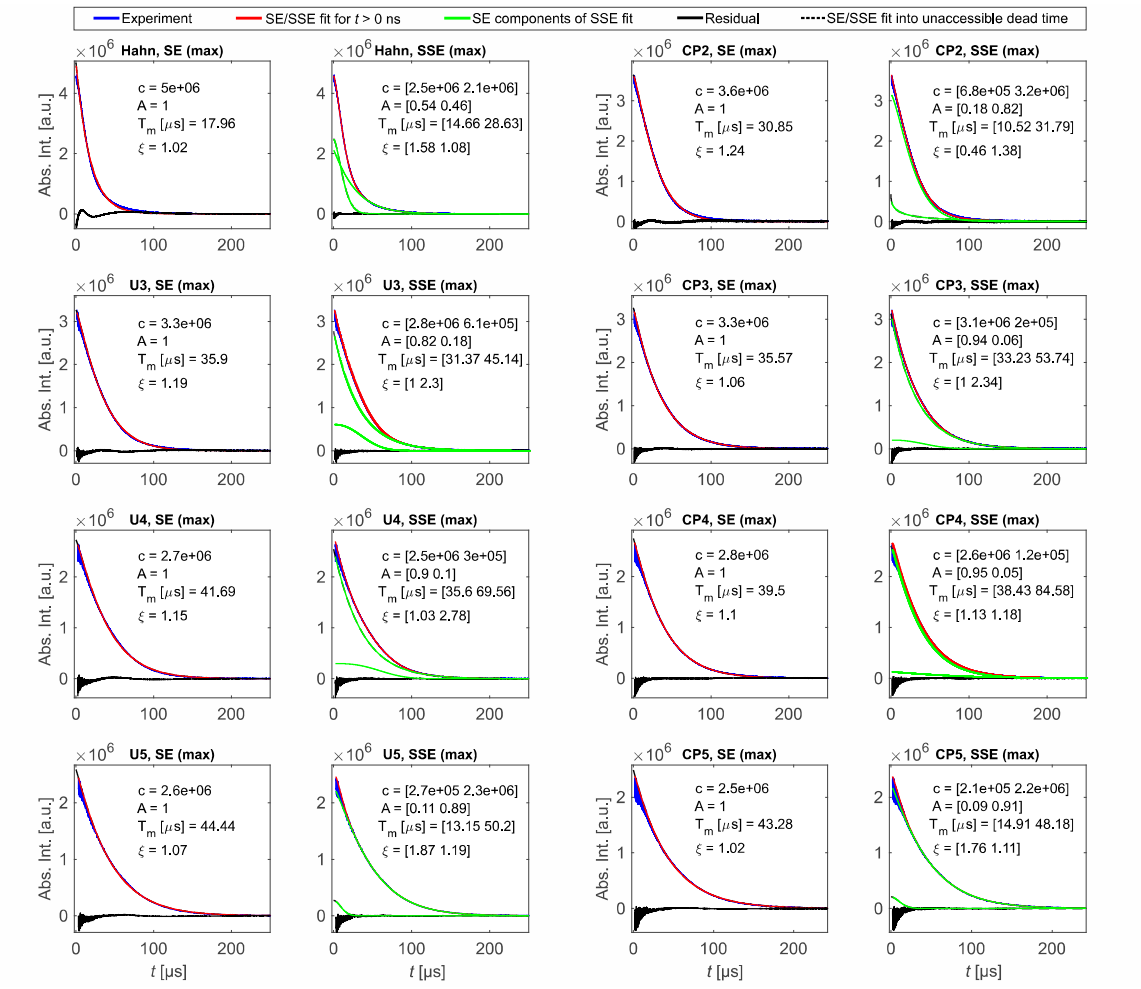

Figure Sa25 Comparison of an SE and SSE fit to the DD data of 10 μM OX071 in D_2O:glycerol-d_8 recorded at 110 K and B_{max} with $t_\pi = t_{\pi/2} = 12$ ns.

6 Gd(III) complexes: Gd-NO_3Pic, Gd-DOTA-M, Gd-PCTA

Based on the Q-band Hahn relaxation results presented in Fig. Sa26 in section 6.1 a concentration of 25 μM and a temperature of 10 K was chosen to determine the effect of the zero field splitting (ZFS) on the relaxation behavior under DD experiments. All experimental results are provided in section 6.2.

6.1 Concentration and temperature effect

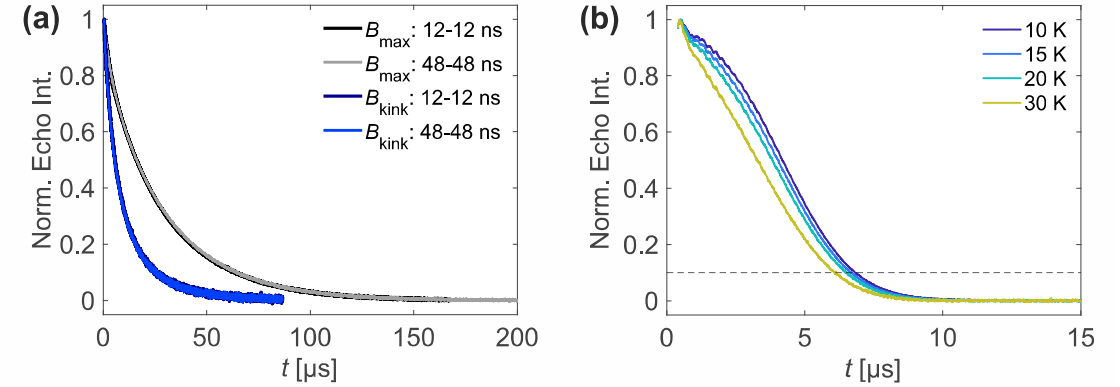

Figure Sa26 Q-band Hahn relaxation recorded at a spin concentration of 25 μM. **(a)** Pulse-length dependent relaxation of Gd-DOTA-M in D_2O:glycerol-d_8 at 10 K acquired at B_{max} and B_{kink} (-5 mT = -140 MHz relative to B_{max}). **(b)** Temperature-dependent relaxation of Gd-NO_3Pic in H_2O:glycerol recorded at B_{max}. The dashed line marks the 10% reference level to determine $T_{10\%}^{Hahn}$.

6.2 Dynamical decoupling at 10 K

All gadolinium DD measurements were acquired at Q band if not otherwise specified. The DD results recorded at B_{max} for Gd-NO_3Pic, Gd-DOTA-M and Gd-PCTA in H_2O:glycerol and Gd-DOTA-M in D_2O:glycerol-d_8 are shown in Fig. Sa27. According to Fig. Sa29, Sa30 and Sa31 the SSE expression is required to model the DD traces in H_2O:glycerol. For Gd-DOTA-M in D_2O:glycerol-d_8 the SE model is sufficient as evident from Fig. Sa32. Fig. Sa28 compares the scaling of the stretched exponential(s) parameter values with n for all four samples at B_{max}. Applying the refocusing pulses at B_{kink} instead of B_{max} deteriorates the refocusing effect as demonstrated for the protonated solvent in Fig. Sa34. Fig. Sa36, Sa37 and Sa38 show that the echo decays can be modeled by the SE expression, leading to a sub-linear increase of T_m with n as visible from Fig. Sa35 for all three gadolinium(III) complexes. The relative loss in coherence time at B_{kink} is expected to be even larger in D_2O:glycerol-d_8. Fig. Sa33 supports this claim by comparing the relaxation under the Hahn and CP $n = 2$ experiment for Gd-DOTA-M in H_2O:glycerol and D_2O:glycerol-d_8 at B_{max} and B_{kink}.

Performing the DD experiments at W band instead of Q band somewhat slows the decoherence at B_{max} due to a more selective excitation of the $|m_S| = 1/2$ transition as discussed in the main text. Fig. Sa39 shows this effect for Gd-NO_3Pic in H_2O:glycerol.

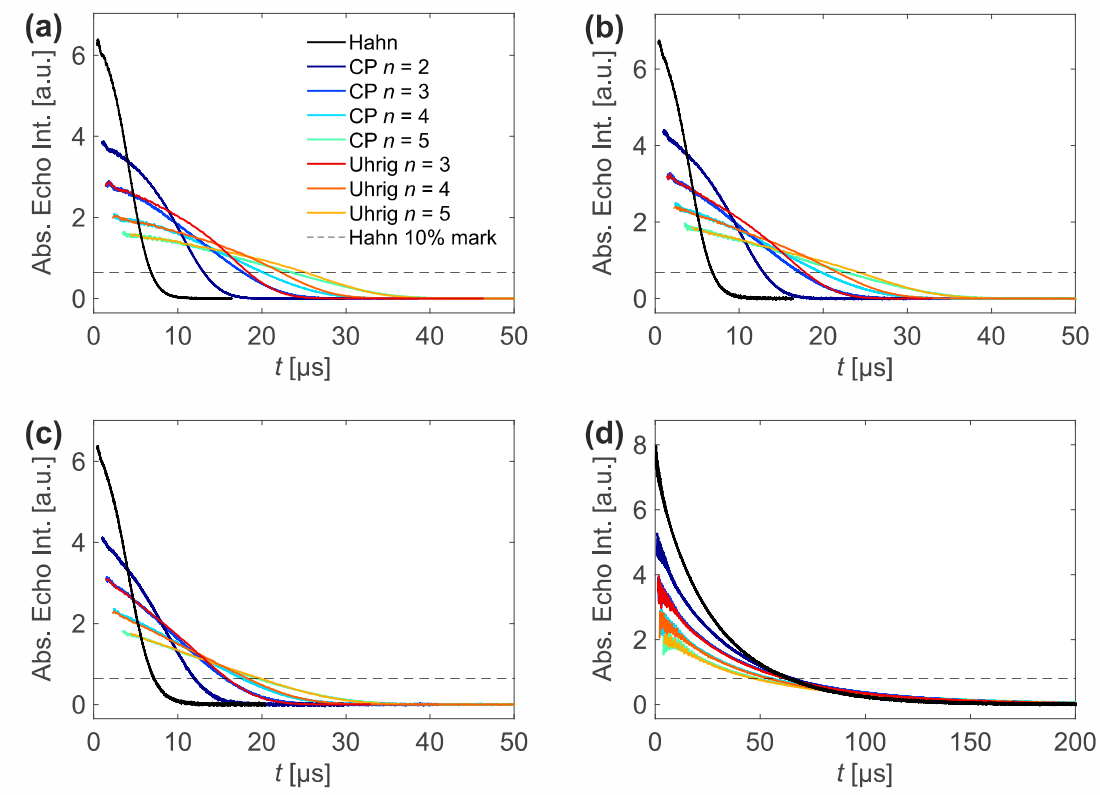

Figure Sa27 DD data sets of gadolinium(III) complexes recorded at a spin concentration of 25 μM and a temperature of 10 K at $B_{\max}$ using pulse lengths of $t_\pi = t_{\pi/2} = 12$ ns. **(a)** Gd-NO_3Pic in H_2O:glycerol along with a legend that defines the color code for the DD experiments. **(b)** Gd-DOTA-M in H_2O:glycerol, **(c)** Gd-PCTA in H_2O:glycerol and **(d)** Gd-DOTA-M in D_2O:glycerol-d_8.

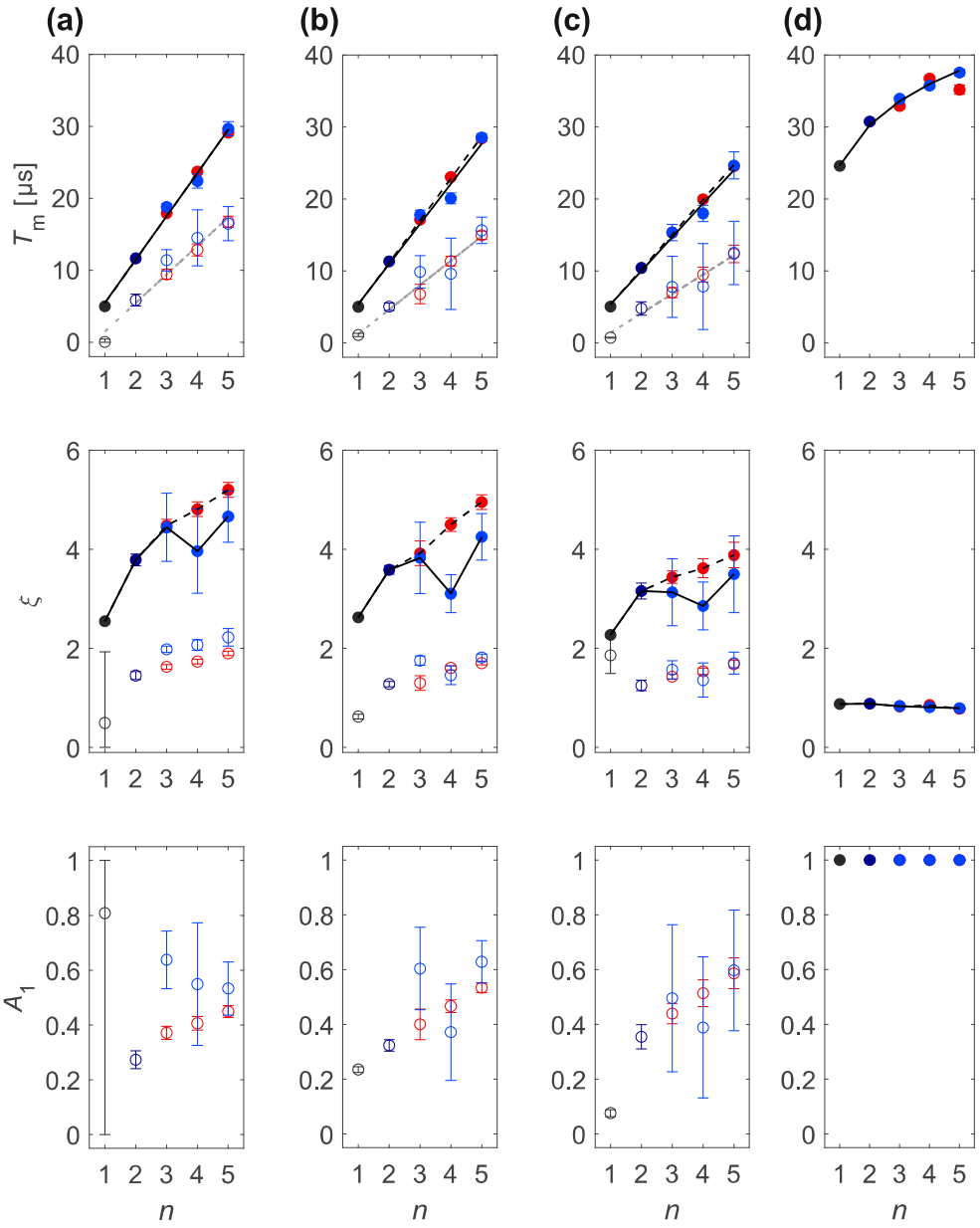

Figure Sa28 Stretched exponential(s) parameterization of DD data recorded at B_{max} and 10 K for Gd-NO_3Pic, Gd-DOTA-M and Gd-PCTA (25 μM) in water-glycerol glass: (a) SSE for Gd-NO_3Pic in H_2O:glycerol, (b) SSE for Gd-DOTA-M in H_2O:glycerol, (c) SSE for Gd-PCTA in H_2O:glycerol, (d) SE for Gd-DOTA-M in D_2O:glycerol-d_8. Each column displays the fitting parameters T_m, ξ, A_1 (top to bottom) with the associated 95% confidence intervals for a particular sample as a function of n. The color encodes the DD experiment with Hahn (●), CP/Uhrig $n = 2$ (●), CP $n > 2$ (●) and Uhrig $n > 2$ (●). SE parameters values are marked by filled circles, while for the SSE model empty circles correspond to the fast ($i = 1$), and filled to the slow ($i = 2$) relaxation contribution. Black lines shown in the ξ_i subplot serve as a guide for the eye to indicate the ξ_2 dependence on n for CP (solid) and Uhrig (dashed) experiments. For subplots corresponding to gadolinium(III) complexes in H_2O:glycerol, lines in the T_{m_i} subplots report linear regression results for experiment-specific T_{m_2} increase with n for CP (black, solid) and Uhrig (black, dashed), whereas a common T_{m_1} gain with n (grey, dashed) was determined and summarized in Table 1 in the main text. The SE model for Gd-DOTA-M in D_2O:glycerol-d_8 results in a sub-linear increase of T_m with n, that is modeled by a power-law $\propto n^{\gamma}$ as reported in the main text.

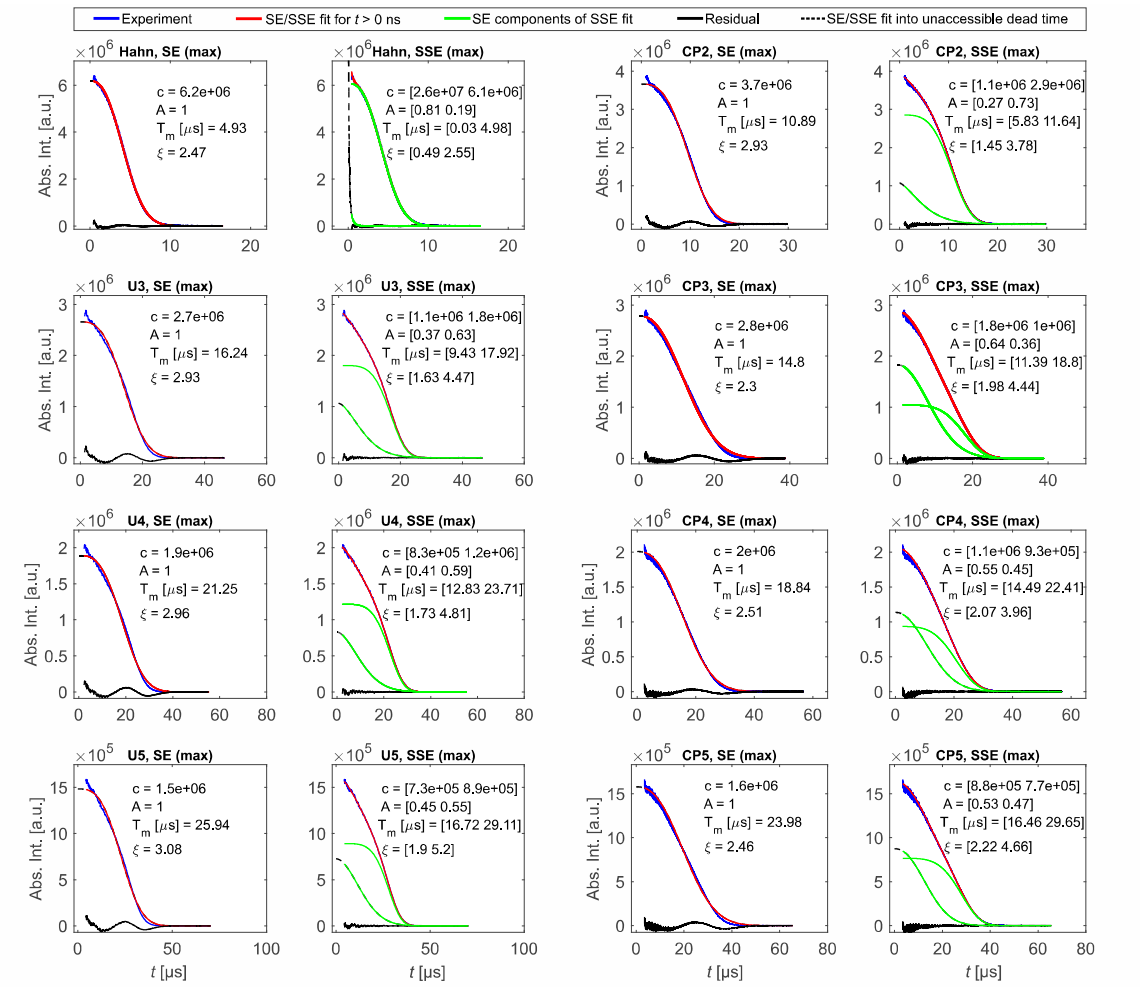

Figure Sa29 Comparison of an SE and SSE fit to the DD data of 25 μM Gd-NO_3Pic in H_2O:glycerol recorded at 10 K and B_{max} with $t_\pi = t_{\pi/2} = 12$ ns.

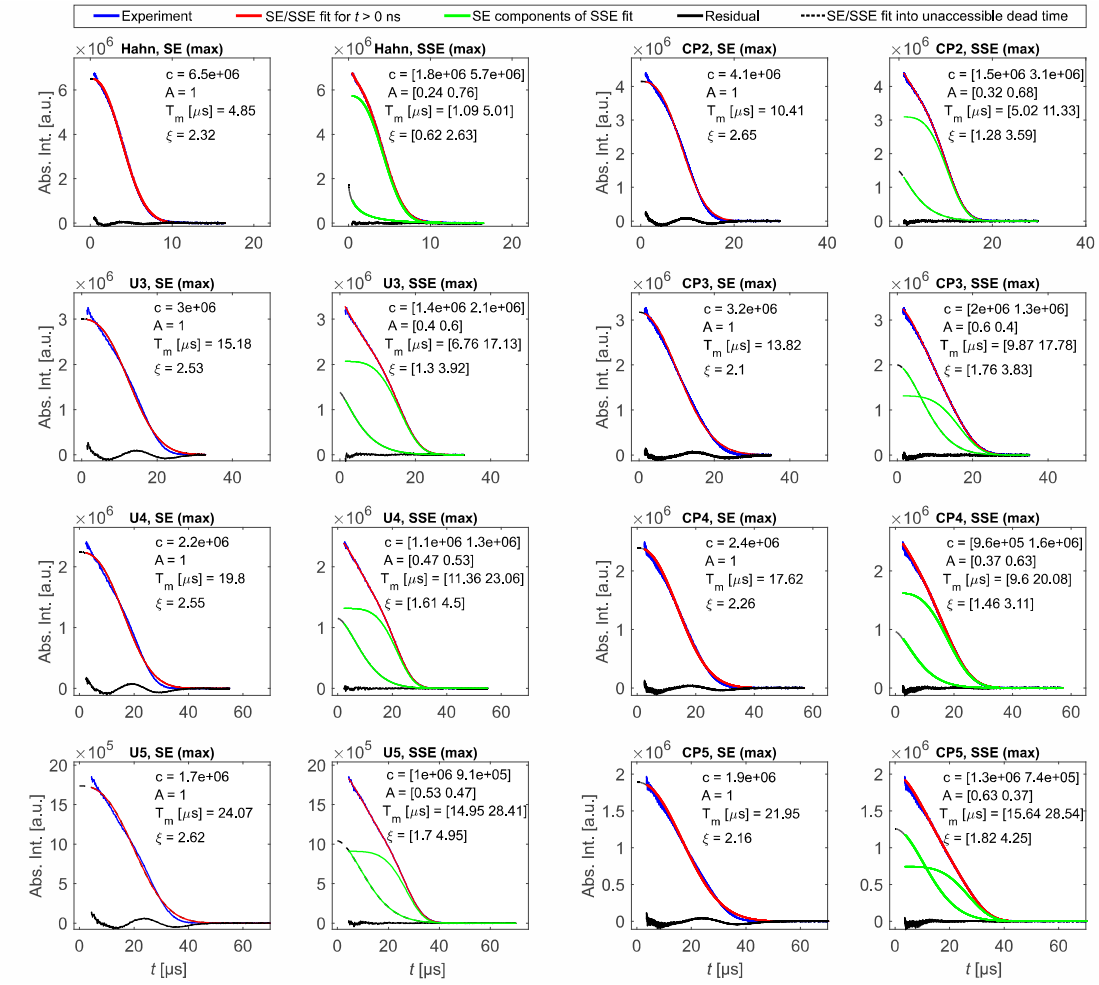

Figure Sa30 Comparison of an SE and SSE fit to the DD data of 25 μM Gd-DOTA-M in H_2O:glycerol recorded at 10 K and B_{max} with $t_\pi = t_{\pi/2} = 12$ ns.

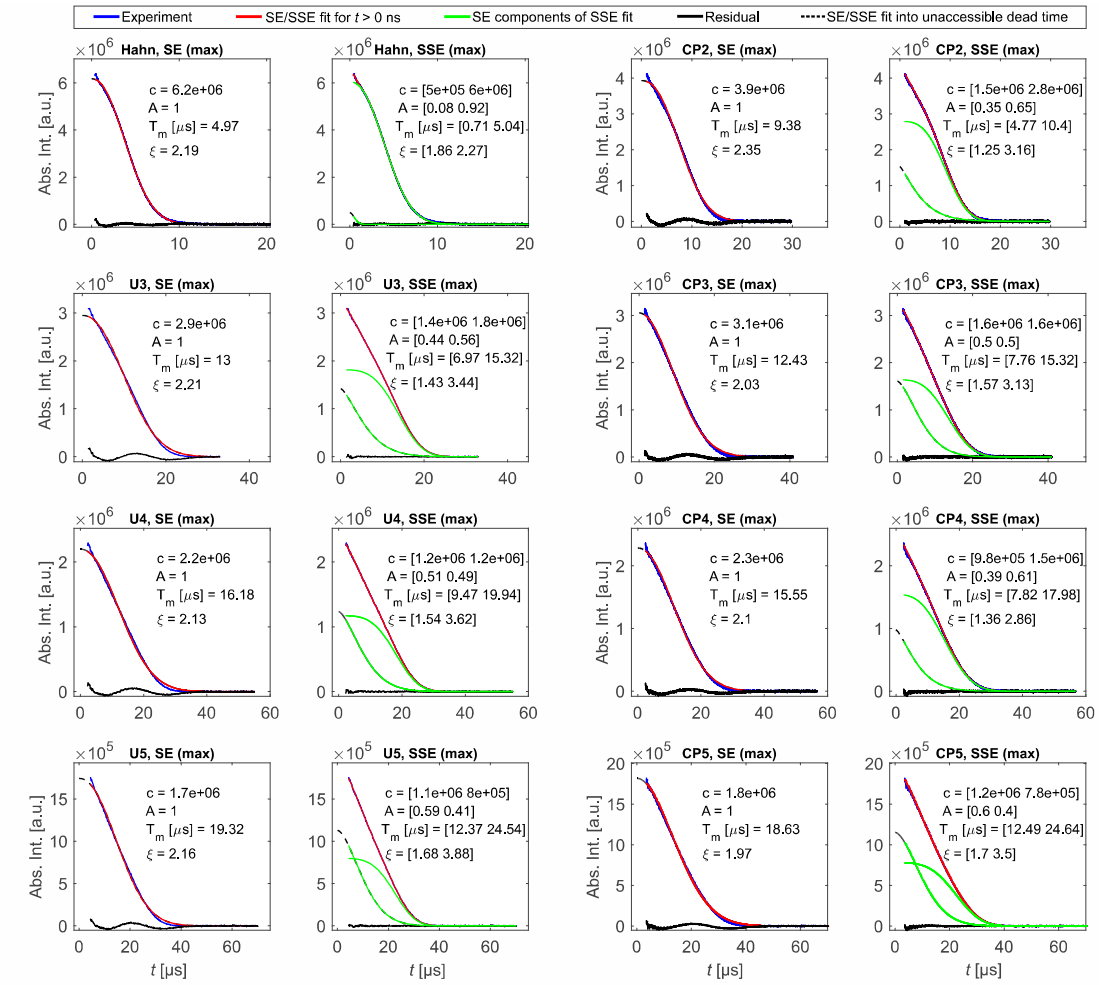

Figure Sa31 Comparison of an SE and SSE fit to the DD data of 25 μM Gd-PCTA in H_2O:glycerol recorded at 10 K and B_{max} with $t_\pi = t_{\pi/2} = 12$ ns.

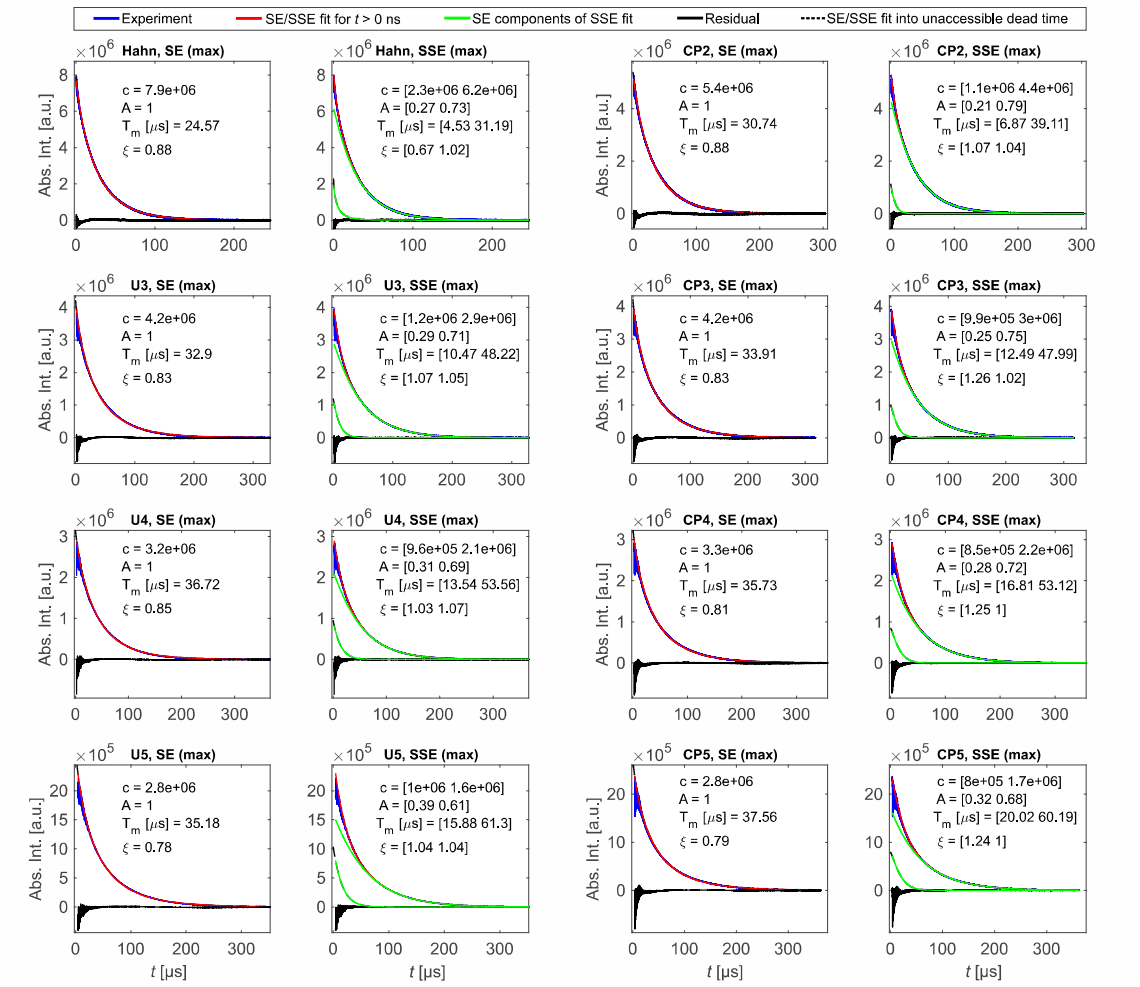

Figure Sa32 Comparison of an SE and SSE fit to the DD data of 25 μM Gd-DOTA-M in D_2O:glycerol-d_8 recorded at 10 K and B_{max} with $t_\pi = t_{\pi/2} = 12$ ns.

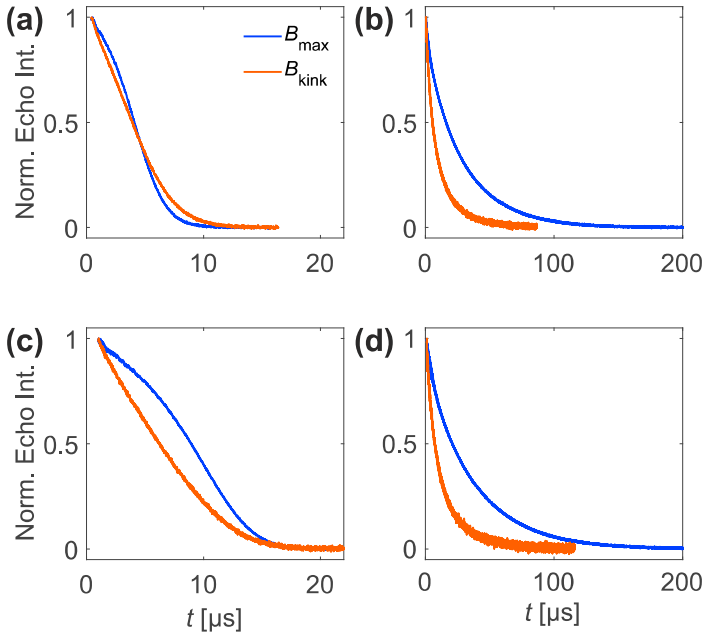

Figure Sa33 Difference between the relaxation behavior of Gd-DOTA-M recorded at B_{max} and B_{kink} (-5 mT = -140 MHz relative to B_{max}) with $t_\pi = t_{\pi/2} = 12$ ns. **(a)** Hahn relaxation of Gd-DOTA-M in H_2O:glycerol, **(b)** Hahn relaxation of Gd-DOTA-M in D_2O:glycerol-d_8, **(c)** CP $n = 2$ relaxation of Gd-DOTA-M in H_2O:glycerol and **(d)** CP $n = 2$ relaxation of Gd-DOTA-M in D_2O:glycerol-d_8.

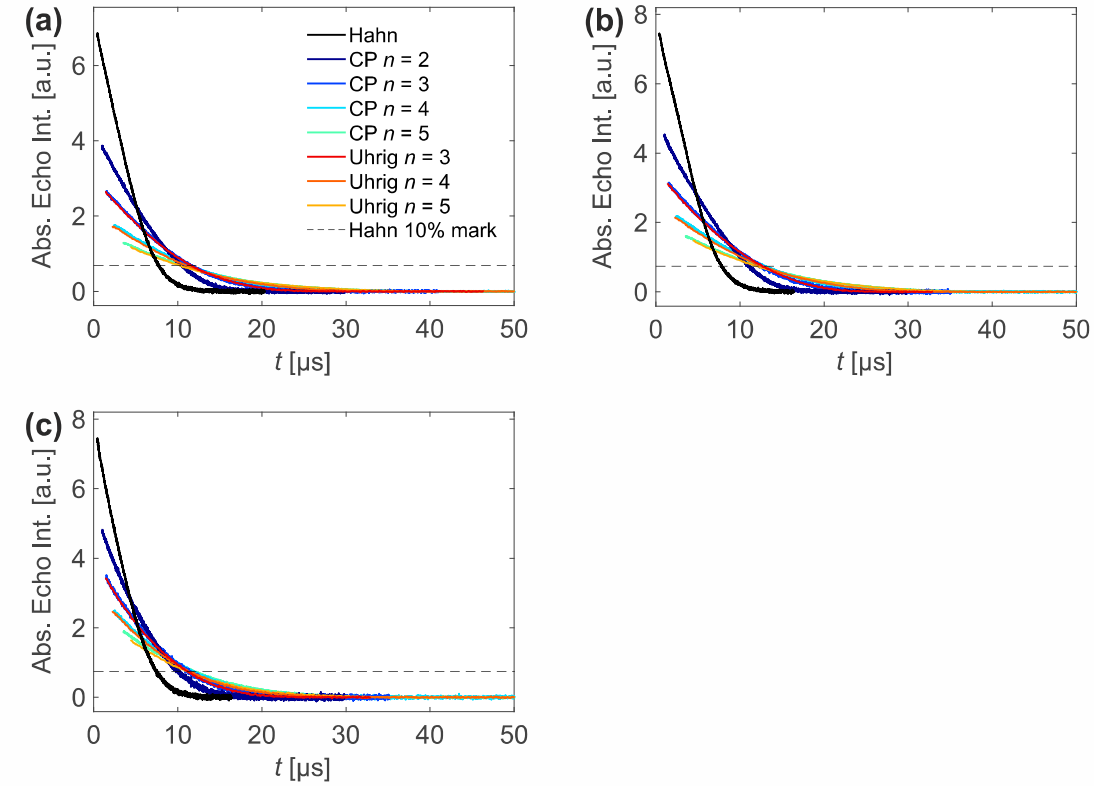

Figure Sa34 DD data sets of gadolinium(III) complexes in H_2O:glycerol recorded at a spin concentration of 25 μM and a temperature of 10 K at B_{kink} using pulse lengths of $t_\pi = t_{\pi/2} = 12$ ns. **(a)** Gd-NO_3Pic in H_2O:glycerol ($B_{kink} = B_{max}$ - 3.4 mT or - 95 MHz) along with a legend that defines the color code for the DD experiments. **(b)** Gd-DOTA-M in H_2O:glycerol ($B_{kink} = B_{max}$ - 5 mT or - 140 MHz) and **(c)** Gd-PCTA in H_2O:glycerol ($B_{kink} = B_{max}$ - 22 mT or - 616 MHz).

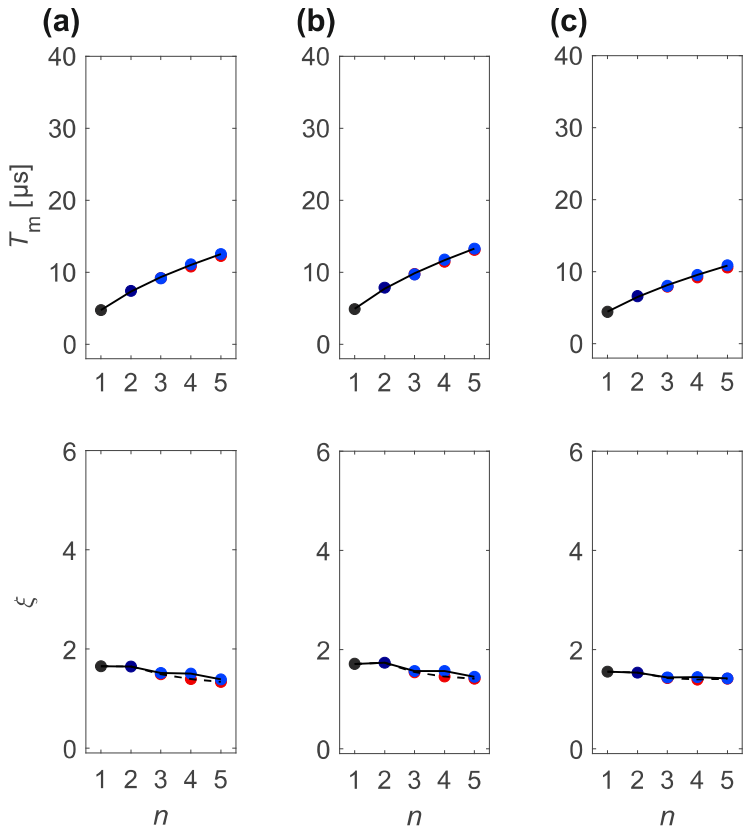

Figure Sa35 SE parameterization of DD data recorded at B_{kink} and 10 K for Gd-NO_3Pic, Gd-DOTA-M and Gd-PCTA (25 μM) in H_2O:glycerol: (a) Gd-NO_3Pic in H_2O:glycerol ($B_{\mathrm{kink}} = B_{\mathrm{max}}$ - 3.4 mT or - 95 MHz) , (b) Gd-DOTA-M in H_2O:glycerol ($B_{\mathrm{kink}} = B_{\mathrm{max}}$ - 5 mT or - 140 MHz) and (c) Gd-PCTA in H_2O:glycerol ($B_{\mathrm{kink}} = B_{\mathrm{max}}$ - 22 mT or - 616 MHz). Each column displays the fitting parameters T_{m}, ξ, A_1 (top to bottom) with the associated 95% confidence intervals for a particular sample as a function of n. The color encodes the DD experiment with Hahn (●), CP/Uhrig $n = 2$ (●), CP $n > 2$ (●) and Uhrig $n > 2$ (●). Black lines shown in the ξ subplot serve as a guide for the eye to indicate the ξ dependence on n for CP (solid) and Uhrig (dashed) experiments. The relationship between T_{m} and n is modelled by a power-law $\propto n^{\gamma}$ with γ values between 0.5 and 0.6.

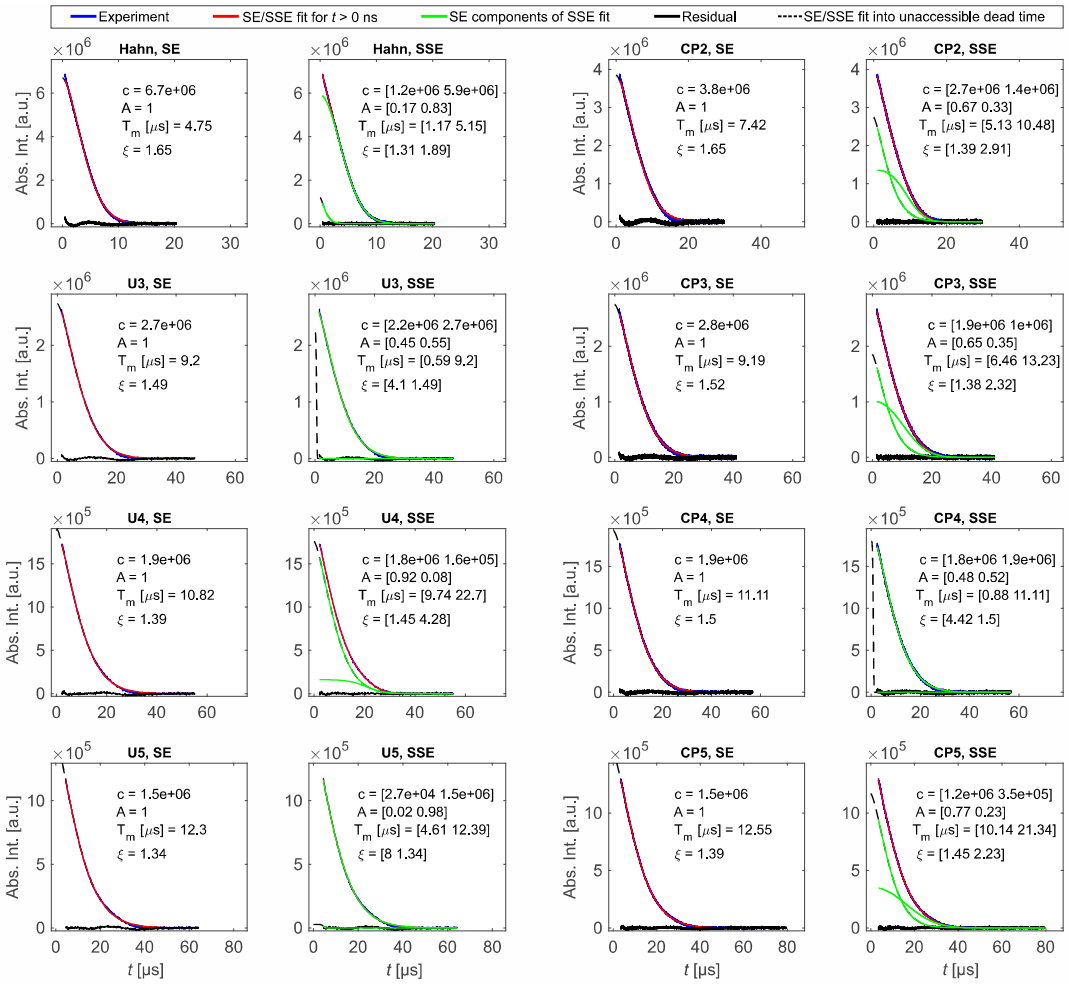

Figure Sa36 Comparison of an SE and SSE fit to the DD data of 25 μM Gd-NO_3Pic in H_2O:glycerol recorded at 10 K and B_{kink} ($= B_{\mathrm{max}}$ - 3.4 mT or - 95 MHz) with $t_\pi = t_{\pi/2} = 12$ ns.

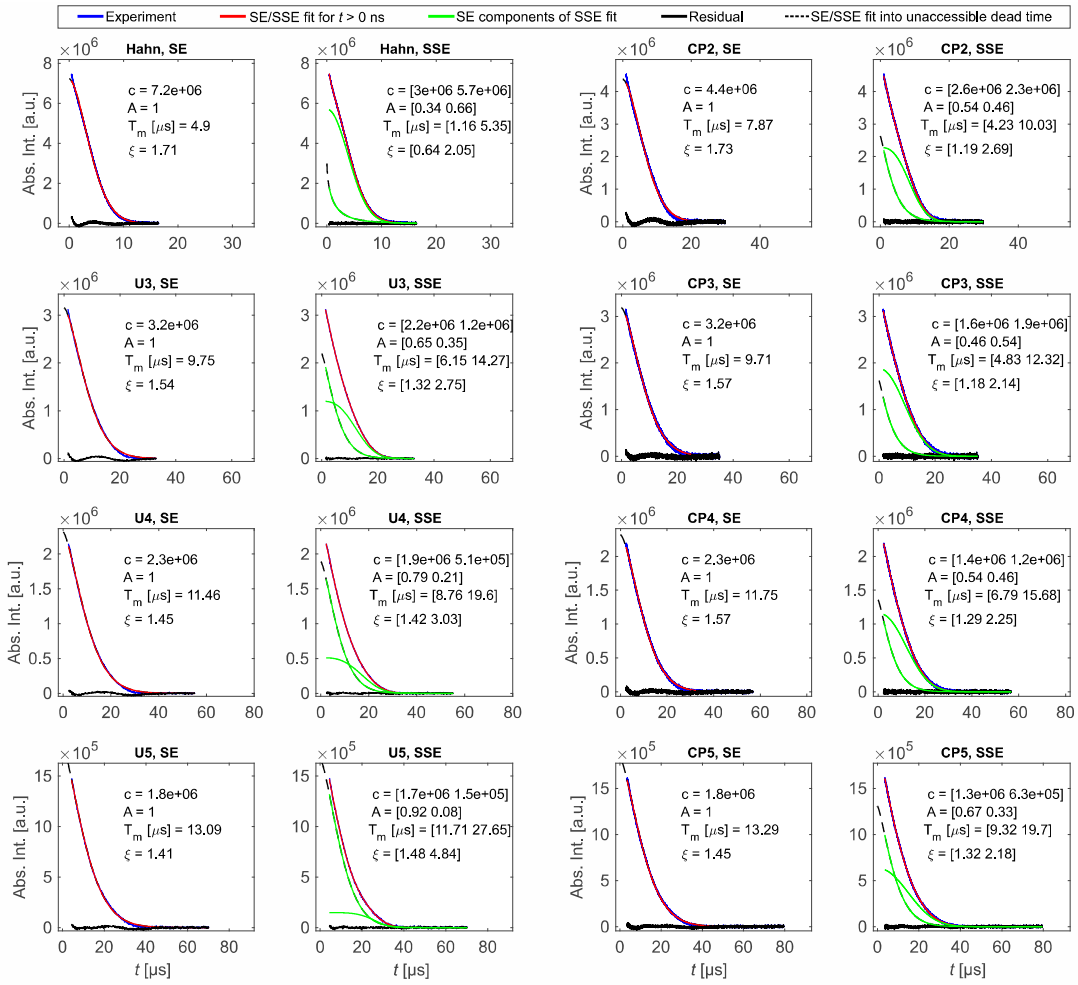

Figure Sa37 Comparison of an SE and SSE fit to the DD data of 25 μM Gd-DOTA-M in H_2O:glycerol recorded at 10 K and B_{kink} ($= B_{\mathrm{max}}$ - 5 mT or - 140 MHz) with $t_\pi = t_{\pi/2} = 12$ ns.

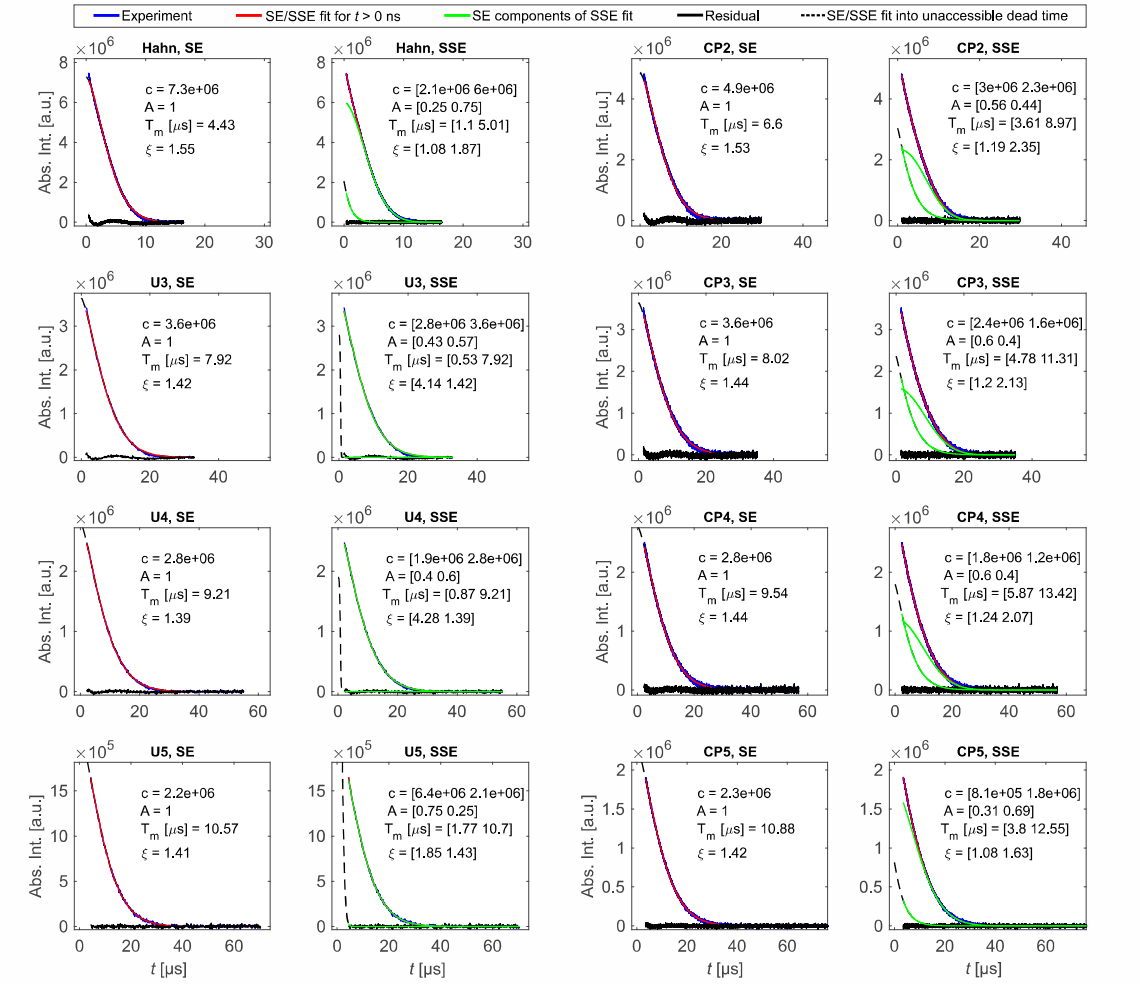

Figure Sa38 Comparison of an SE and SSE fit to the DD data of 25 μM Gd-PCTA in H_2O:glycerol recorded at 10 K and B_{kink} ($= B_{\mathrm{max}}$ - 22 mT or - 616 MHz) with $t_\pi = t_{\pi/2} = 12$ ns.

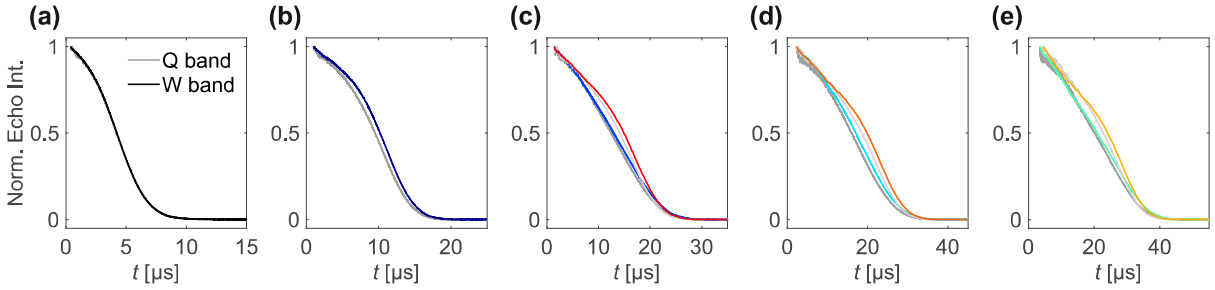

Figure Sa39 Comparison between Q- and W-band DD results for 25 μM Gd-NO_3Pic in H_2O:glycerol recorded at 10 K and B_{kink}. Due to the different time resolution of the spectrometers, the Q-band data was acquired using pulse lengths with $t_\pi = t_{\pi/2} = 12$ ns, while the W-band pulse lengths are $t_\pi = t_{\pi/2} = 16$ ns. The traces are separately displayed by number of pulses n with **(a)** Hahn, **(b)** CP $n = 2$, **(c)** CP and Uhrig $n = 3$, **(d)** CP (cyan) and Uhrig $n = 4$ and **(d)** CP and Uhrig $n = 5$. The colored traces correspond to the W-band data using the same color code as defined in legend in Fig. Sa34**(a)**, while the darker (CP) and lighter (Uhrig) grey represent the Q-band results.

References

[1] R. F. Heck, *Palladium reagents in organic syntheses*, Academic Press, New York, 1985, p. 18.

[2] M. Qi, M. Hülsmann and A. Godt, *The Journal of Organic Chemistry*, 2016, **81**, 2549–2571.

[3] K. Oyaizu, T. Kawamoto, T. Suga and H. Nishide, *Macromolecules*, 2010, **43**, 10382–10389.

[4] I. A. Kirilyuk, Y. F. Polienko, O. A. Krumkacheva, R. K. Strizhakov, Y. V. Gatilov, I. A. Grigor'ev and E. G. Bagryanskaya, *The Journal of Organic Chemistry*, 2012, **77**, 8016–8027.

[5] I. Ritsch, H. Hintz, G. Jeschke, A. Godt and M. Yulikov, *Physical Chemistry Chemical Physics*, 2019, **21**, 9810–9830.

[6] K. Keller, I. Ritsch, H. Hintz, M. Hülsmann, M. Qi, F. D. Breitgoff, D. Klose, Y. Polyhach, M. Yulikov, A. Godt and G. Jeschke, *Physical Chemistry Chemical Physics*, 2020, **22**, 21707–21730.

[7] L. Fábregas Ibáñez, G. Jeschke and S. Stoll, *Magnetic Resonance*, 2020, **1**, 209–224.

[8] T. von Hagens, Y. Polyhach, M. Sajid, A. Godt and G. Jeschke, *Physical Chemistry Chemical Physics*, 2013, **15**, 5854.

[9] M. Lindgren, G. R. Eaton, S. S. Eaton, B.-H. Jonsson, P. Hammarström, M. Svensson and U. Carlsson, *Journal of the Chemical Society, Perkin Transactions 2*, 1997, 2549–2554.

[10] J. Soetbeer, M. Hülsmann, A. Godt, Y. Polyhach and G. Jeschke, *Physical Chemistry Chemical Physics*, 2018, **20**, 1615–1628.

Supporting Information - Part B

Dynamical decoupling in water-glycerol glasses: a comparison of nitroxides, trityl radicals and gadolinium complexes

Janne Soetbeer,[a] Marthe Millen,[a] Konstantin Zouboulis,[a] Miriam Hülsmann,[b] Adelheid Godt,[b] Yevhen Polyhach,[a] and Gunnar Jeschke[a]

7. Figures of NMR spectra

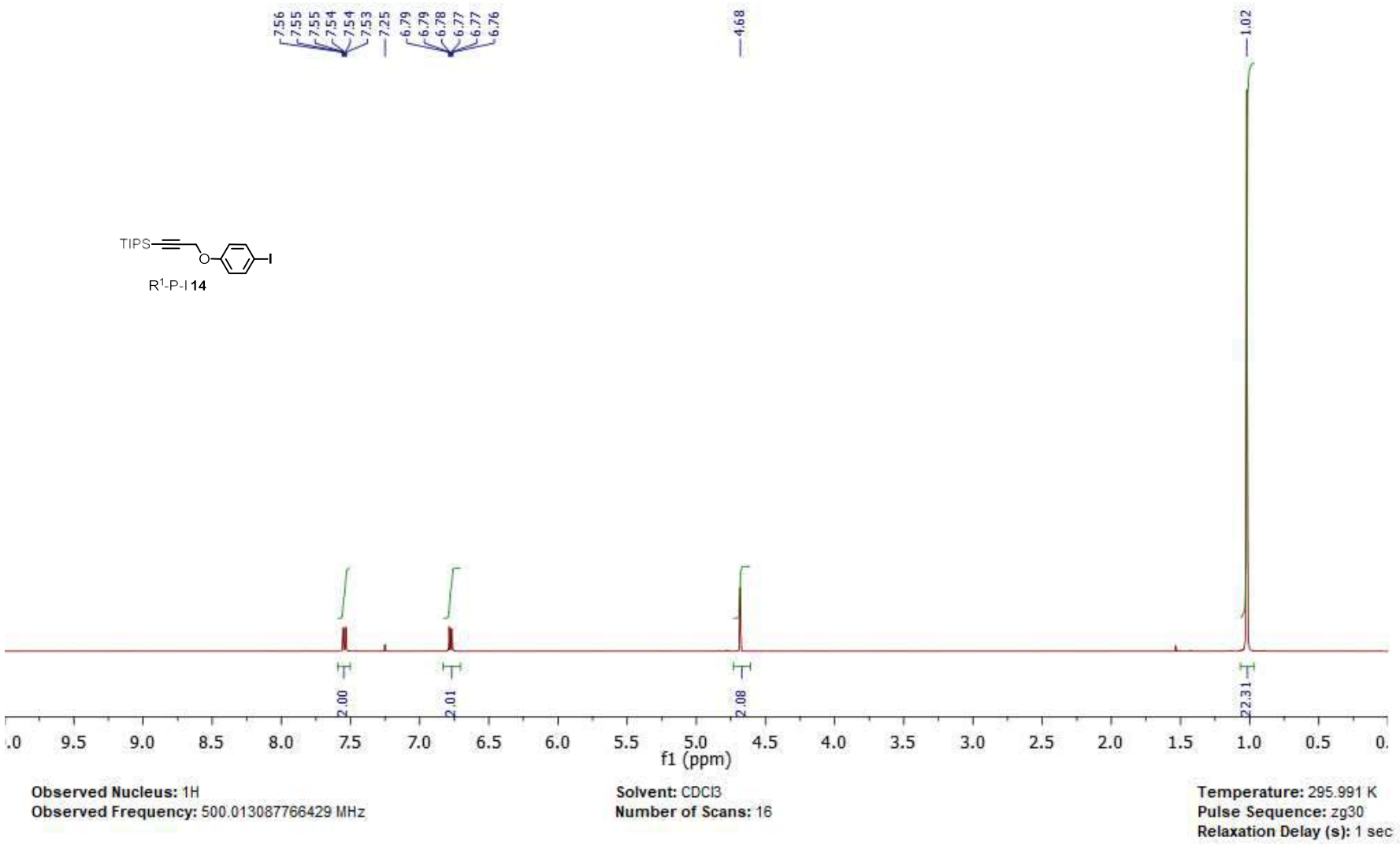

Figure Sb1a. ^{1}H NMR spectrum of R^{1}-P-I **14** in $CDCl_3$.

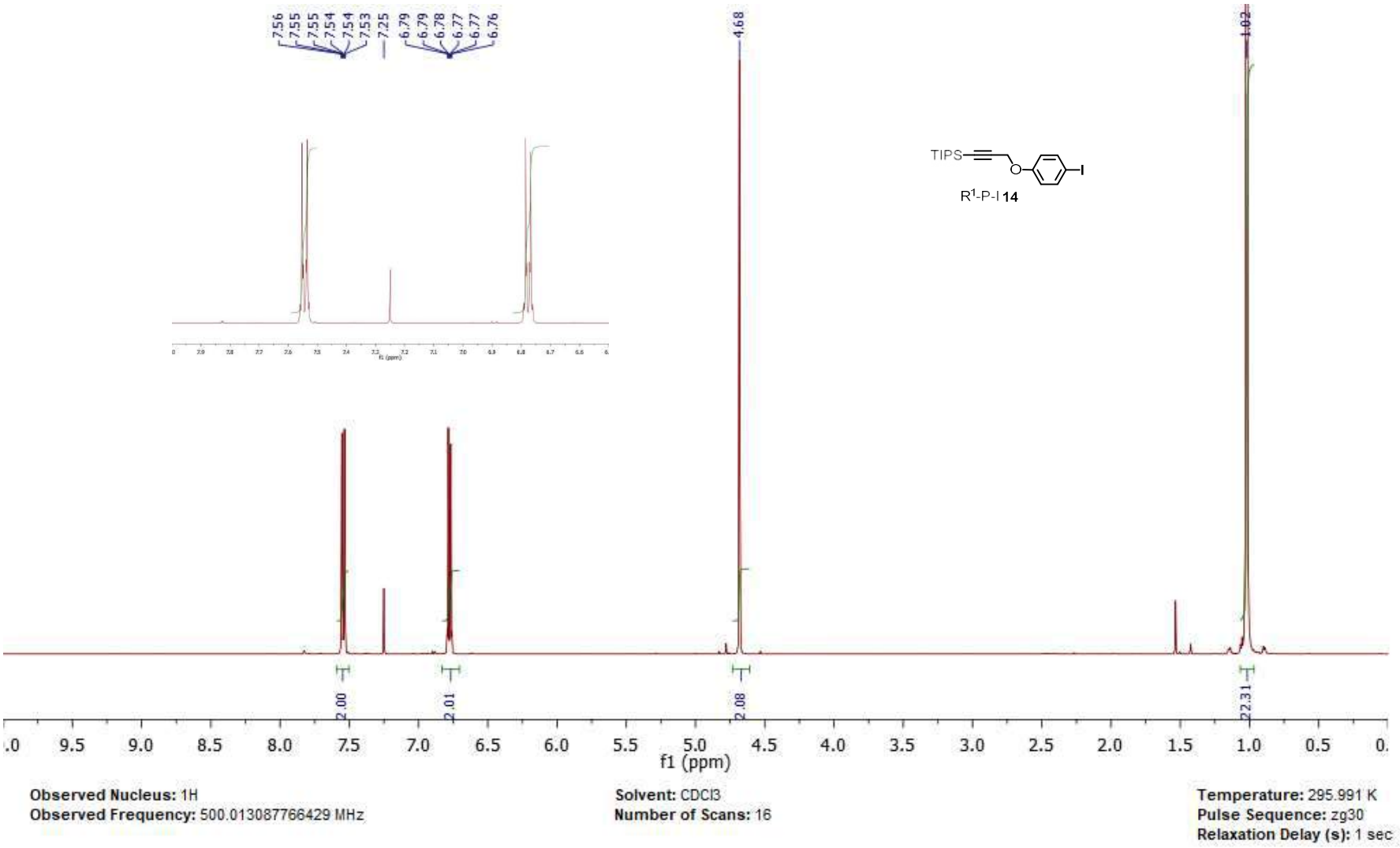

Figure Sb1b. ^{1}H NMR spectrum of R^{1}-P-I **14** in $CDCl_3$.

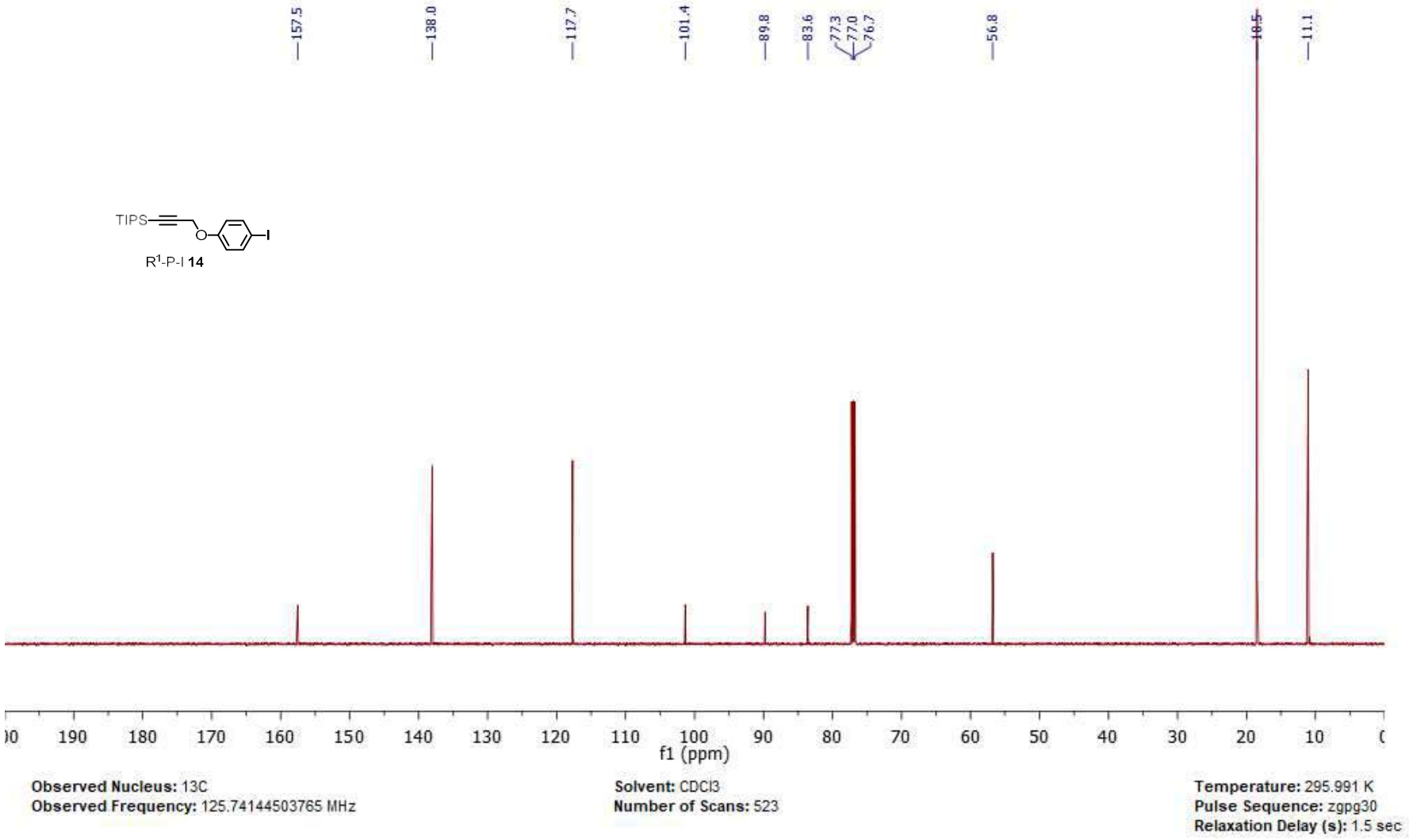

Figure Sb1c. ^{13}C NMR spectrum of R^1-P-I **14** in $CDCl_3$.

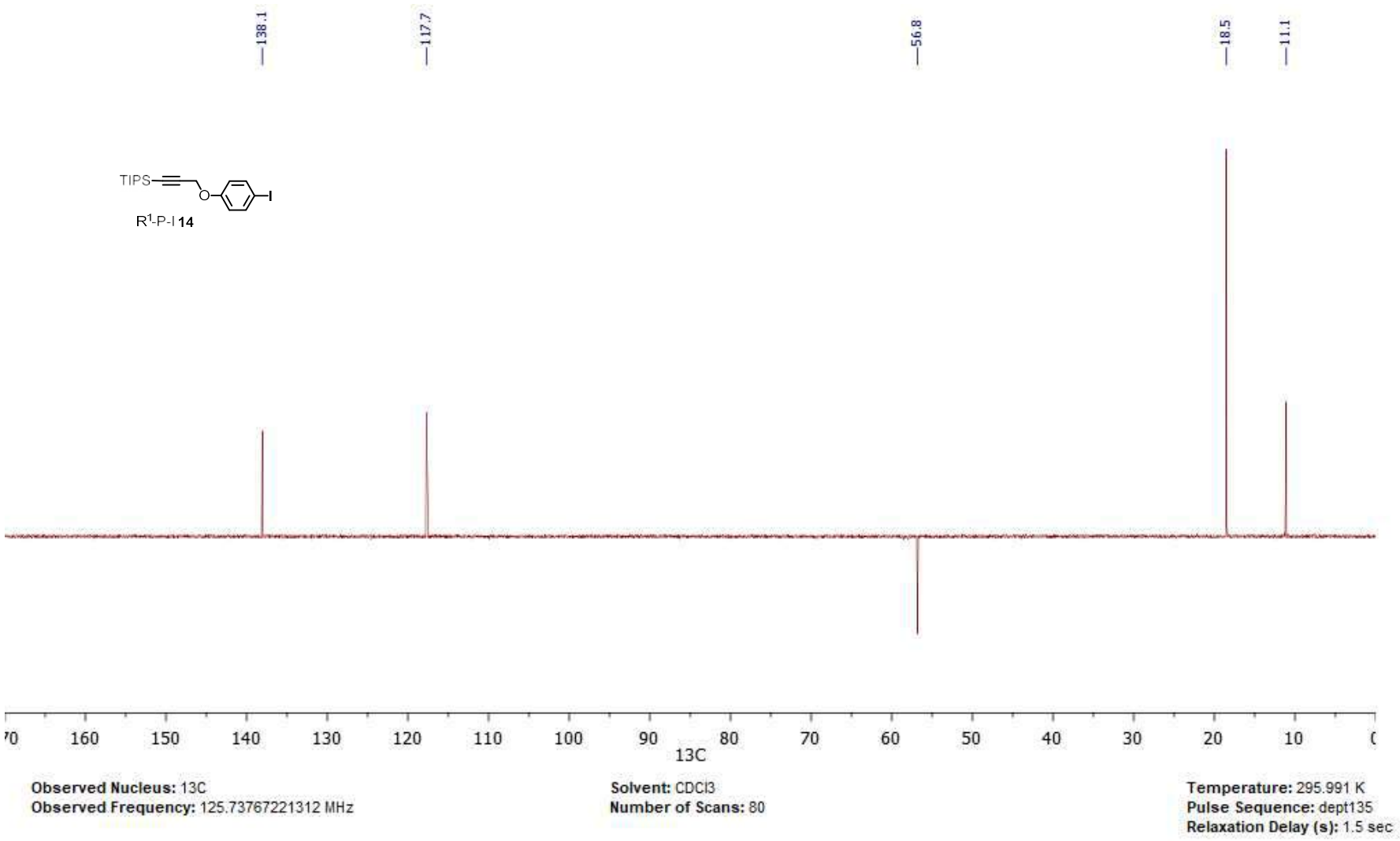

Figure Sb1d. ^{13}C DEPT-135 NMR spectrum of R^1-P-I **14** in $CDCl_3$.

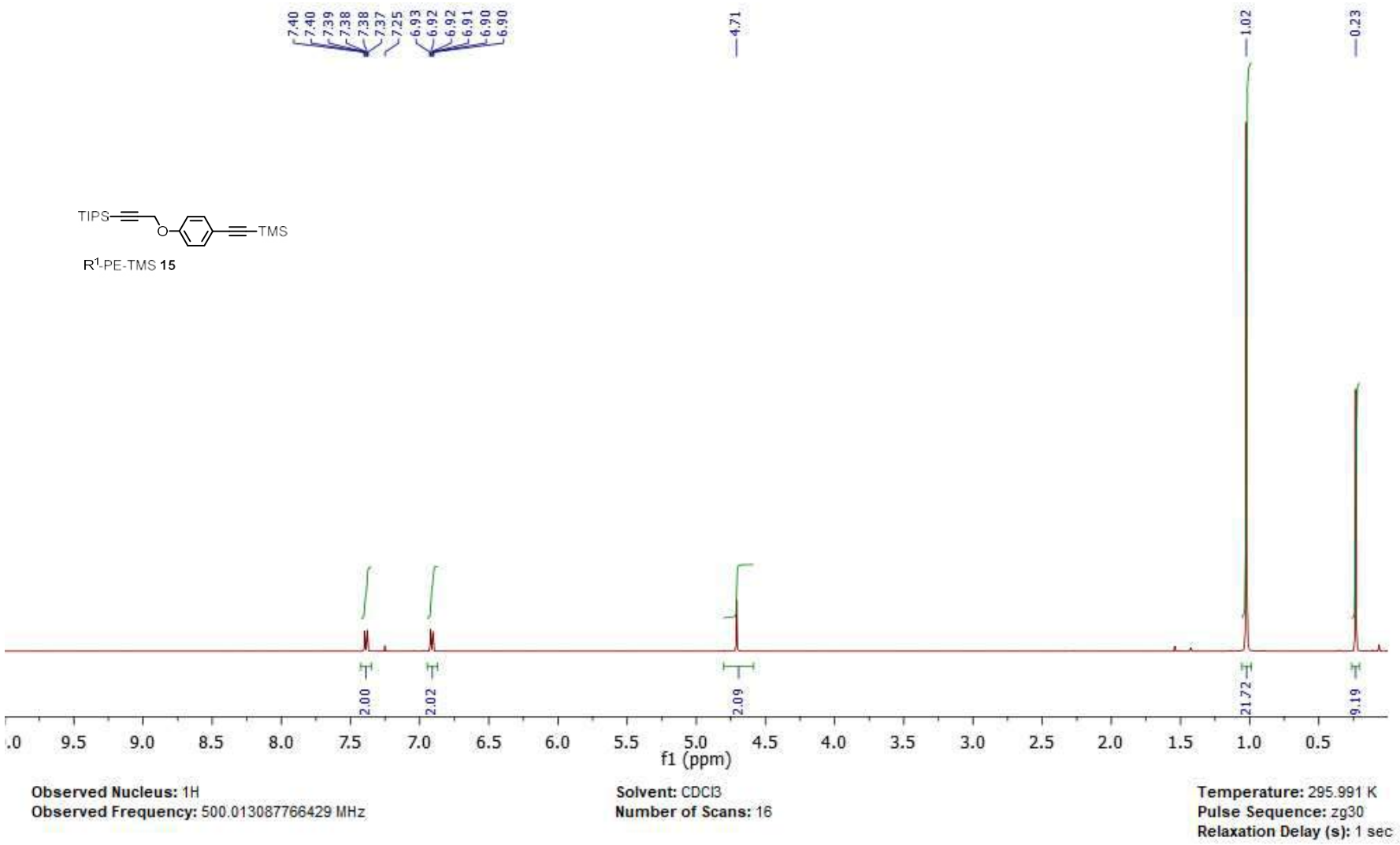

Figure Sb2a. ^{1}H NMR spectrum of R^{1}-PE-TMS **15** in $CDCl_3$.

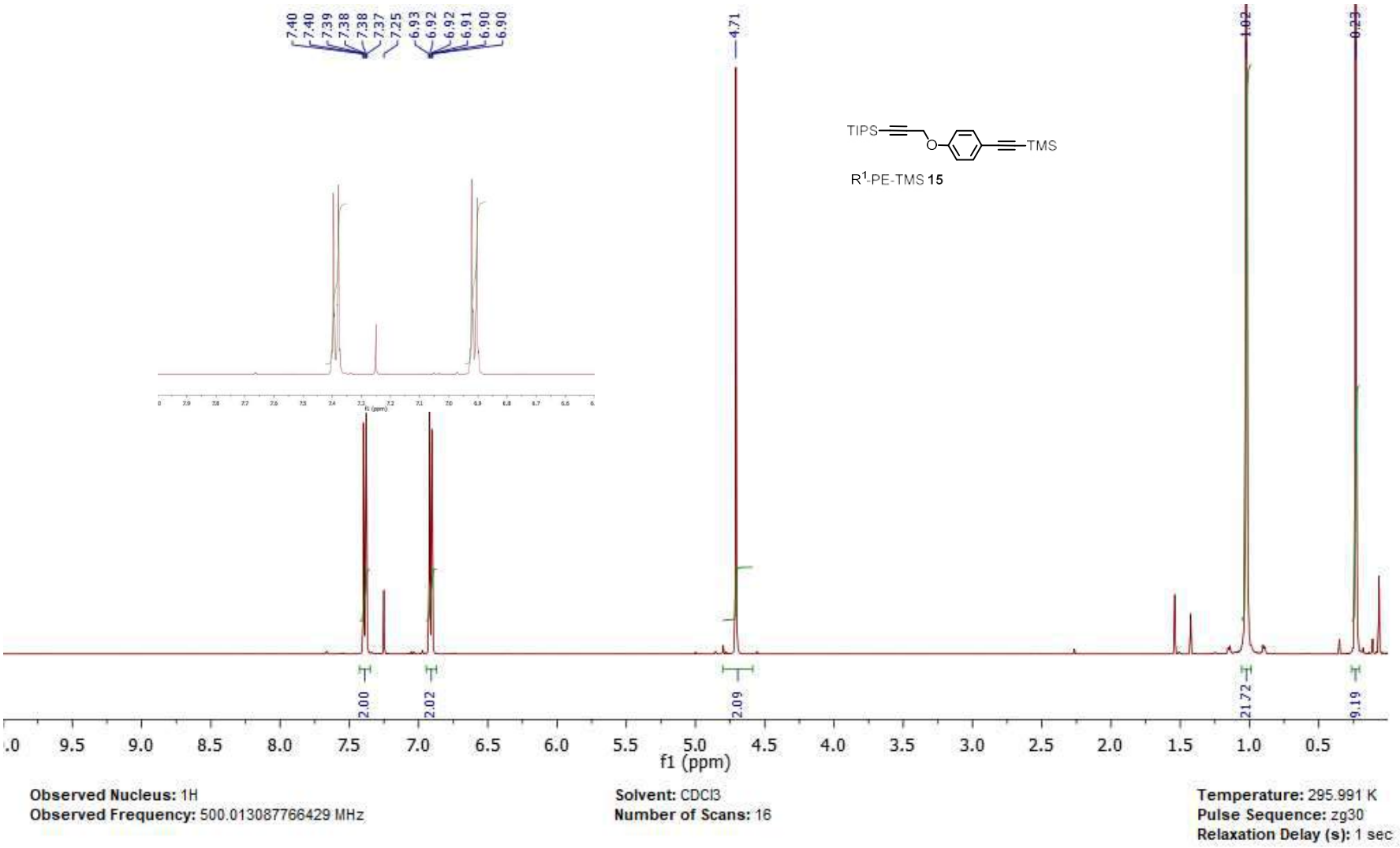

Figure Sb2b. ^{1}H NMR spectrum of R^{1}-PE-TMS **15** in $CDCl_3$.

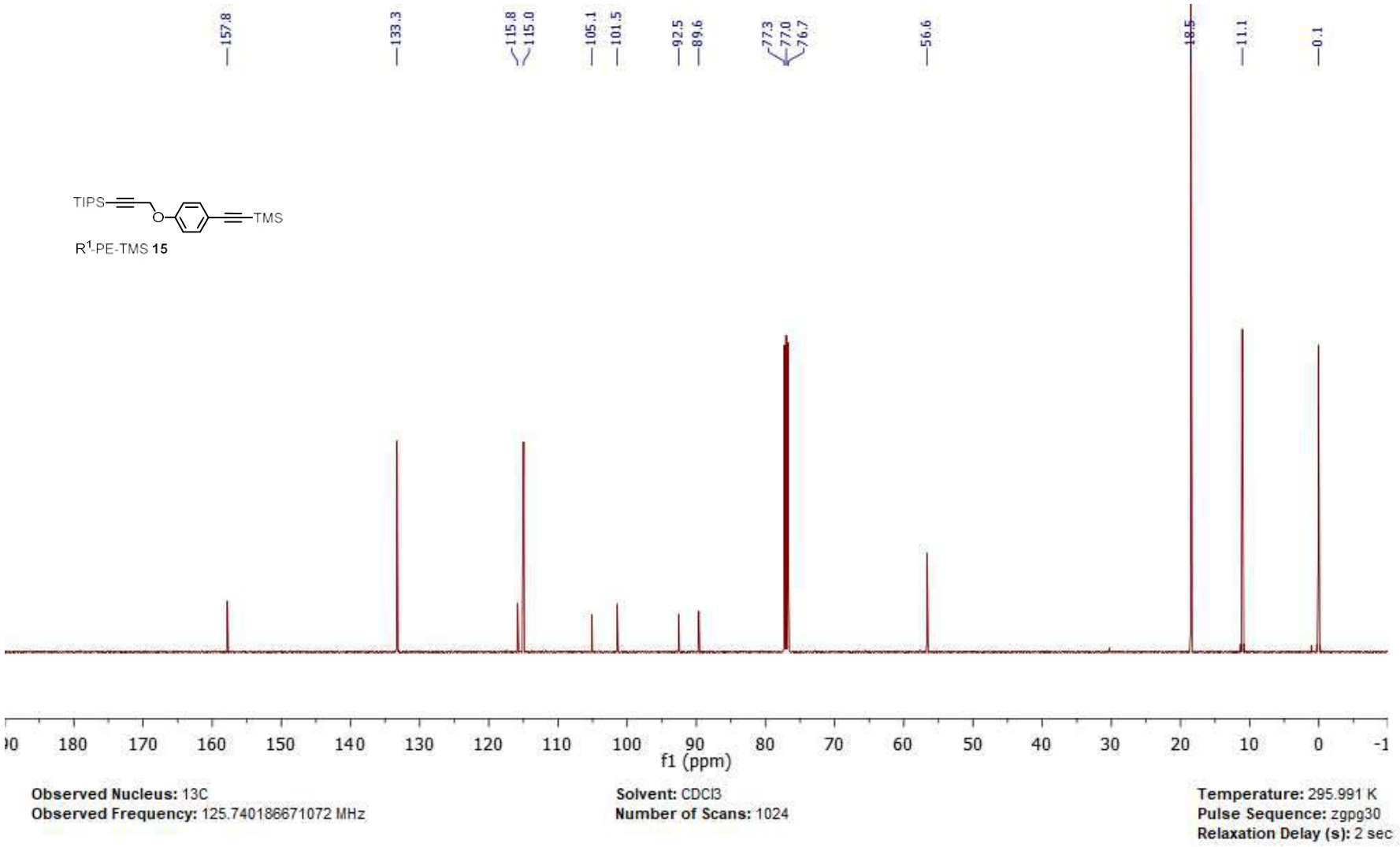

Figure Sb2c. ^{13}C NMR spectrum of R^1-PE-TMS **15** in $CDCl_3$.

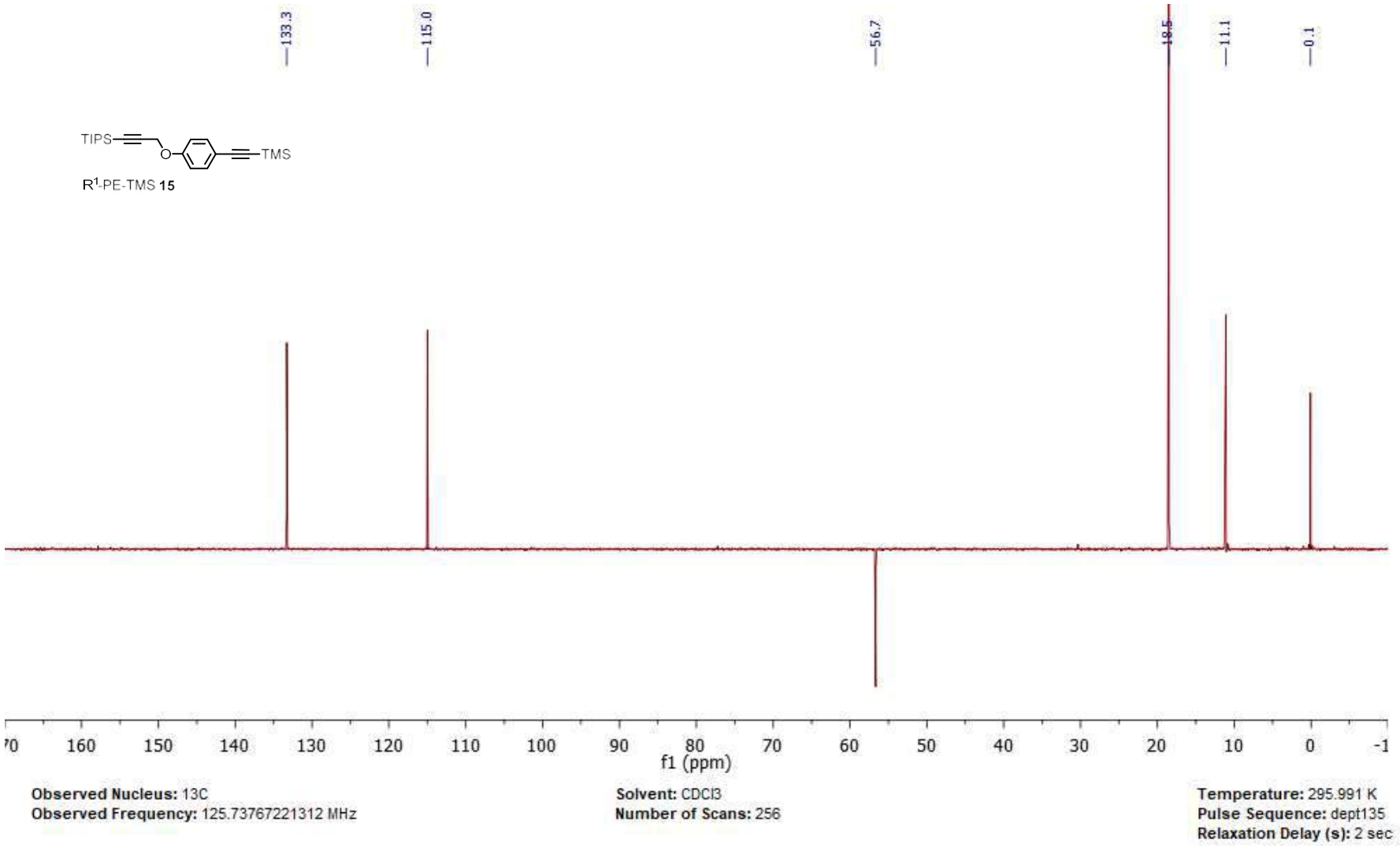

Figure Sb2d ^{13}C DEPT-135 NMR spectrum of R^1-PE-TMS **15** in $CDCl_3$.

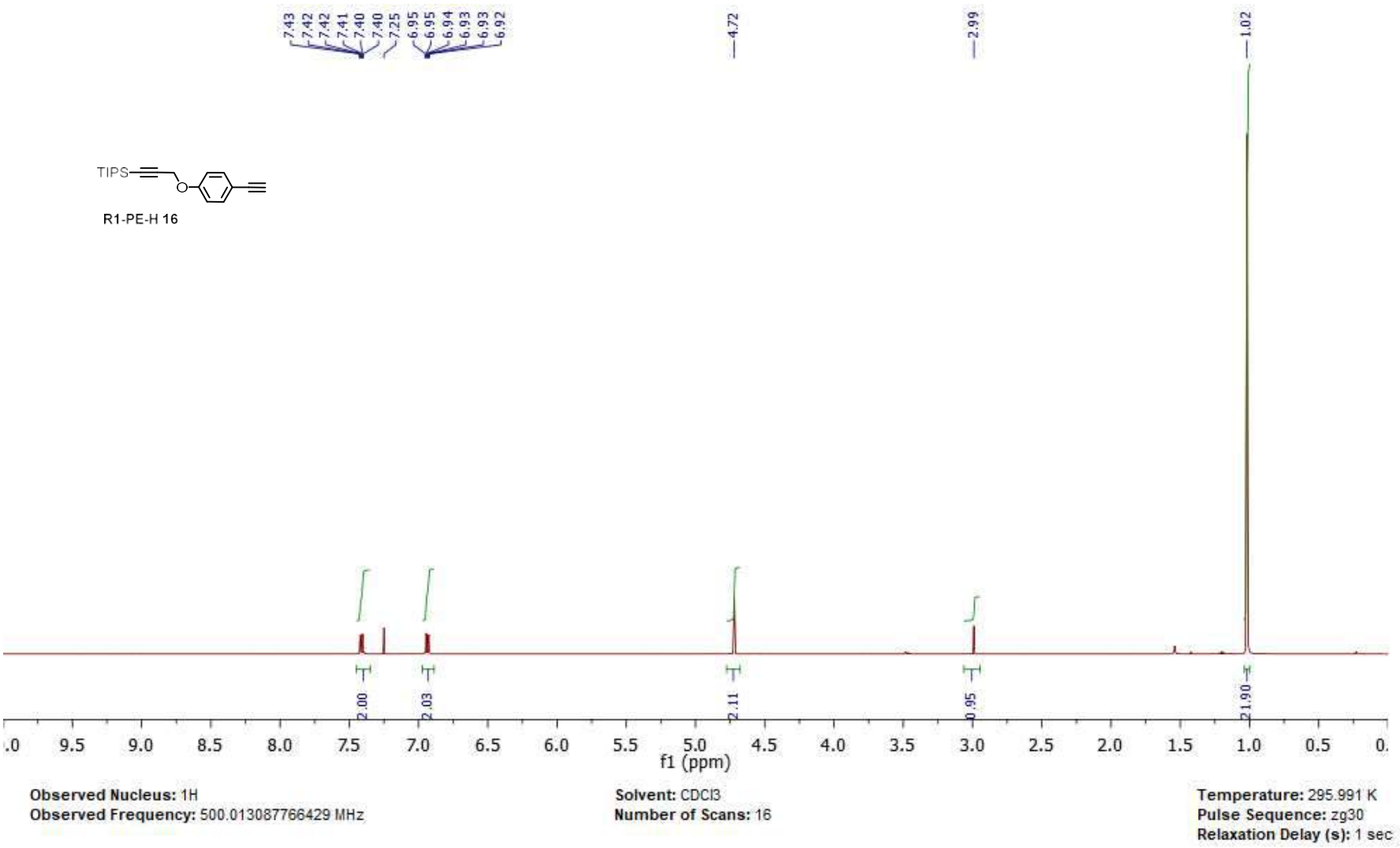

Figure Sb3a. ^{1}H NMR spectrum of R^{1}-PE-H **16** in $CDCl_3$.

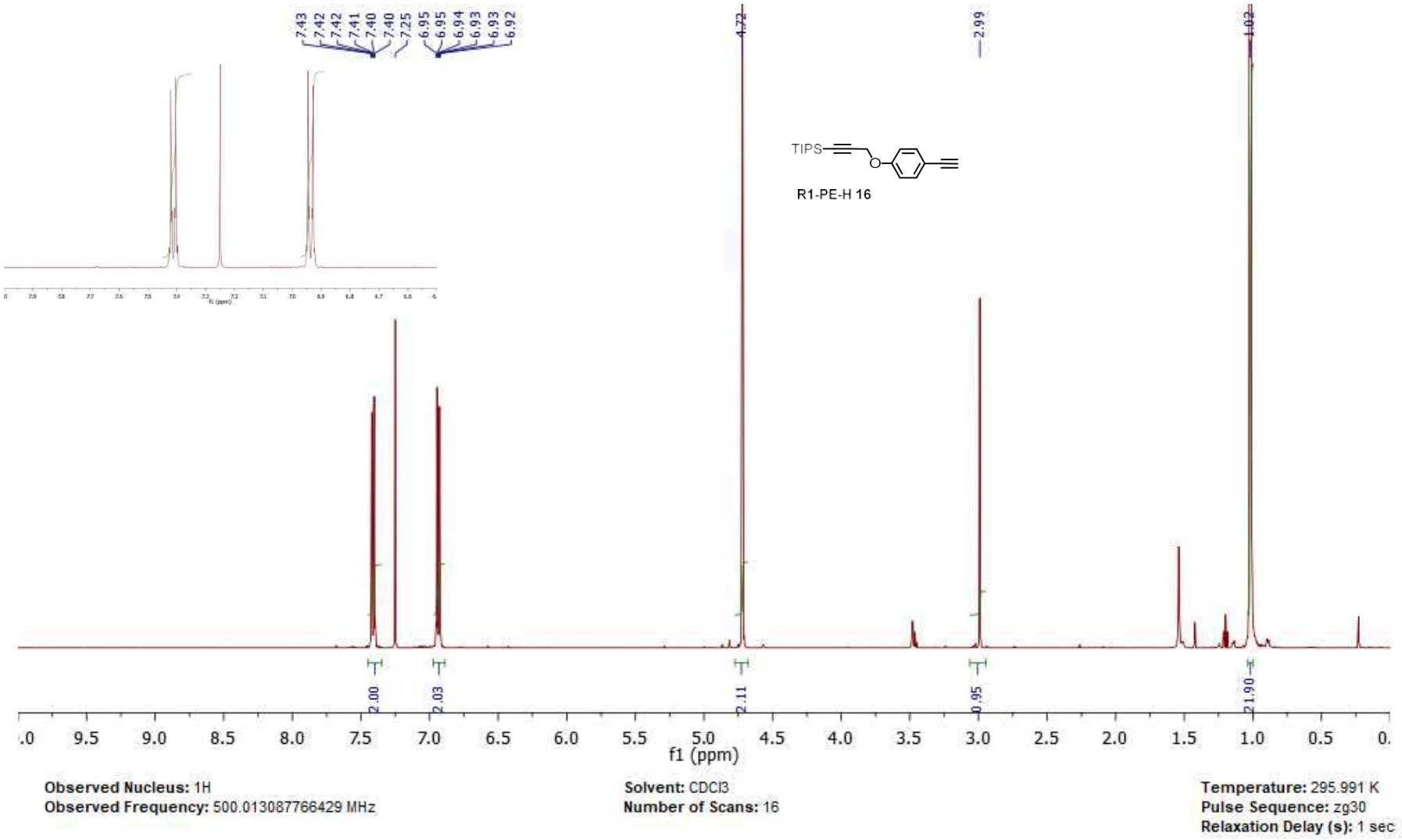

Figure Sb3b. ^{1}H NMR spectrum of R^{1}-PE-H **16** in $CDCl_3$.

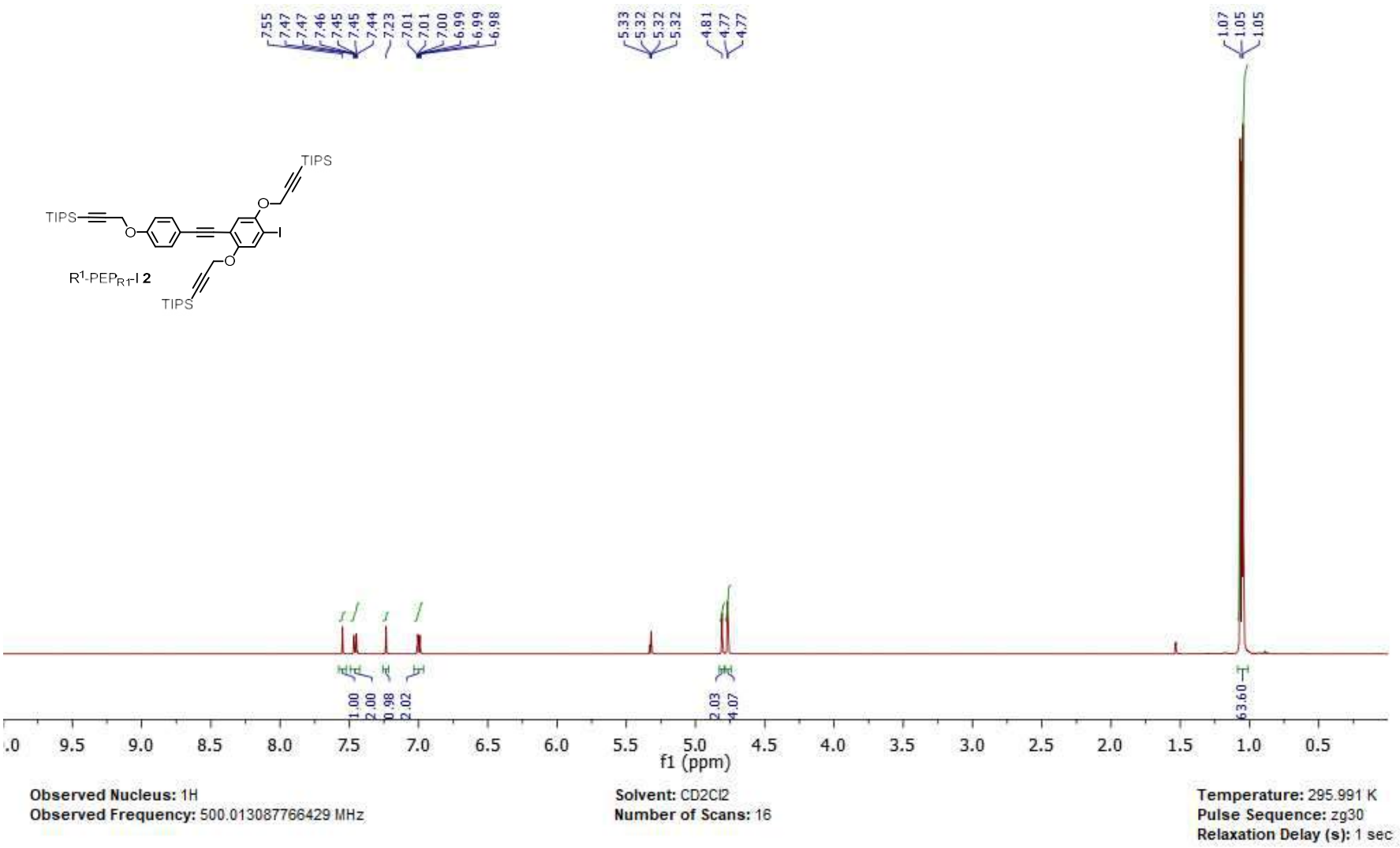

Figure Sb4a. ^{1}H NMR spectrum of R^{1}-PEP_{R1}-I **2** in CD_2Cl_2.

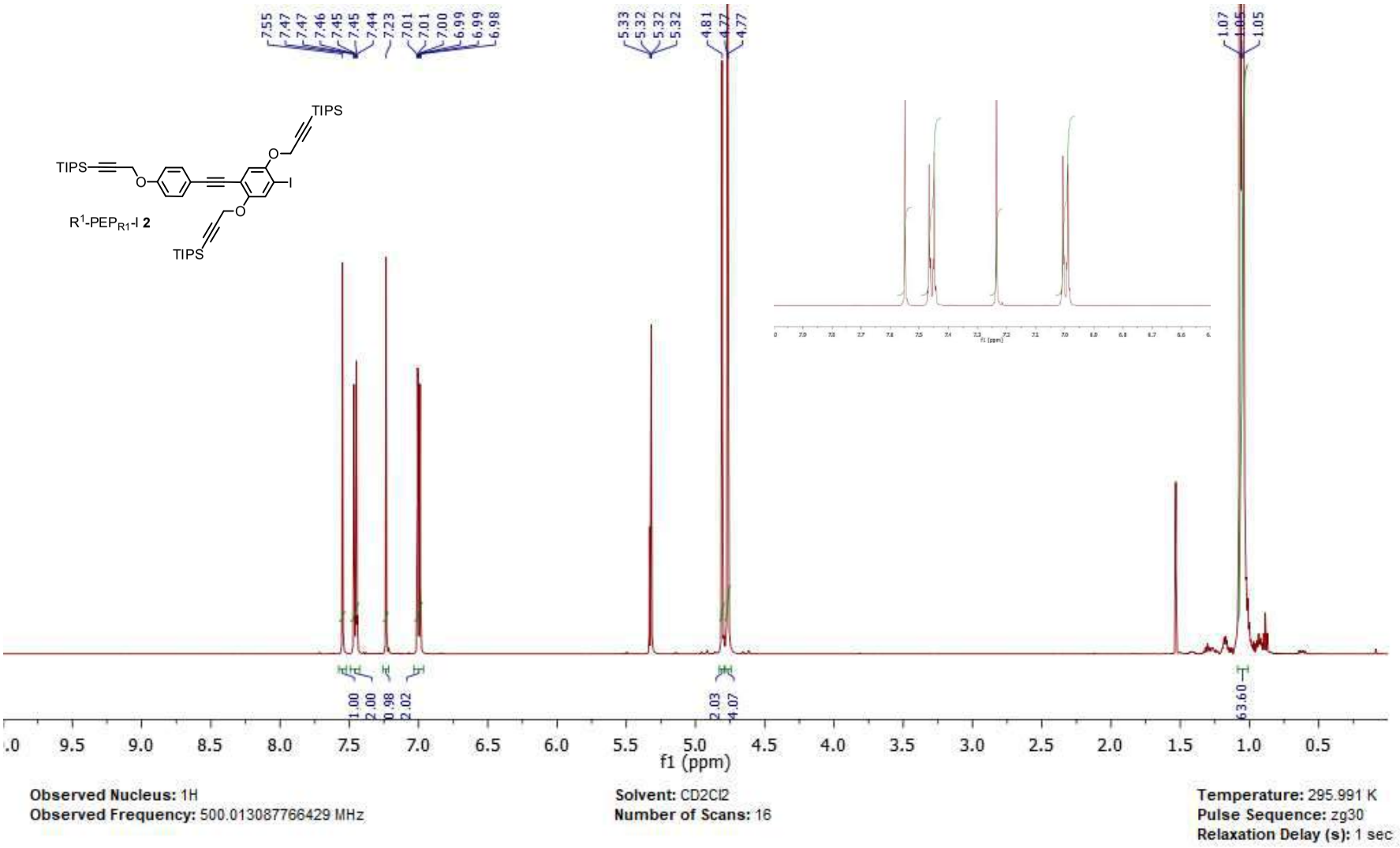

Figure Sb4b. ^{1}H NMR spectrum of R^{1}-PEP$_{R1}$-I **2** in CD_2Cl_2.

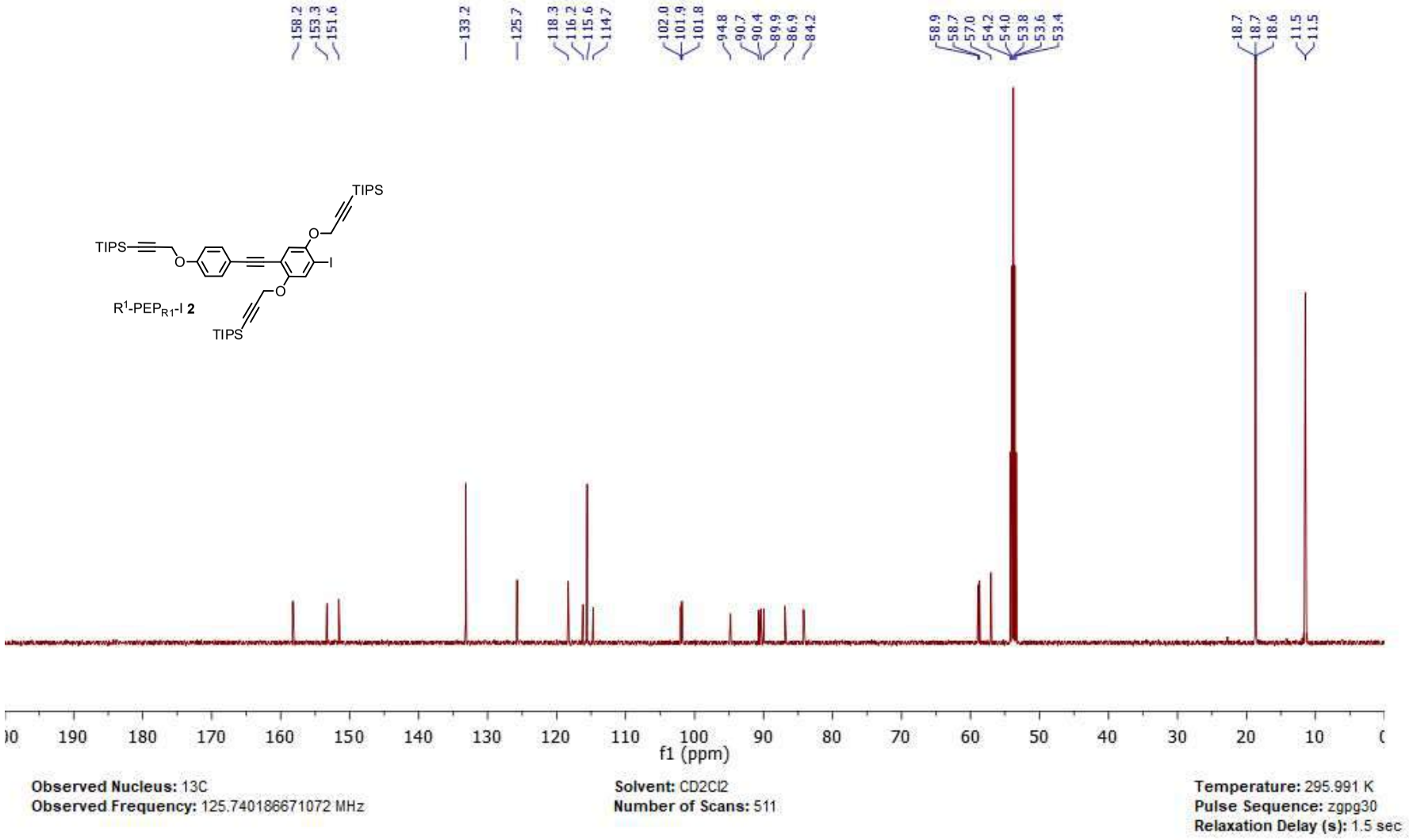

Figure Sb4c. ^{13}C NMR spectrum of R^1-PEP_{R1}-I **2** in CD_2Cl_2.

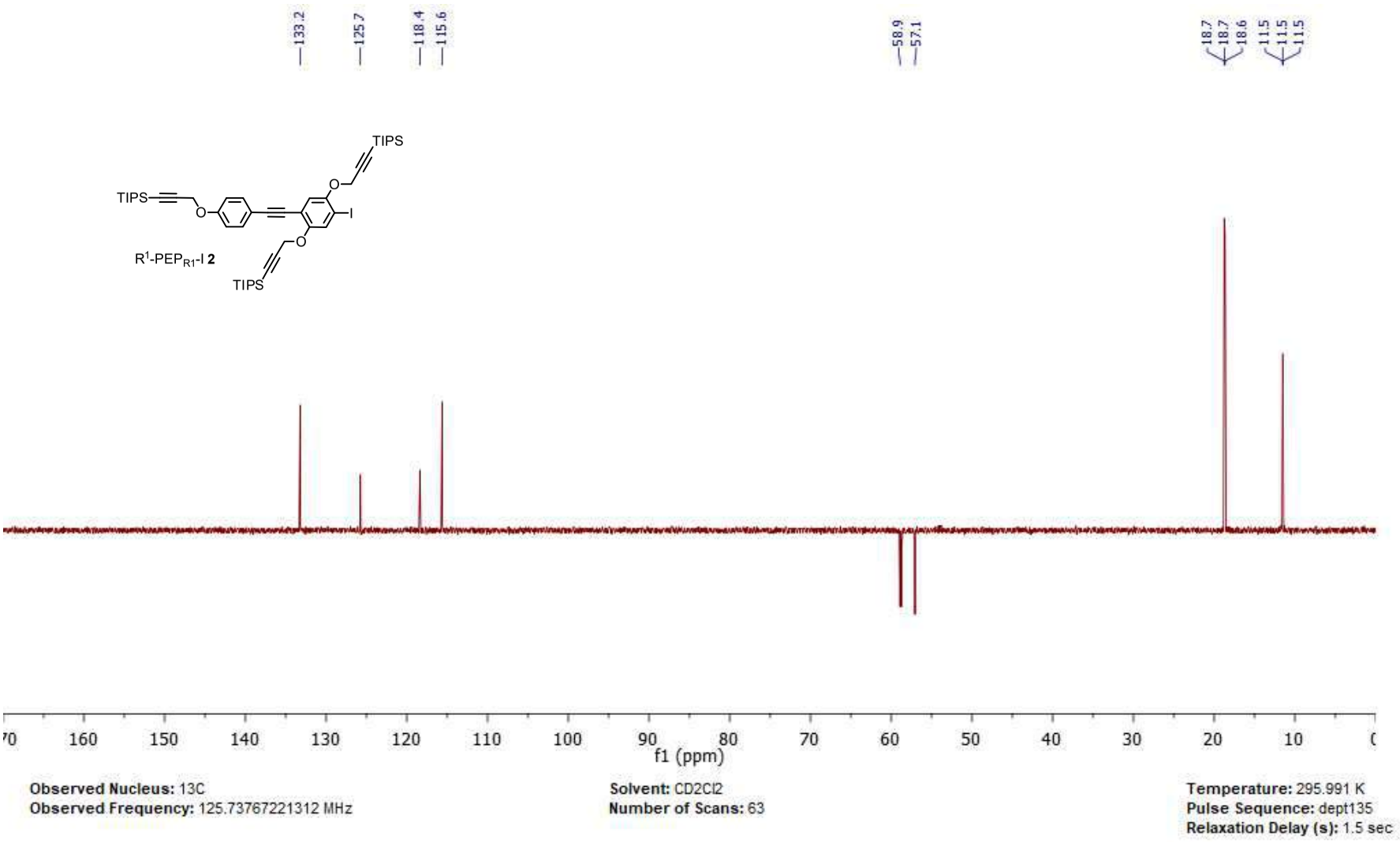

Figure Sb4d. ^{13}C DEPT-135 NMR spectrum of R^1-PEP_{R1}-I **2** in CD_2Cl_2.

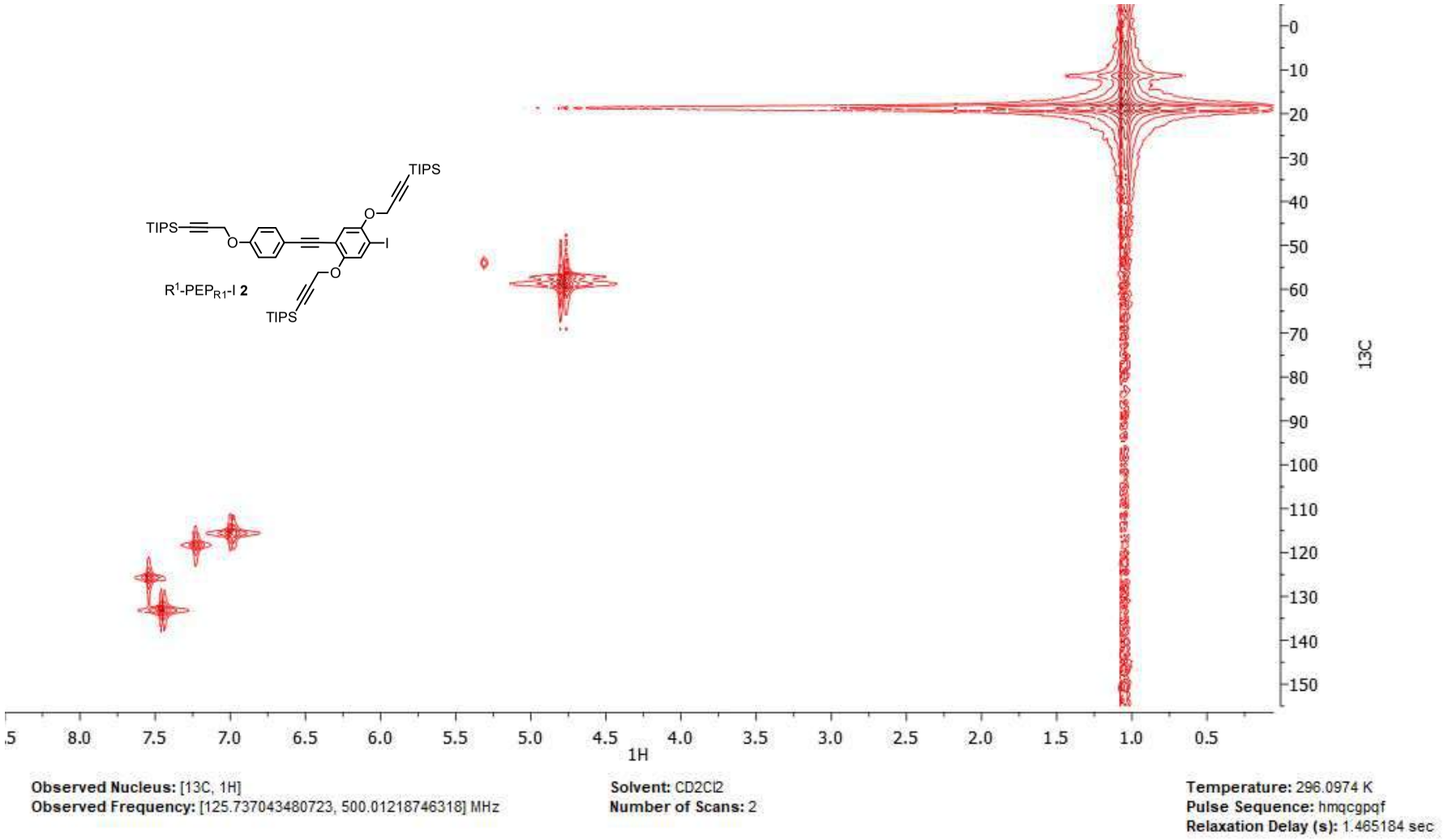

Figure Sb4e. HMQC NMR spectrum of R^1-PEP_{R1}-I **2** in CD_2Cl_2.

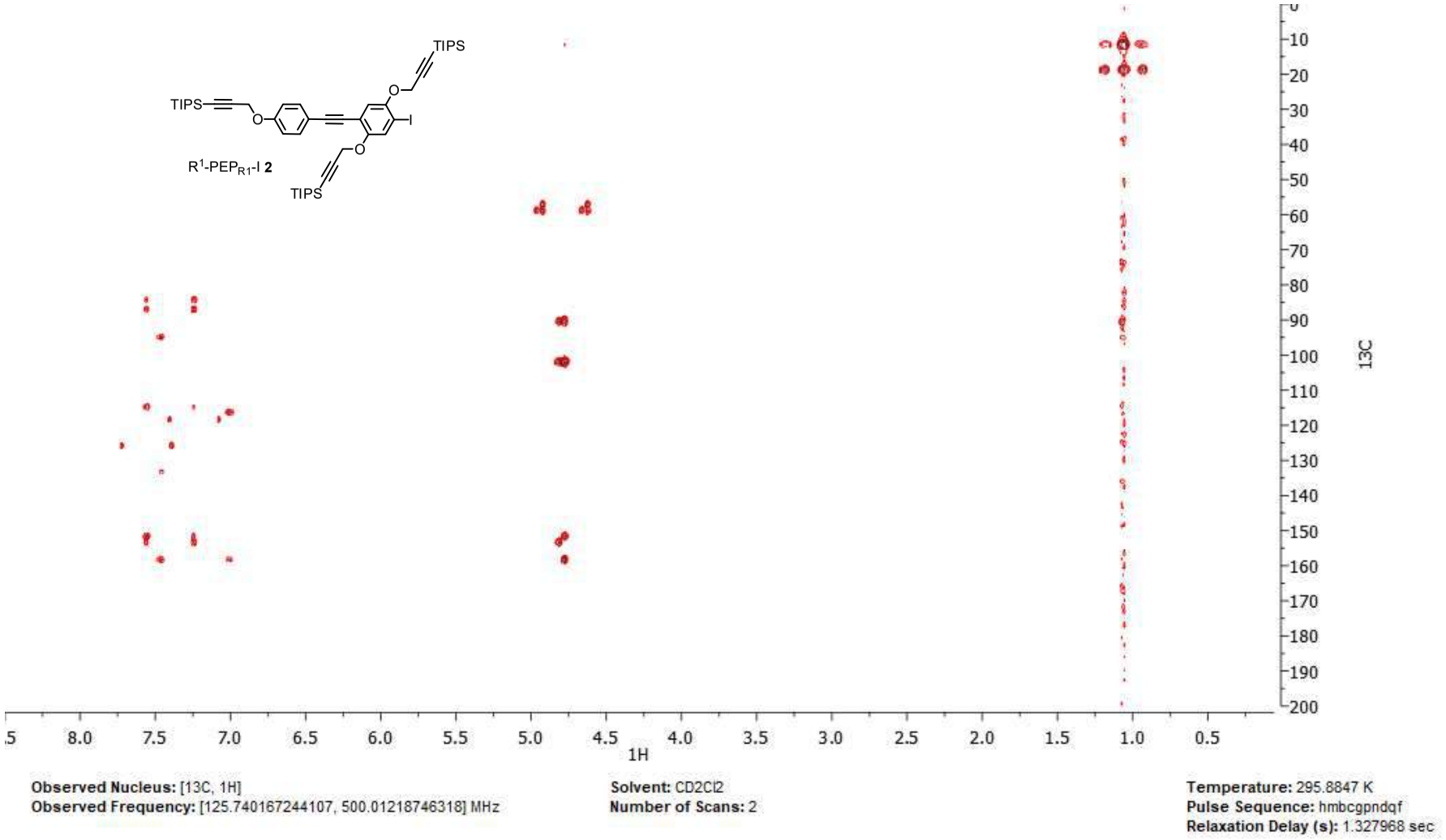

Figure Sb4f. HMBC NMR spectrum of R^1-PEP_{R1}-I **2** in CD_2Cl_2.

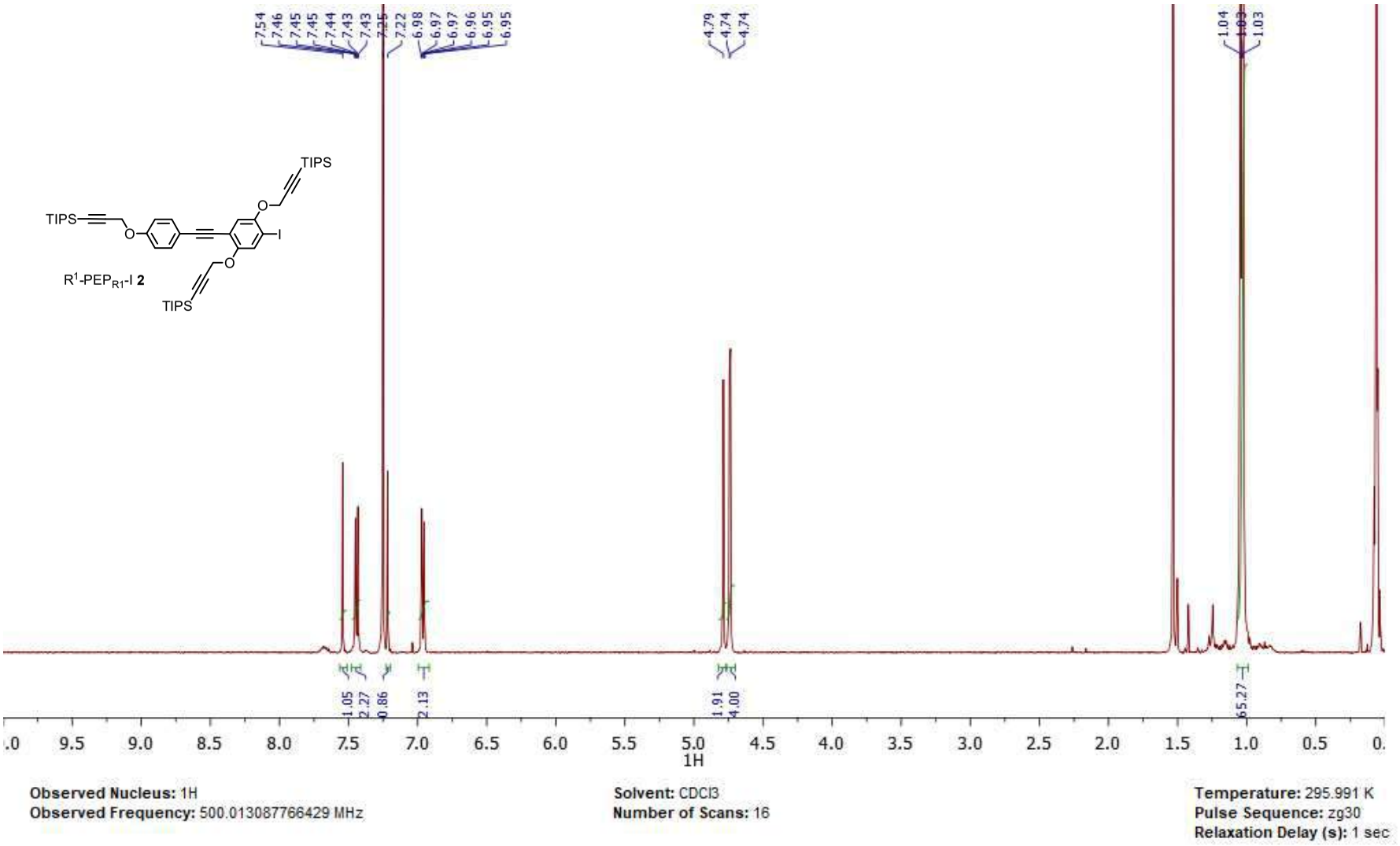

Figure Sb4g. ^{1}H NMR spectrum of R^1-PEP_{R1}-I **2** in $CDCl_3$. The material giving this spectrum was used together with pure R^1-PEP_{R1}-I **2** (1:1 ratio) for the synthesis of R^1-$PEP_{R1}P$-NH_2 **8**.

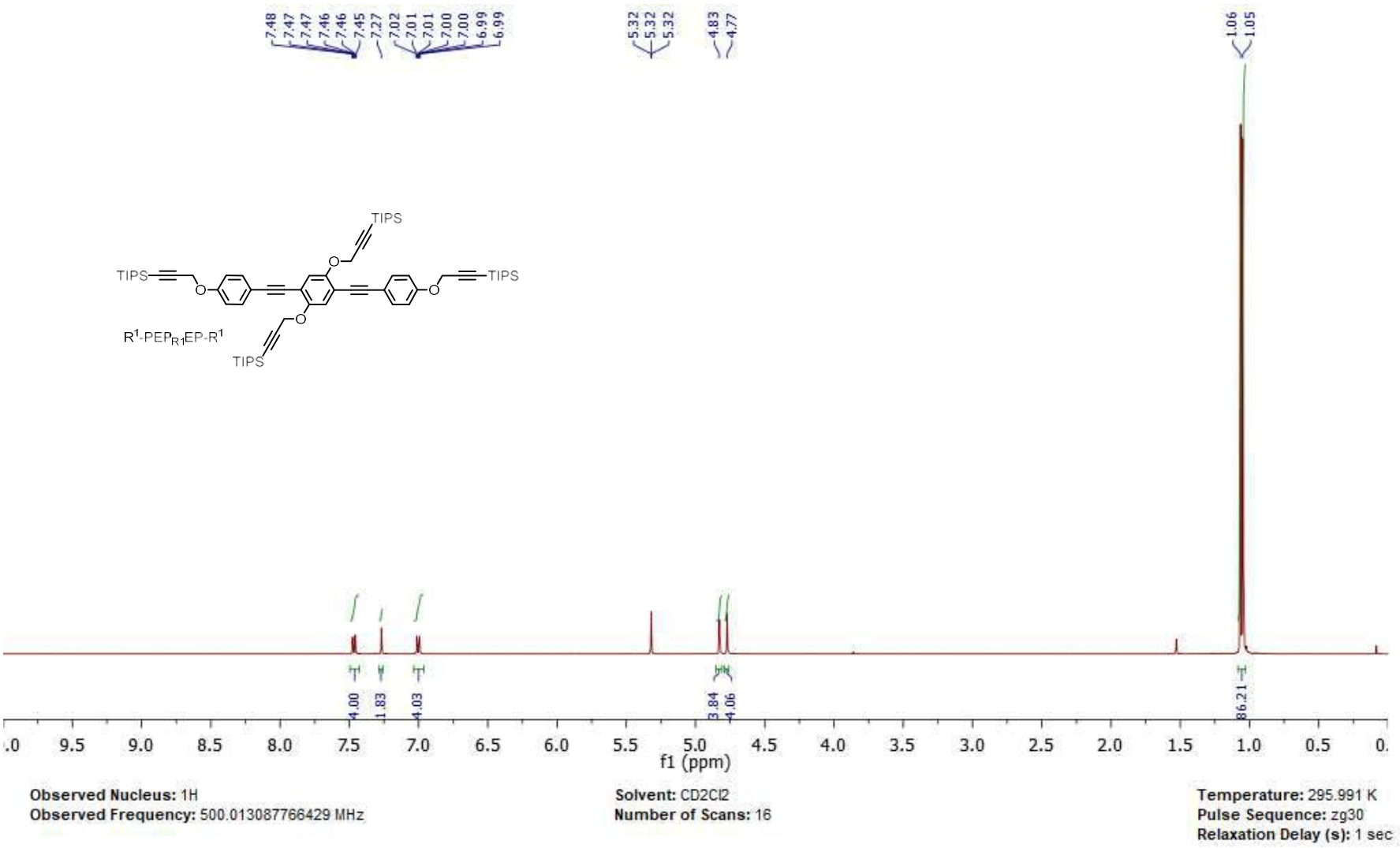

Figure Sb5a. ^{1}H NMR spectrum of R^1-$PEP_{R1}EP$-R^1 in CD_2Cl_2.

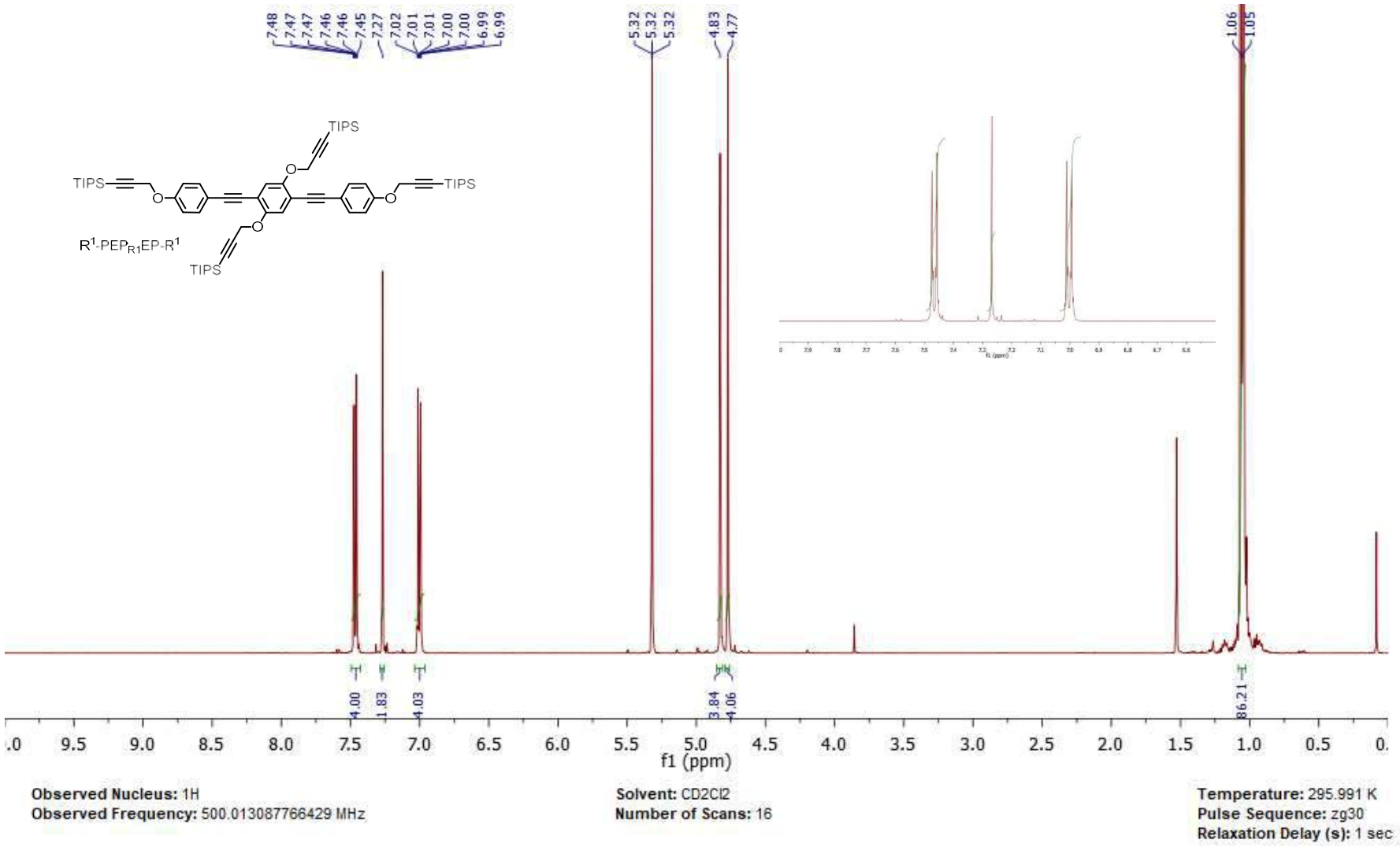

Figure Sb5b. ^{1}H NMR spectrum of R^1-$PEP_{R1}EP$-R^1 in CD_2Cl_2.

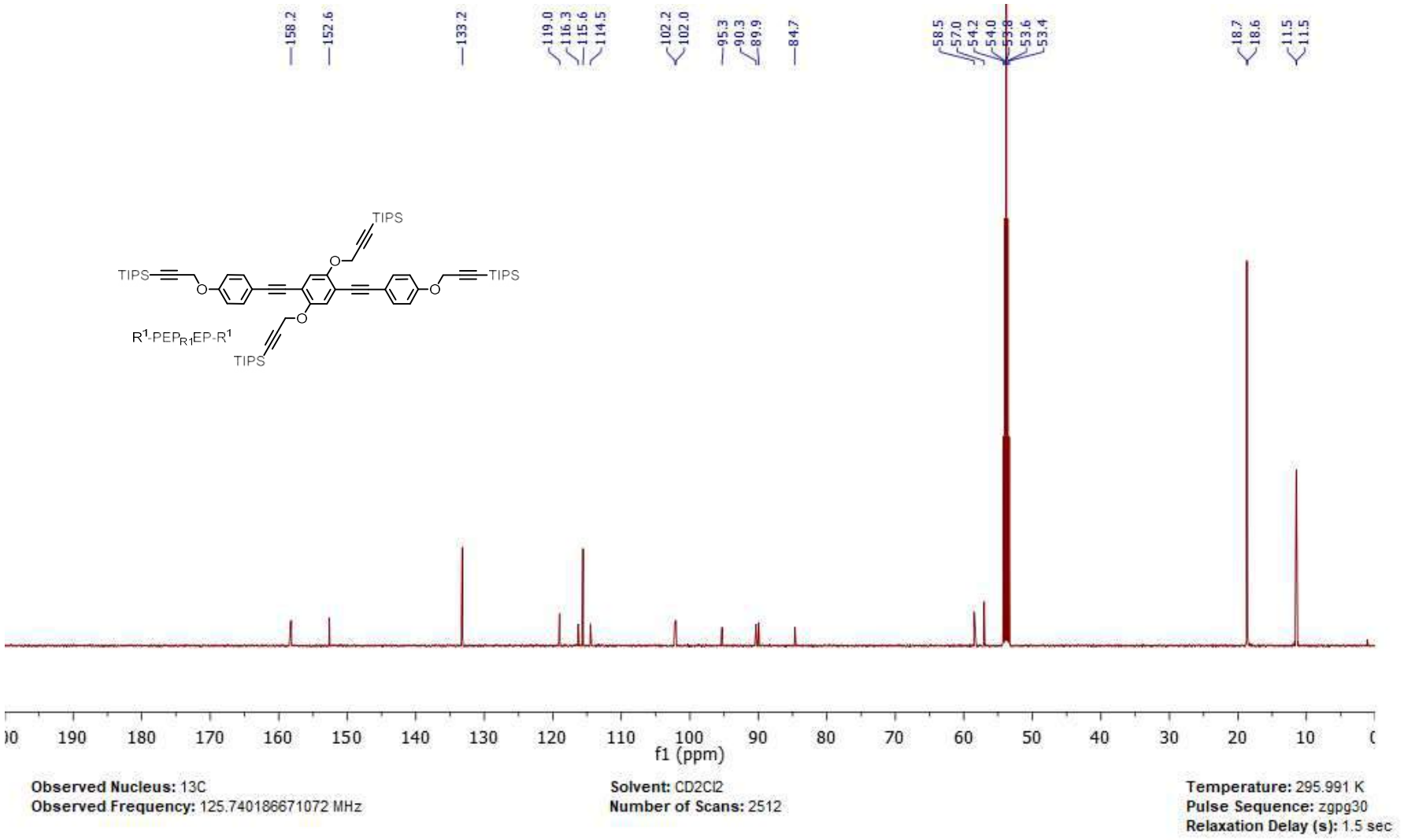

Figure Sb5c. ^{13}C NMR spectrum of R^1-$PEP_{R1}EP$-R^1 in CD_2Cl_2.

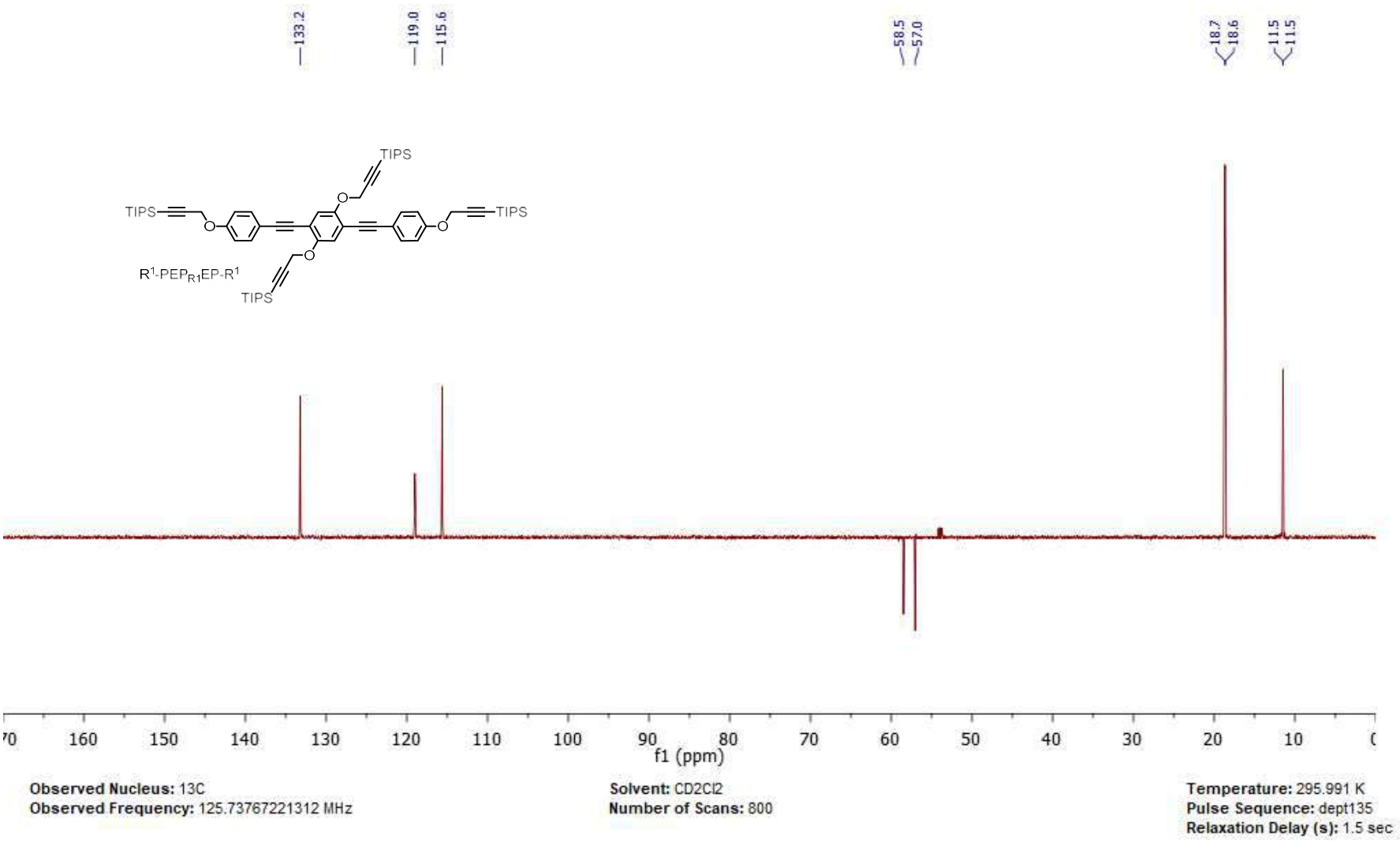

Figure Sb5d. ^{13}C DEPT-135 NMR spectrum of R^1-$PEP_{R1}EP$-R^1 in CD_2Cl_2.

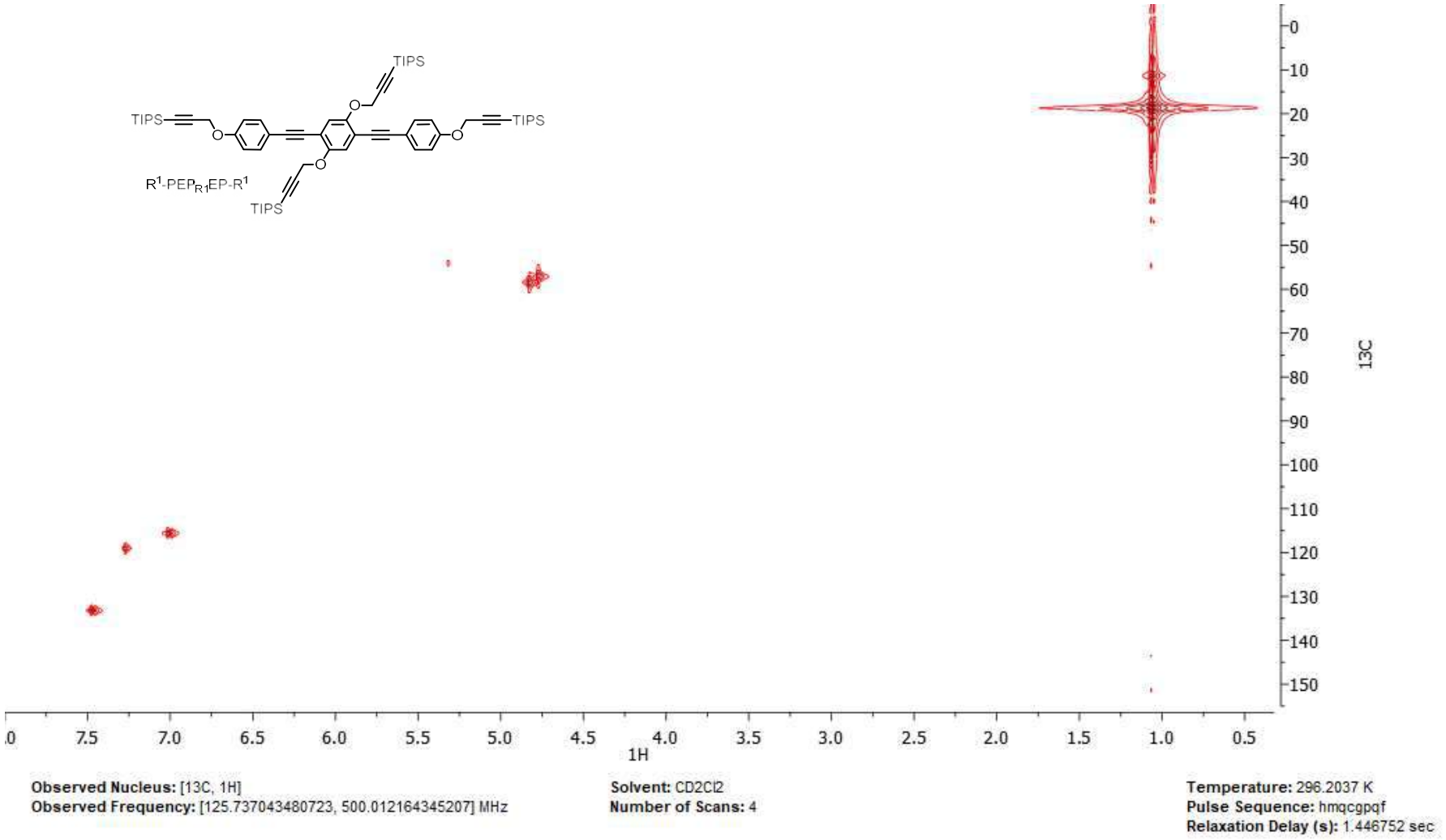

Figure Sb5e. HMQC NMR spectrum of R^1-$PEP_{R1}EP$-R^1 in CD_2Cl_2.

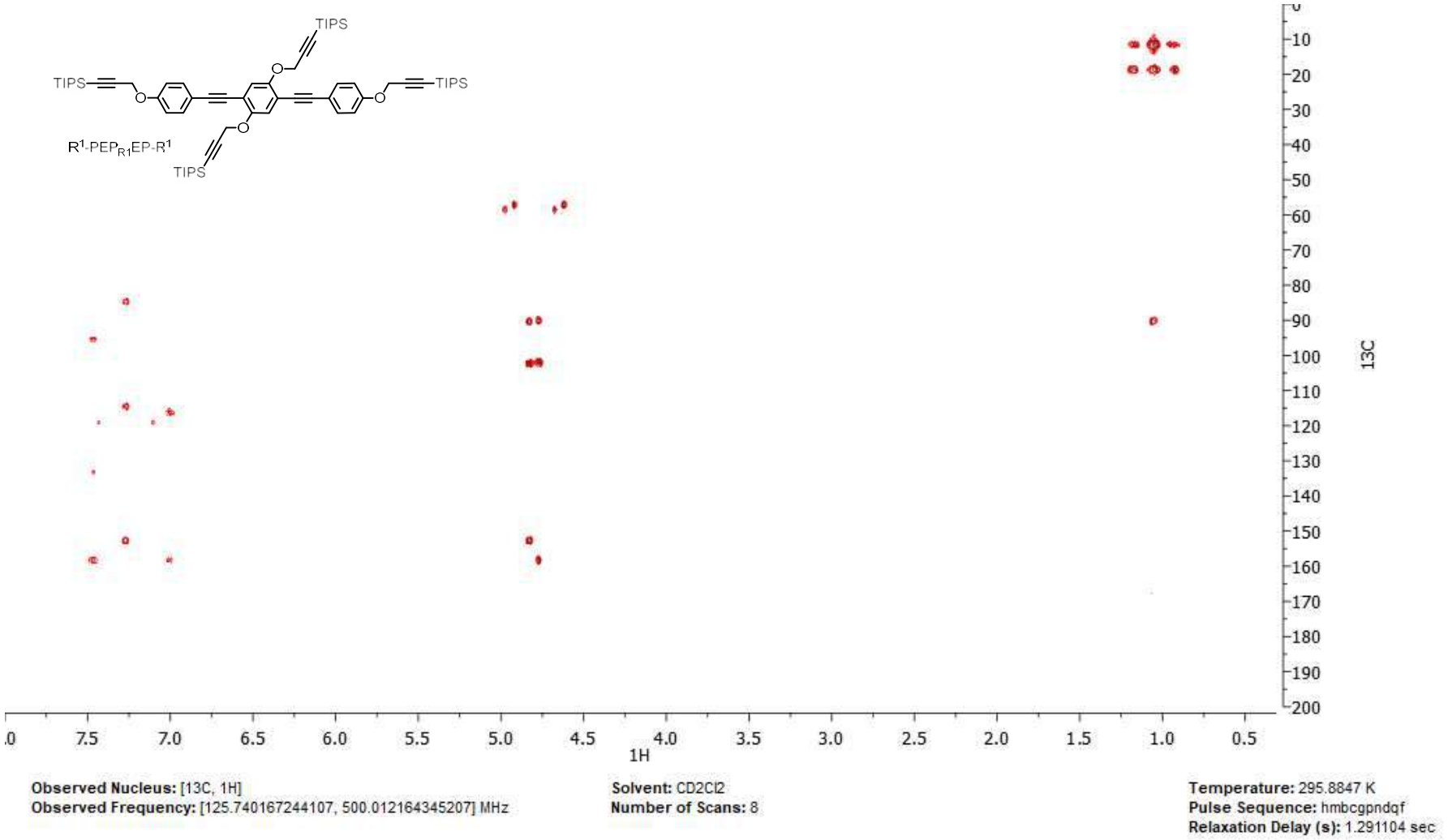

Figure Sb5f. HMBC NMR spectrum of R^1-$PEP_{R1}EP$-R^1 in CD_2Cl_2.

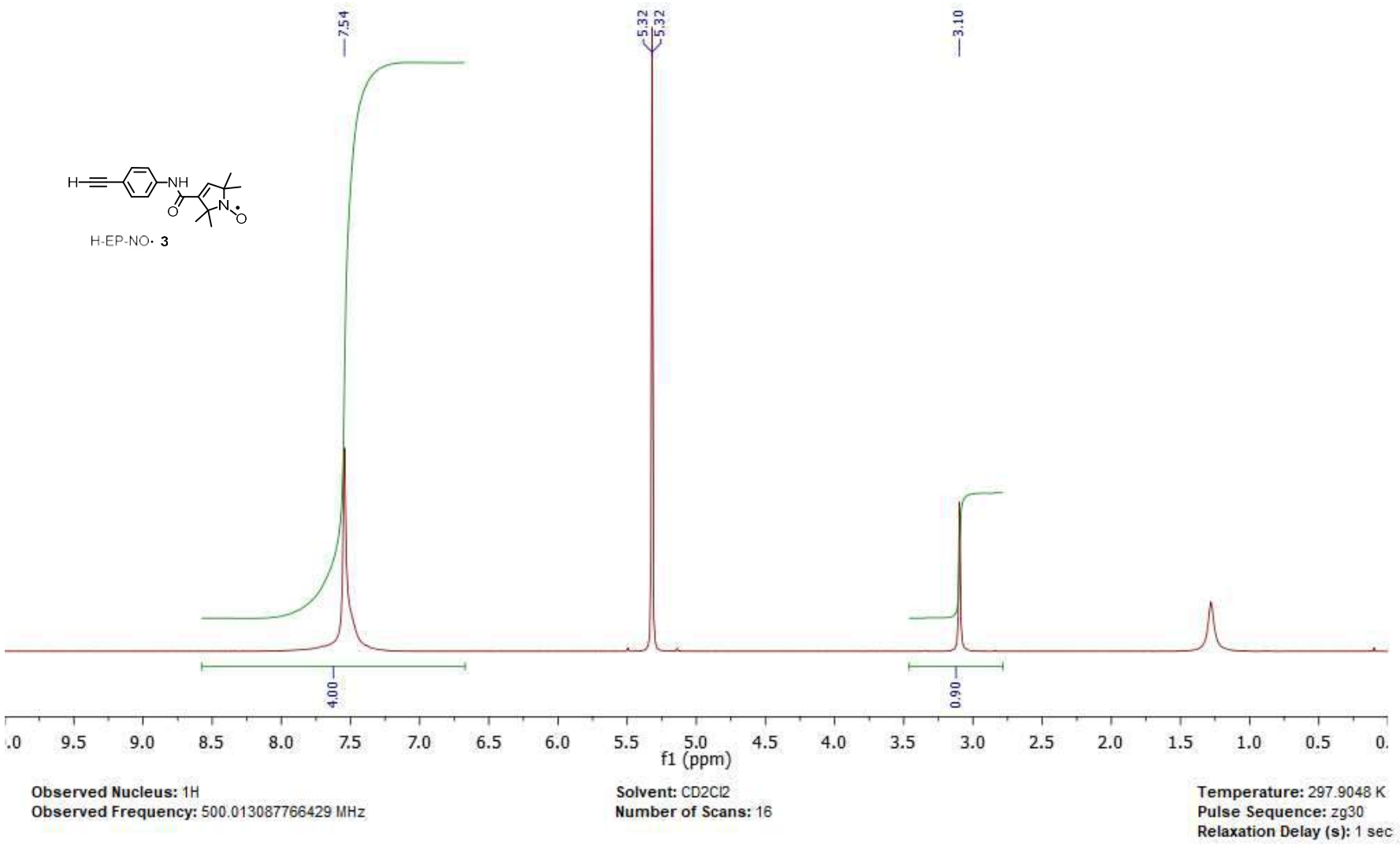

Figure Sb6a. ^{1}H NMR spectrum of H-EP-NO• **3** in CD_2Cl_2.

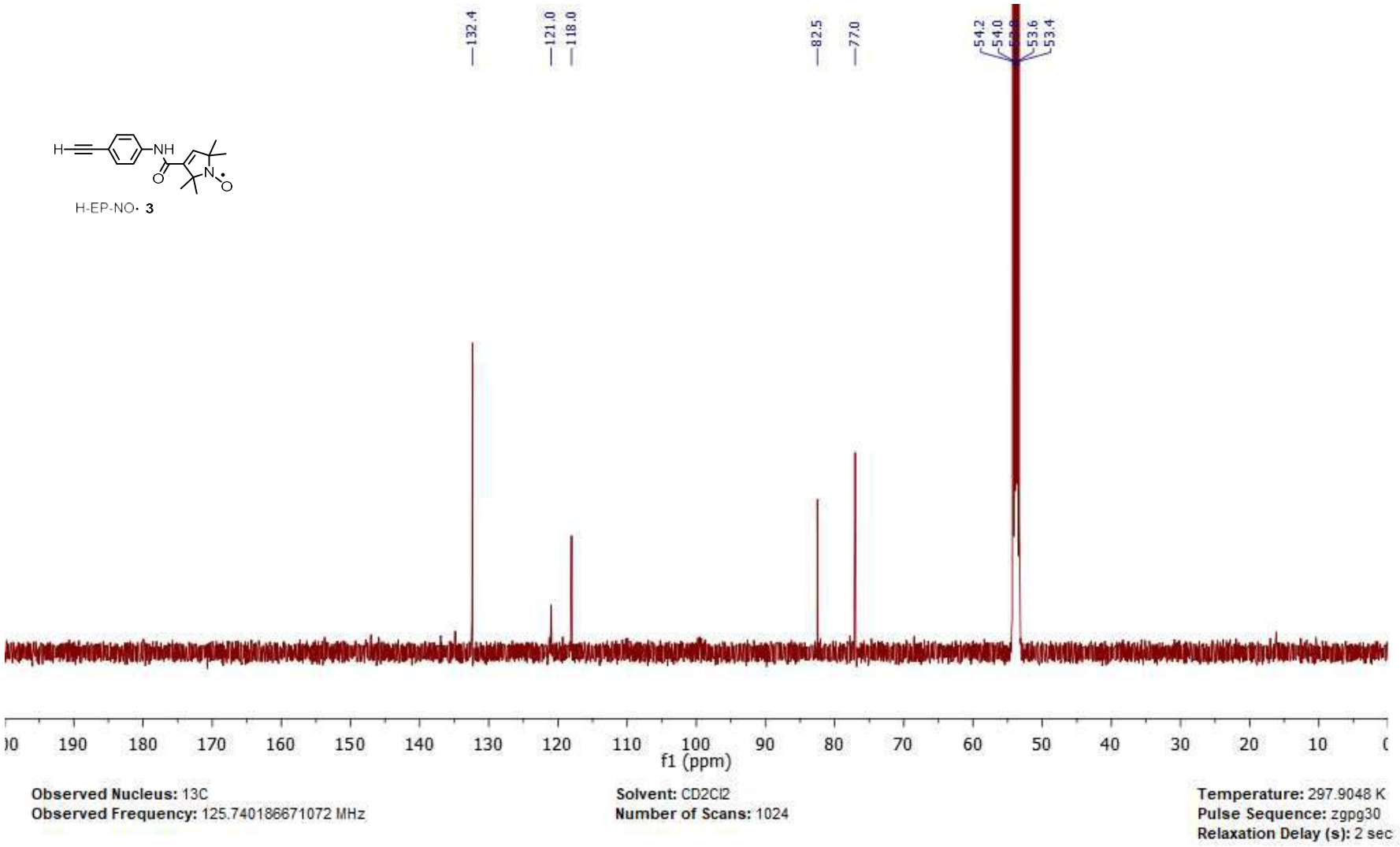

Figure Sb6b. ^{13}C NMR spectrum of H-EP-NO• **3** in CD_2Cl_2.

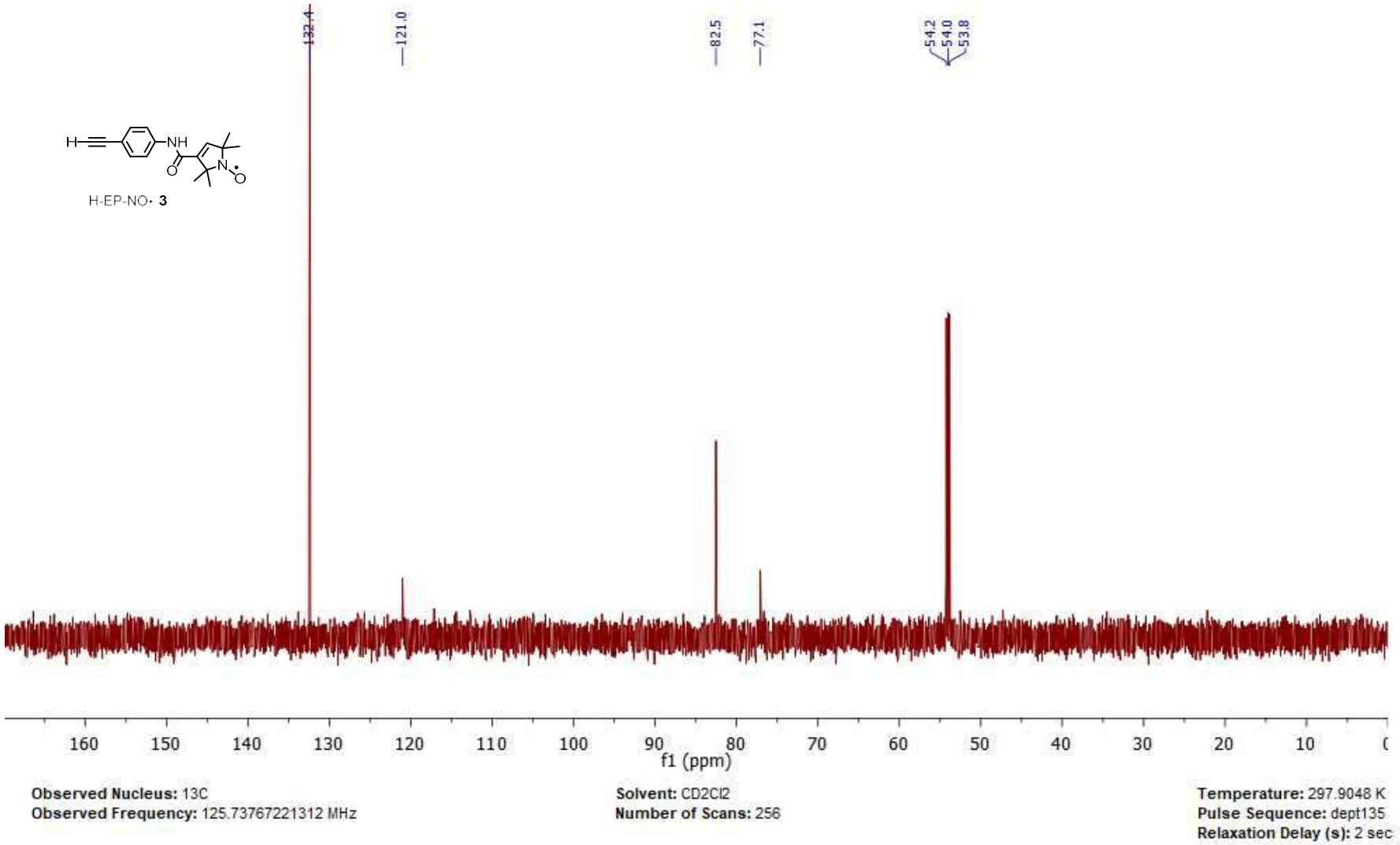

Figure Sb6c. ^{13}C DEPT-135 NMR spectrum of H-EP-NO• **3** in CD_2Cl_2.

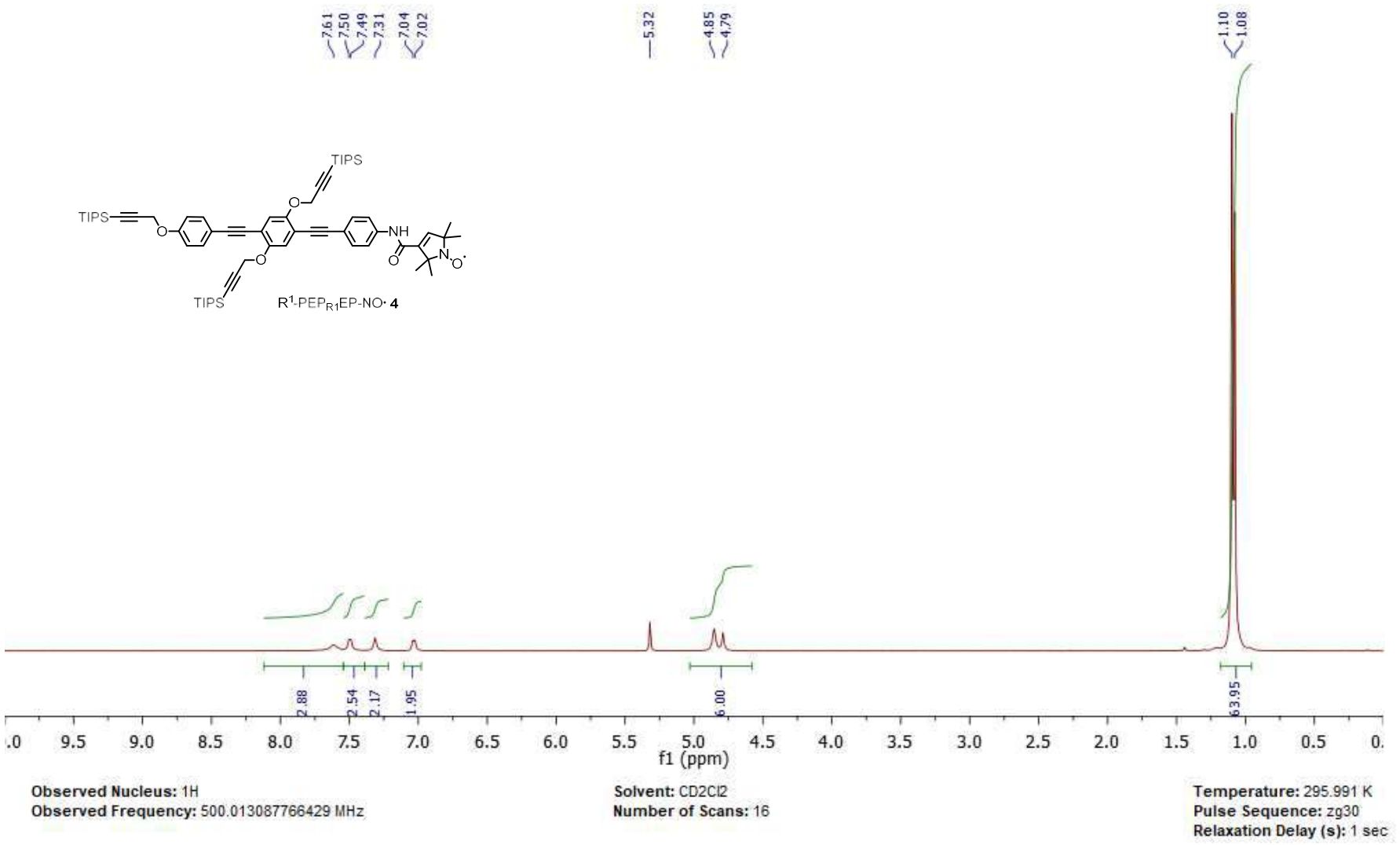

Figure Sb7a. ^{1}H NMR spectrum of R^{1}-PEP$_{R1}$EP-NO• **4** in CD_2Cl_2.

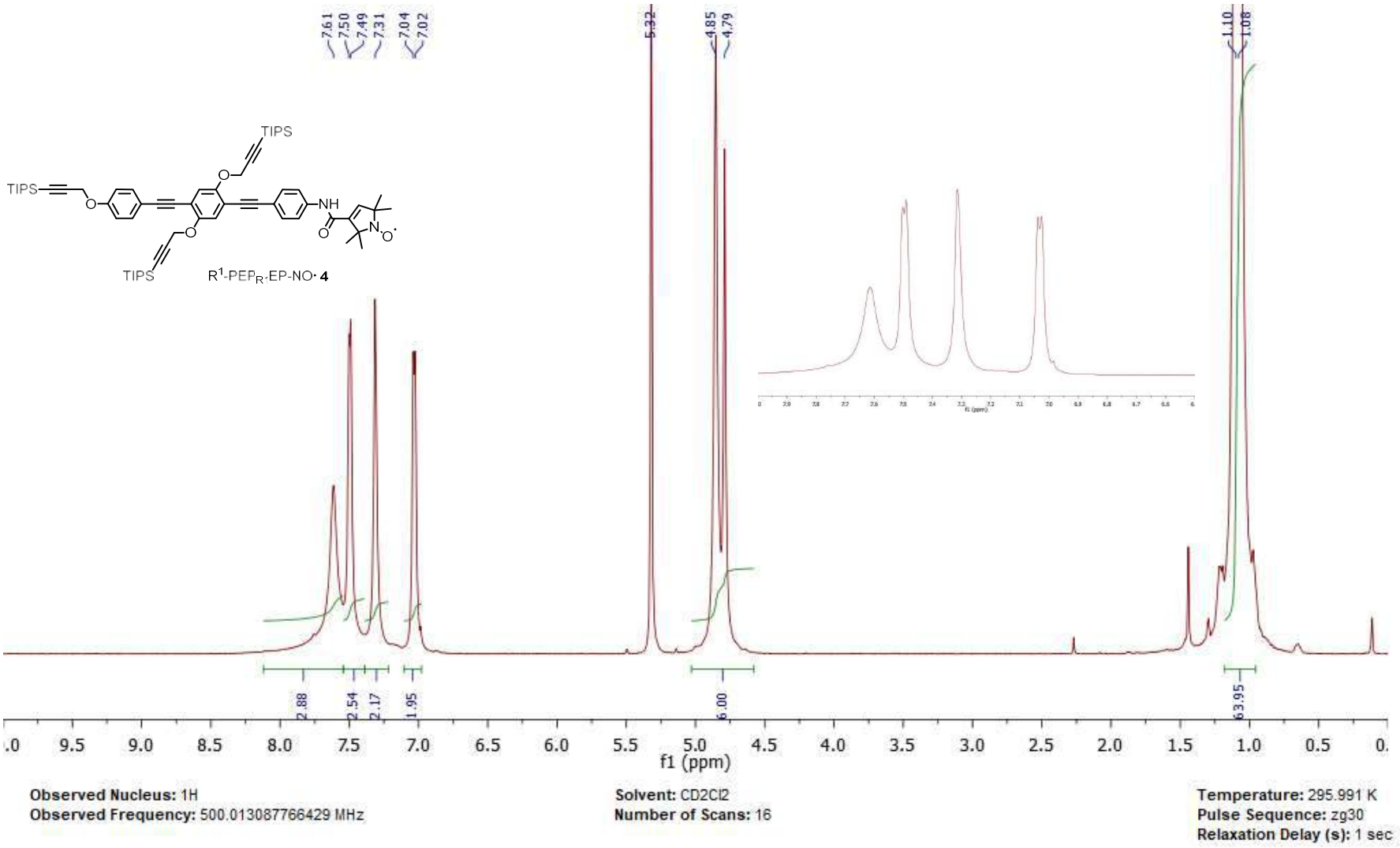

Figure Sb7b. ^{1}H NMR spectrum of R^{1}-PEP$_{R1}$EP-NO• **4** in CD_2Cl_2.

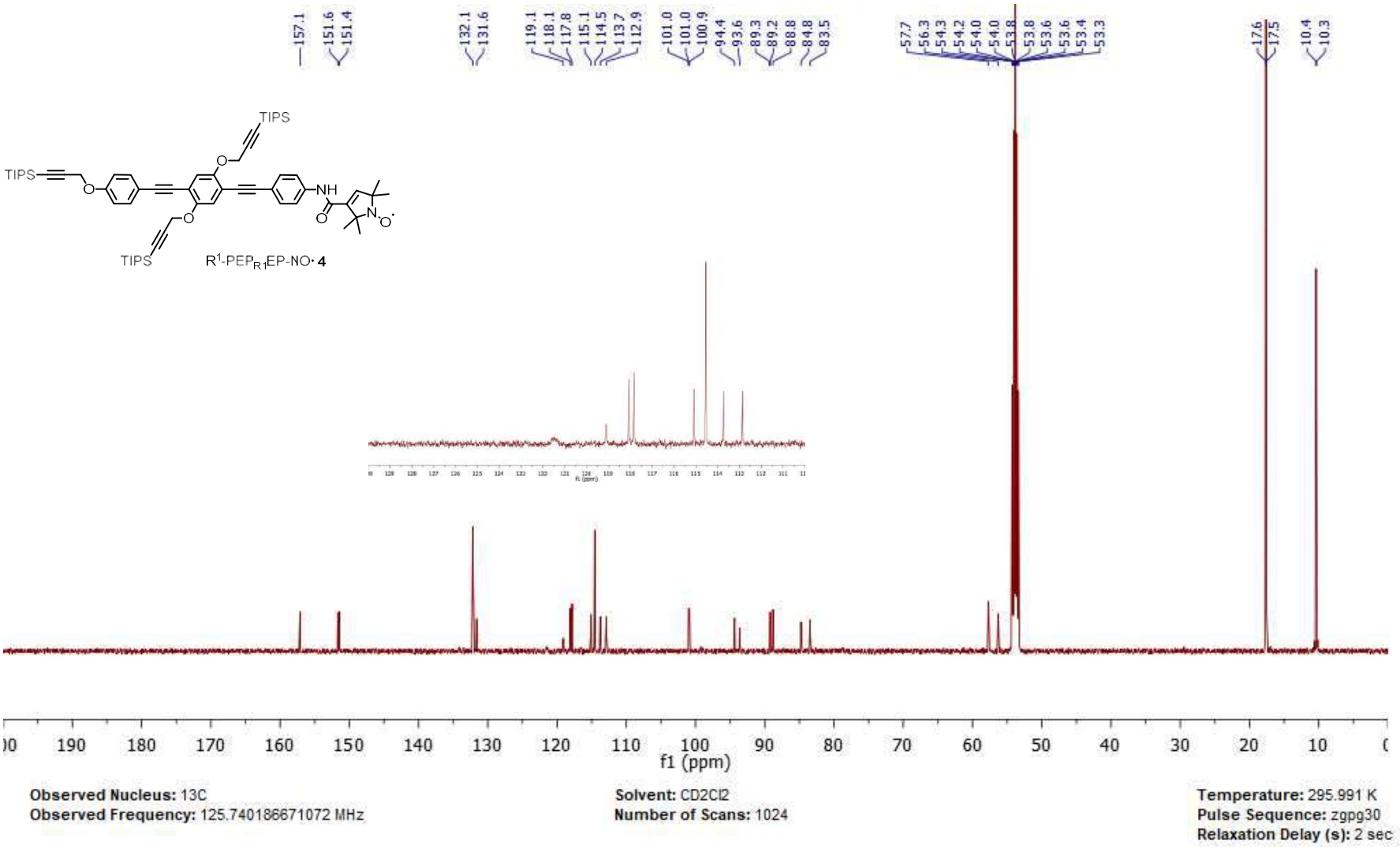

Figure Sb7c. ^{13}C NMR spectrum of R^1-$PEP_{R1}EP$-NO• **4** in CD_2Cl_2.

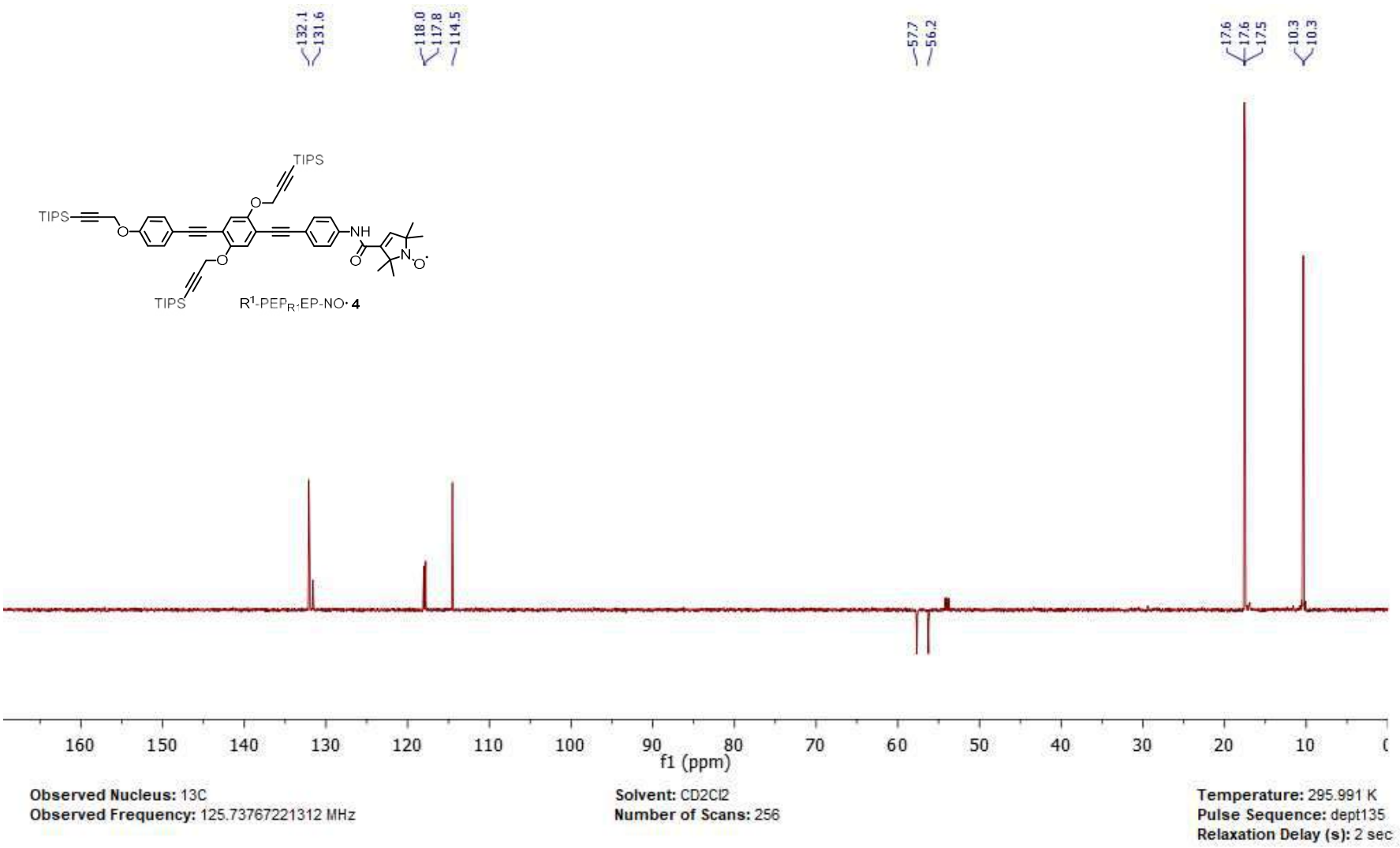

Figure Sb7d. ^{13}C DEPT-135 NMR spectrum of R^1-PEP_{R1}EP-NO• **4** in CD_2Cl_2.

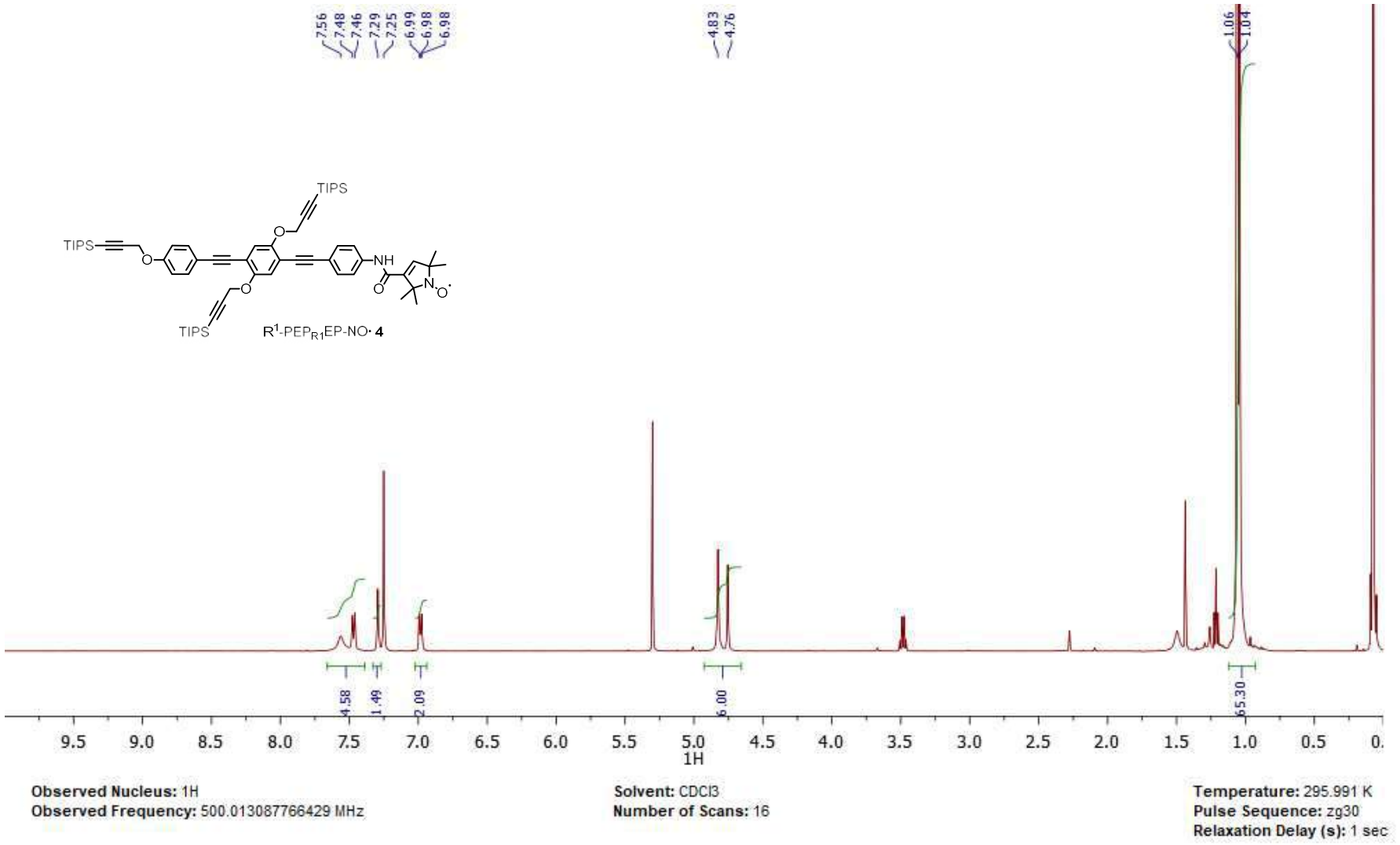

Figure Sb7e. ^{1}H NMR spectrum of R^{1}-PEP$_{R1}$EP-NO• **4** in $CDCl_3$. This material was used to obtain the reported accurate mass spectroscopical data.

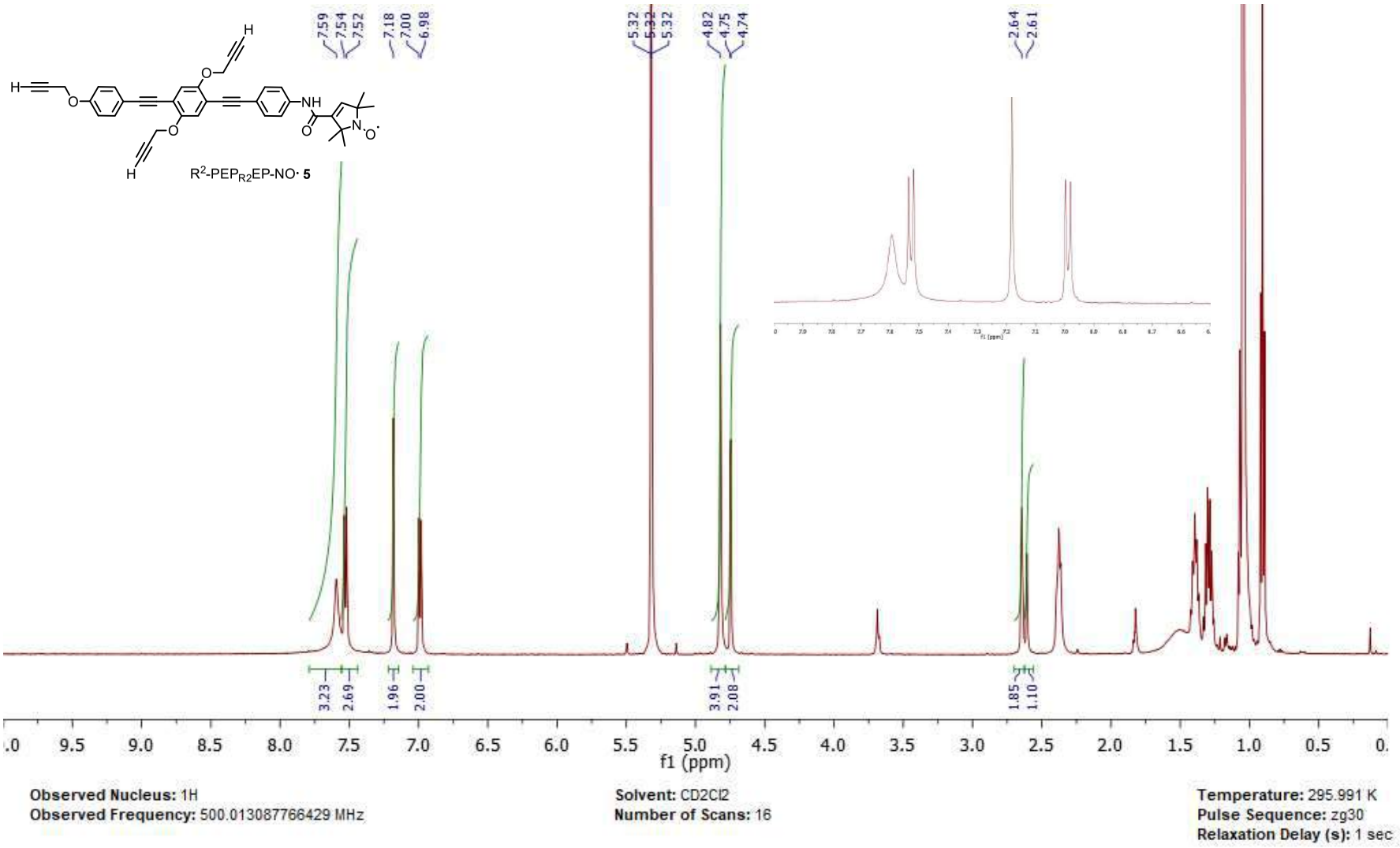

Figure Sb8. ^{1}H NMR spectrum of R^2-$PEP_{R2}EP$-NO• in CD_2Cl_2 **5** (containing THF and Bu_4NX with X = F and/or OH).

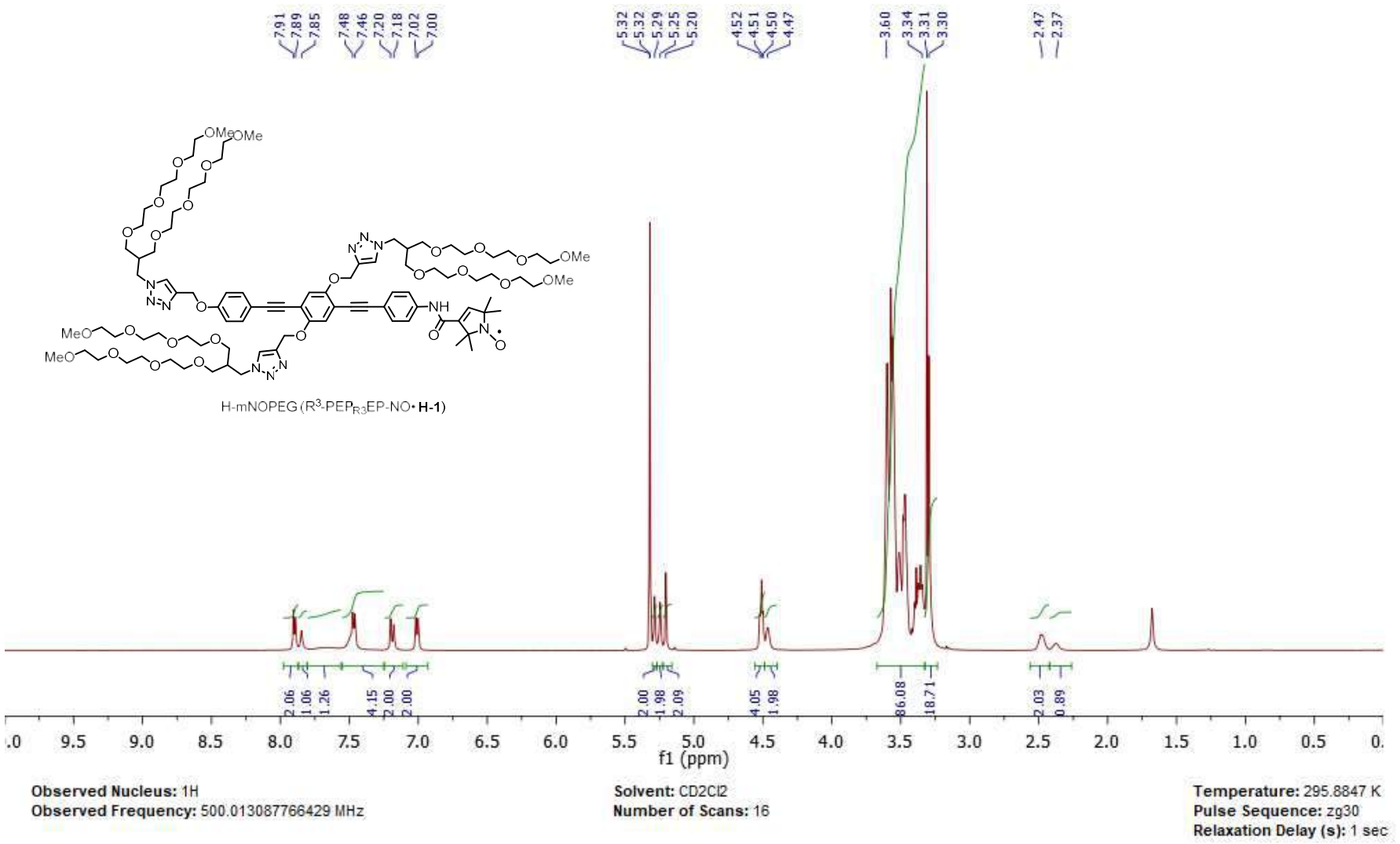

Figure Sb9a. ^{1}H NMR spectrum of H-mNOPEG (R^3-$PEP_{R3}EP$-NO• **H-1**) in CD_2Cl_2.

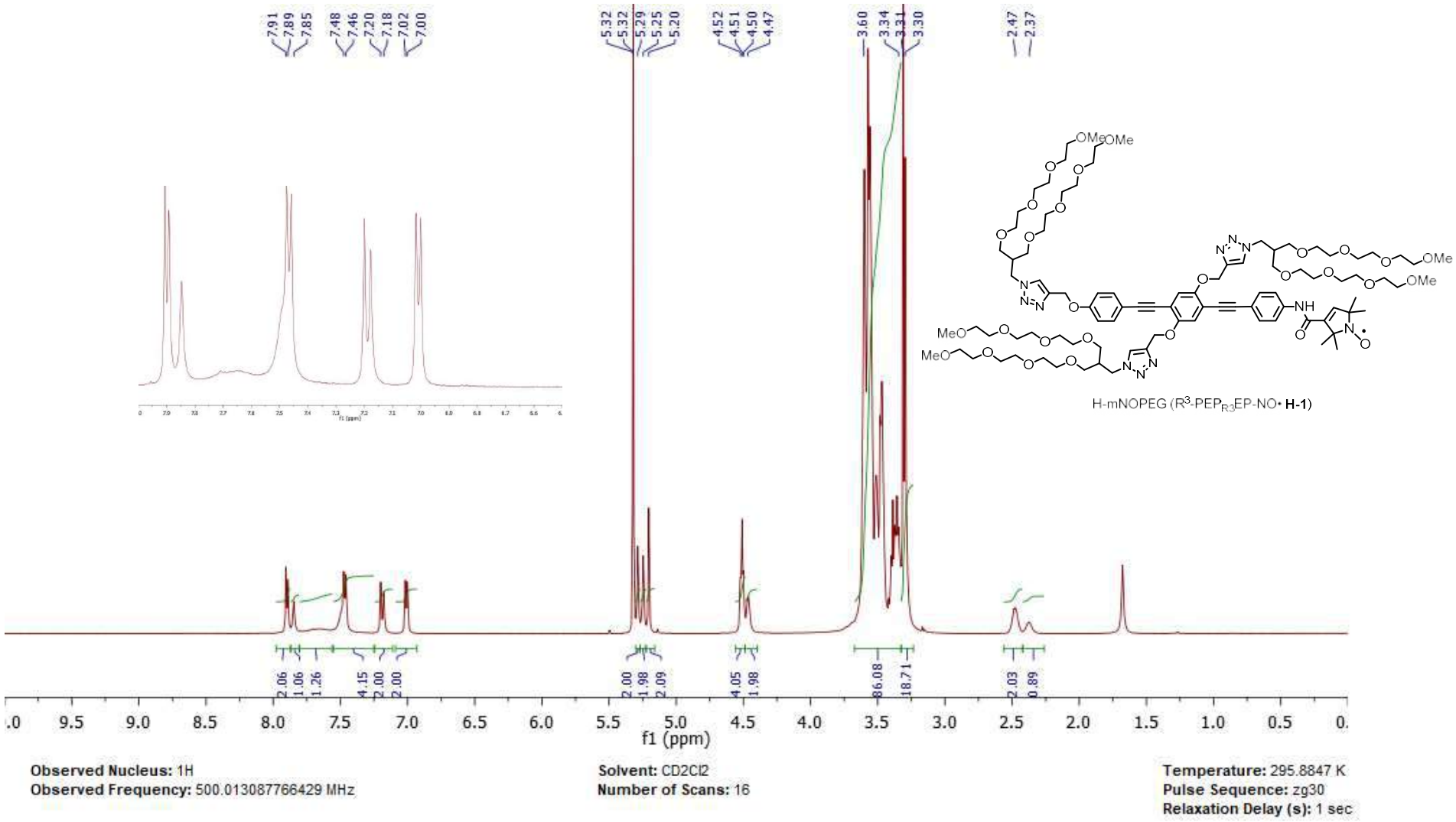

Figure Sb9b. ^{1}H NMR spectrum of H-mNOPEG (R^3-$PEP_{R3}EP$-NO• **H-1**) in CD_2Cl_2.

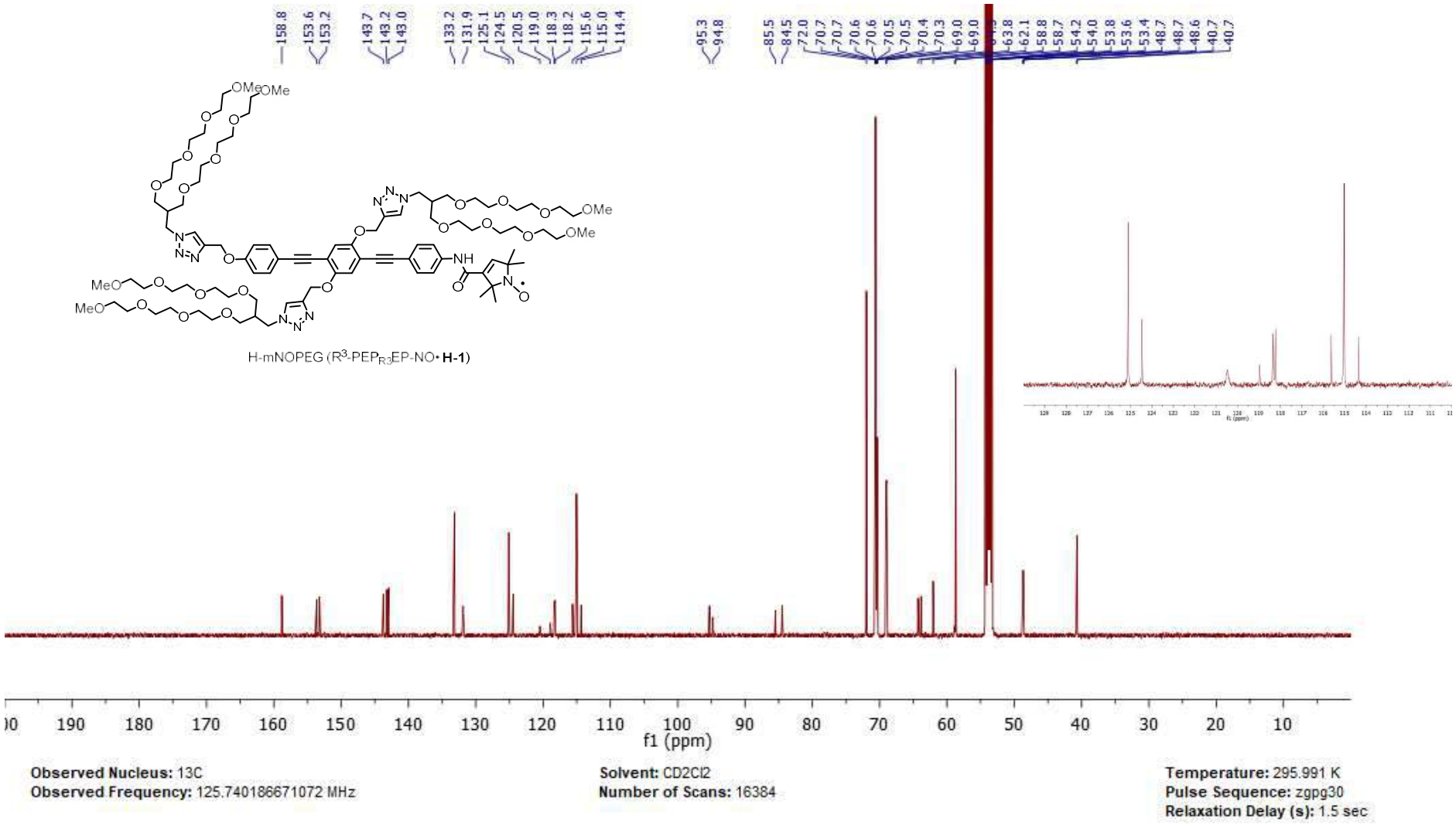

Figure Sb9c. ^{13}C NMR spectrum of H-mNOPEG (R^3-$PEP_{R3}EP$-NO• **H-1**) in CD_2Cl_2.

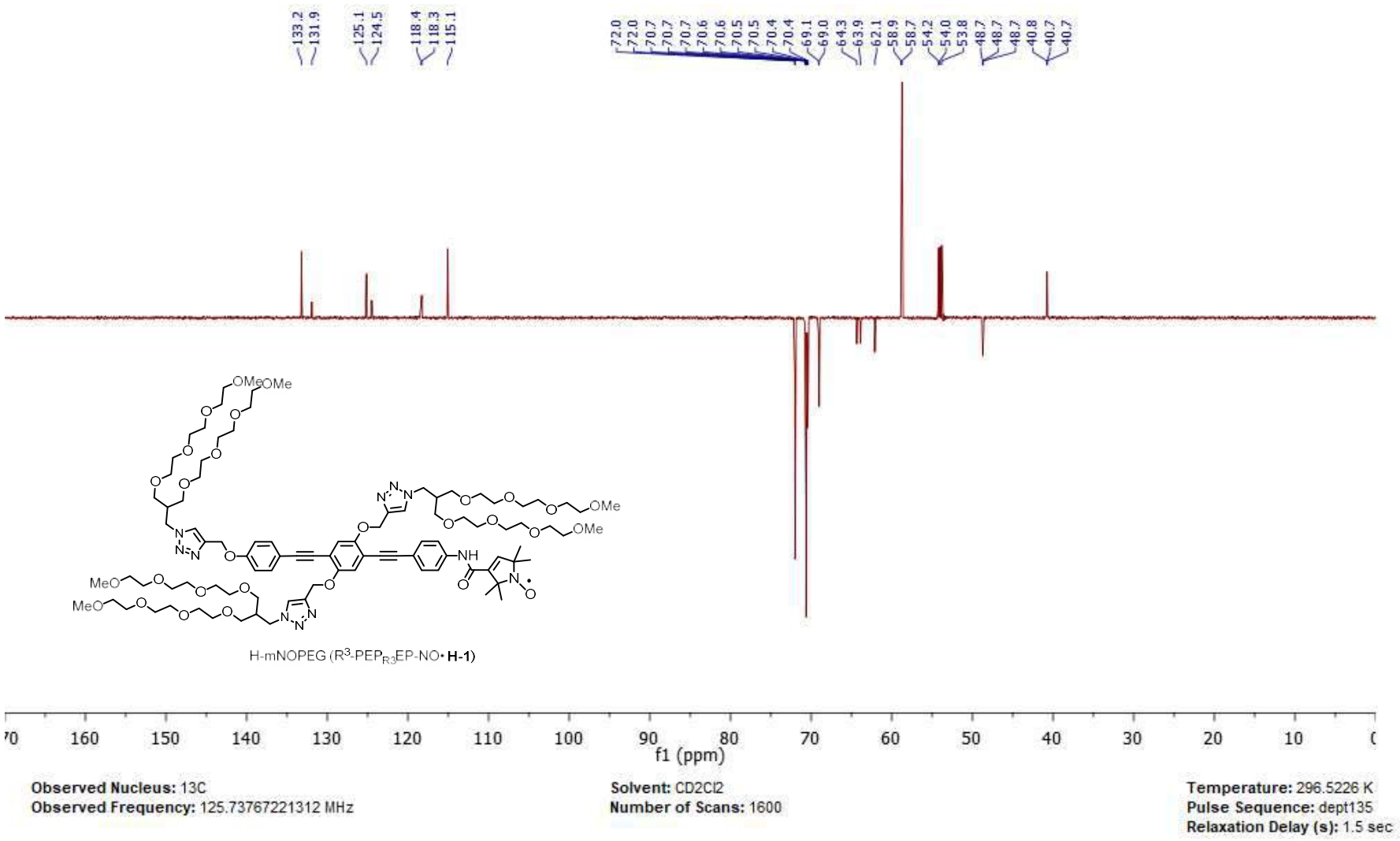

Figure Sb9d. ^{13}C DEPT-135 NMR spectrum of H-mNOPEG (R^3-$PEP_{R3}EP$-NO• **H-1**) in CD_2Cl_2.

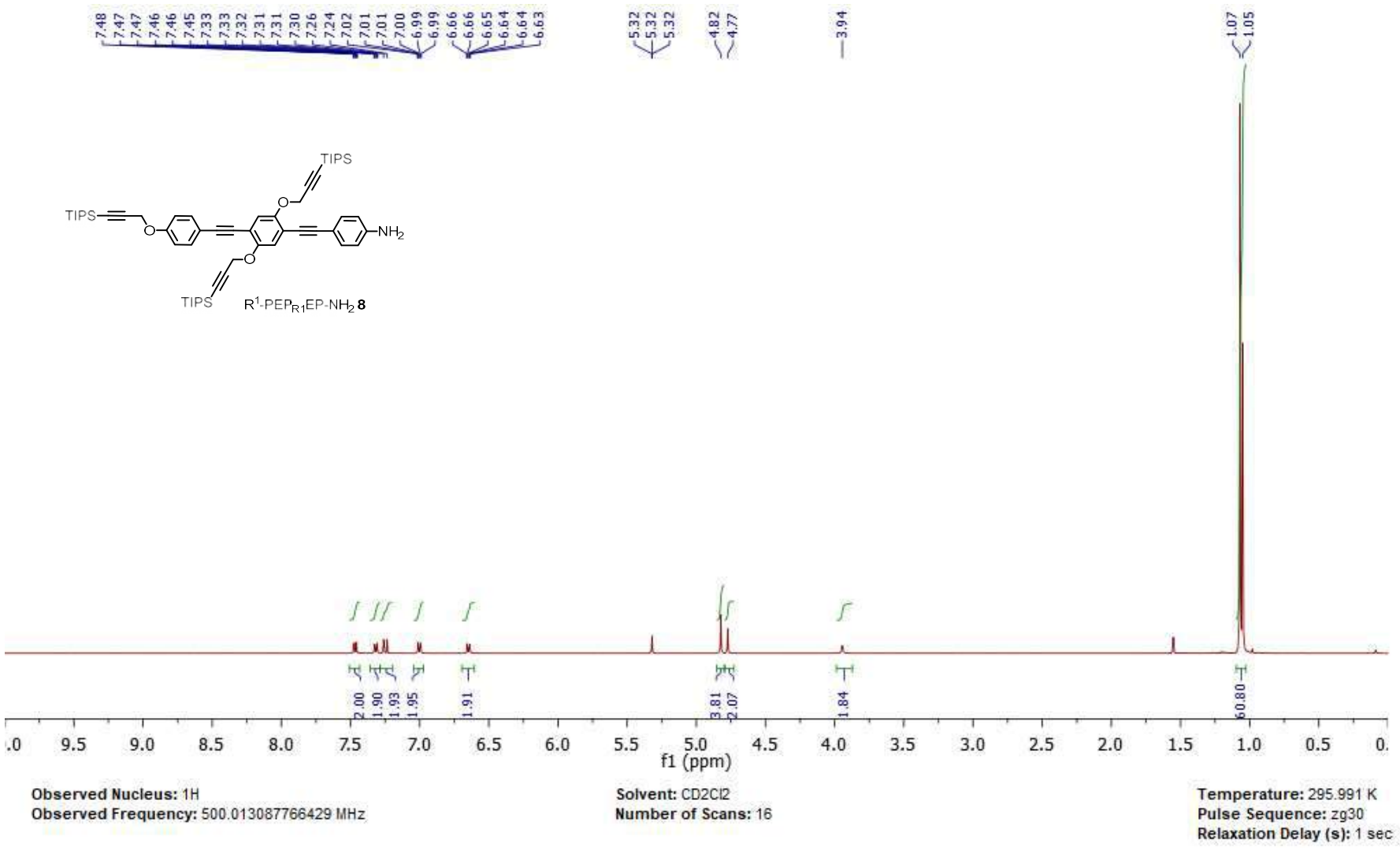

Figure Sb10a. ^{1}H NMR spectrum of R^{1}-PEP$_{R1}$EP-NH$_2$ **8** in CD_2Cl_2.

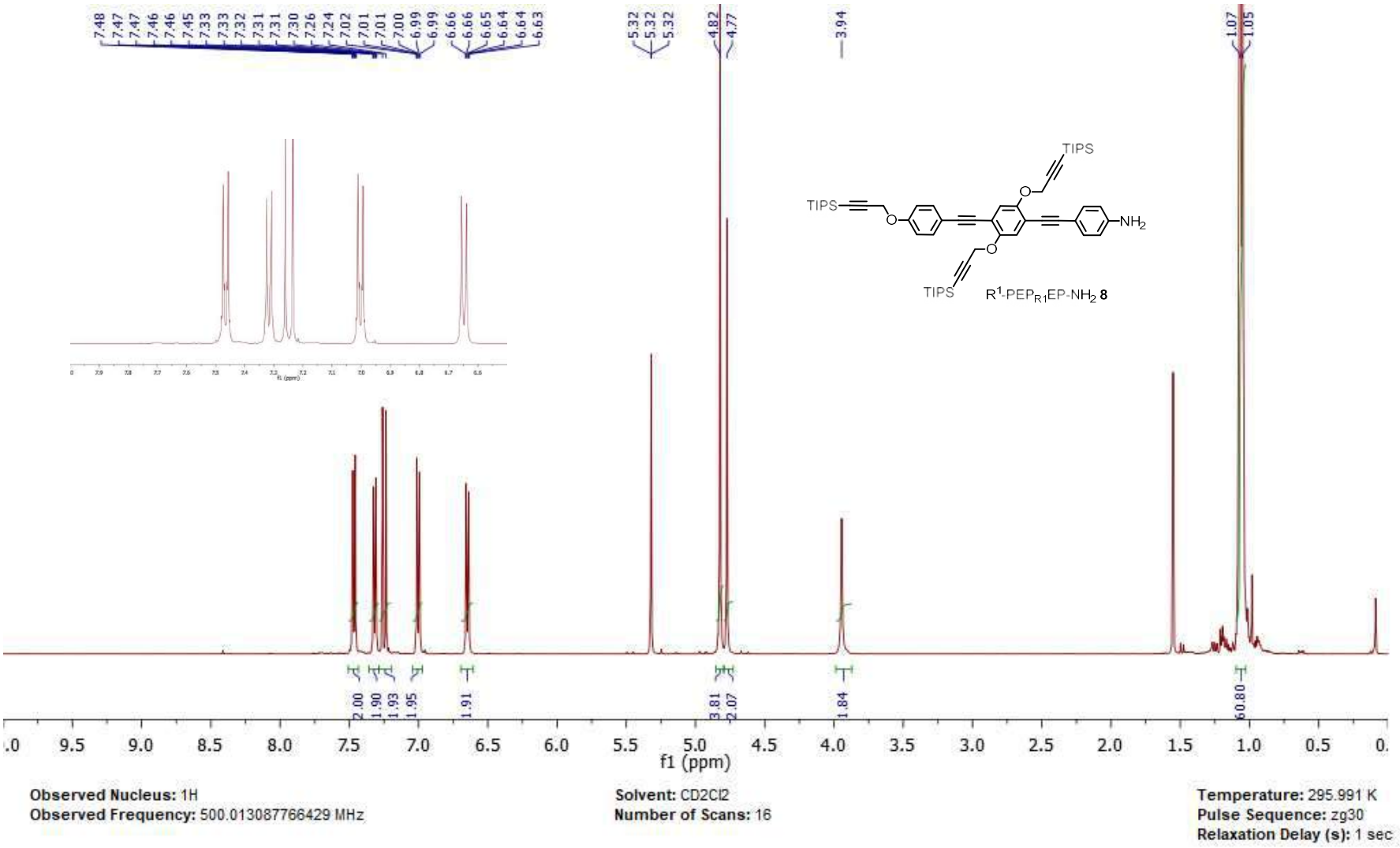

Figure Sb10b. ^{1}H NMR spectrum of R^{1}-PEP$_{R1}$EP-NH$_2$ **8** in CD_2Cl_2.

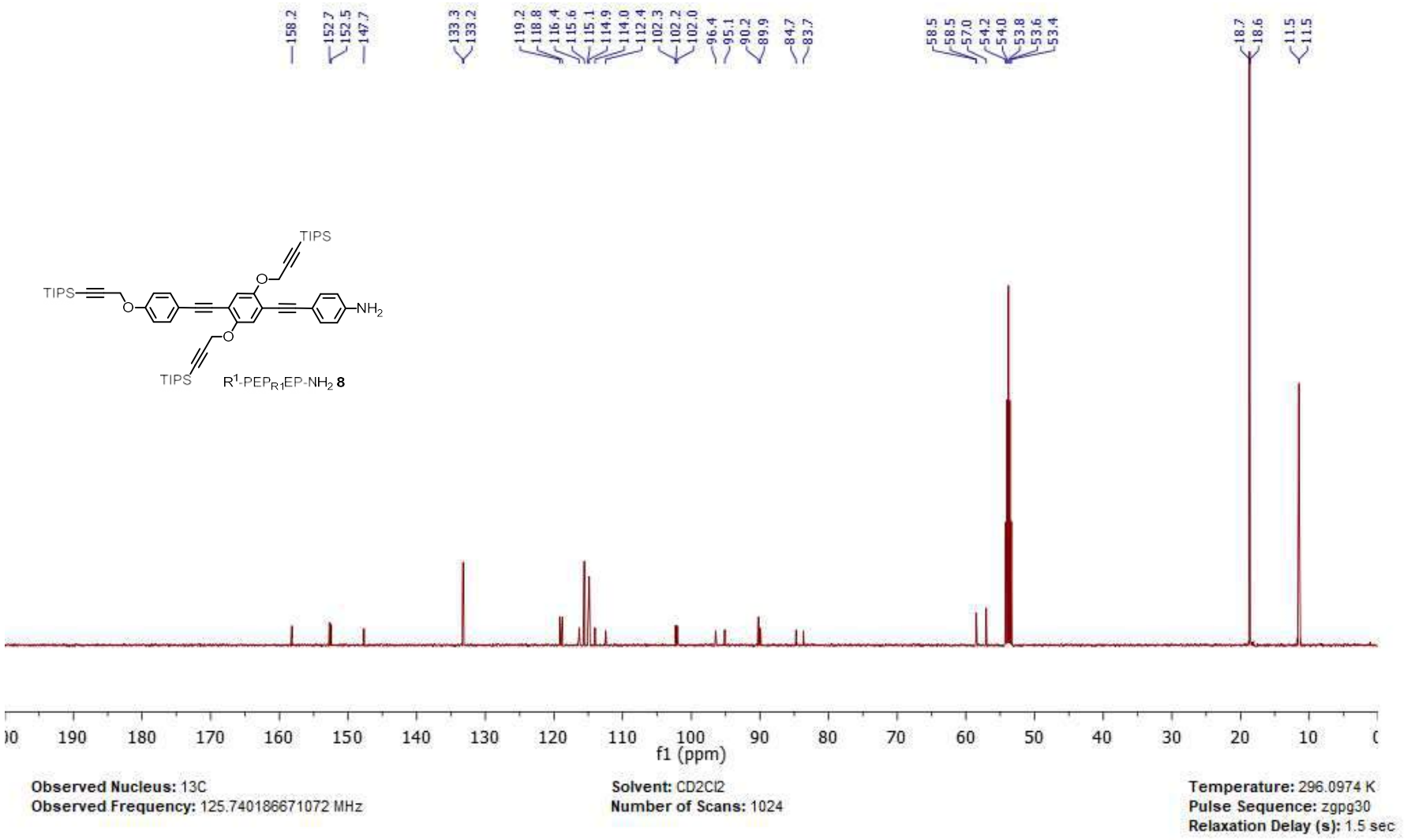

Figure Sb10c. ^{13}C NMR spectrum of R^1-PEP$_{R1}$EP-NH$_2$ **8** in CD_2Cl_2.

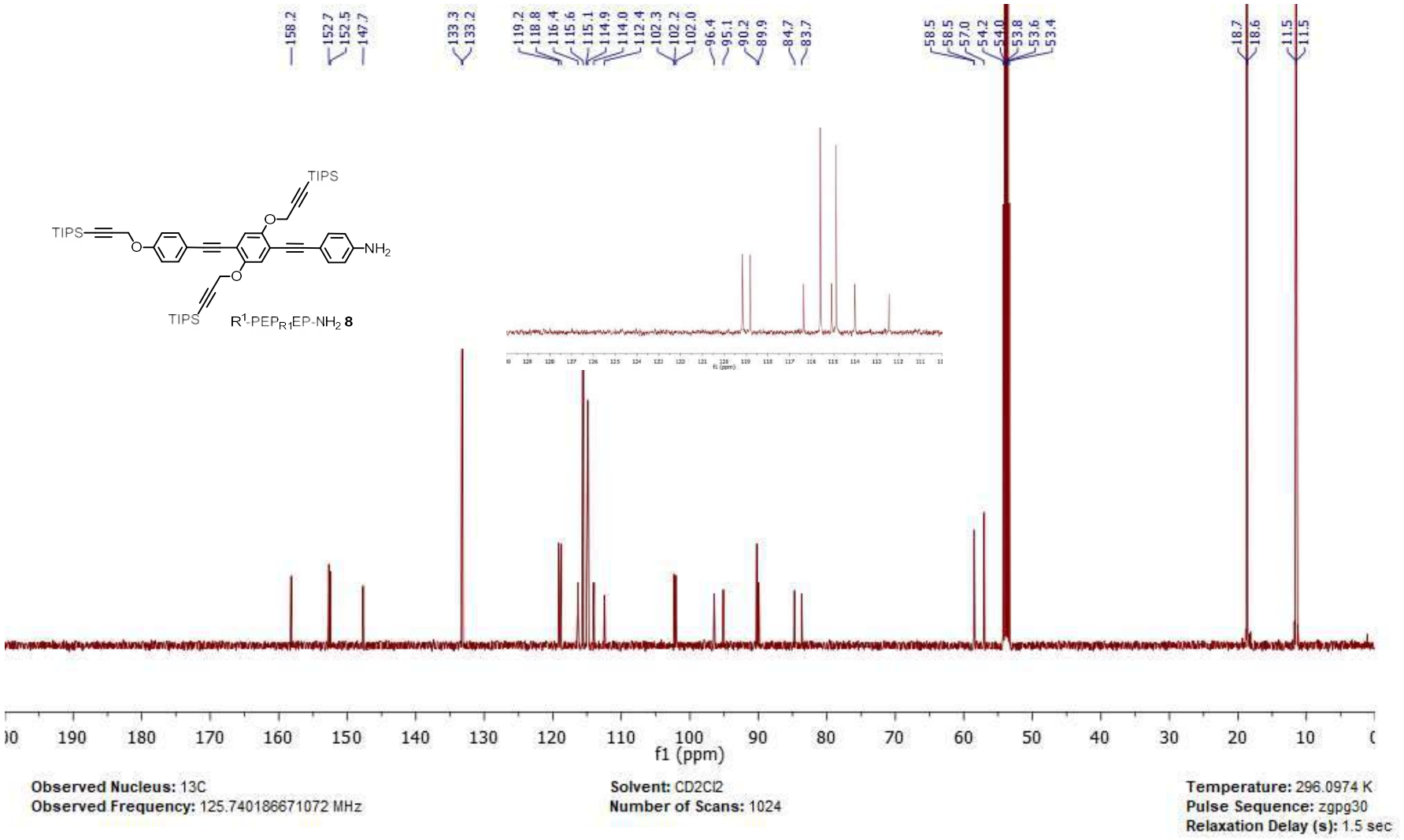

Figure Sb10d. ^{13}C NMR spectrum of R^1-$PEP_{R1}EP$-NH_2 **8** in CD_2Cl_2.

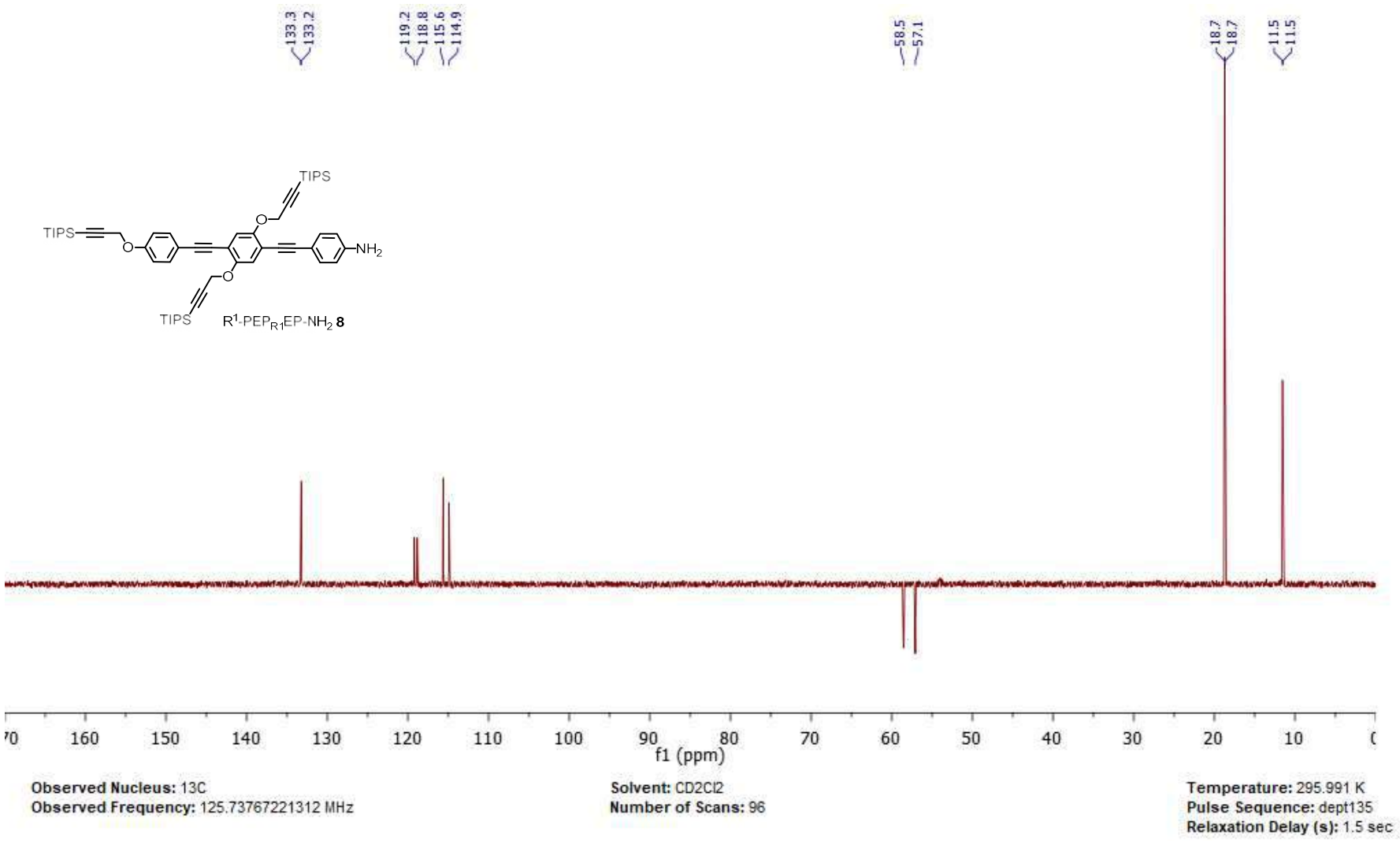

Figure Sb10e. ^{13}C DEPT-135 NMR spectrum of R^1-$PEP_{R1}EP$-NH_2 **8** in CD_2Cl_2.

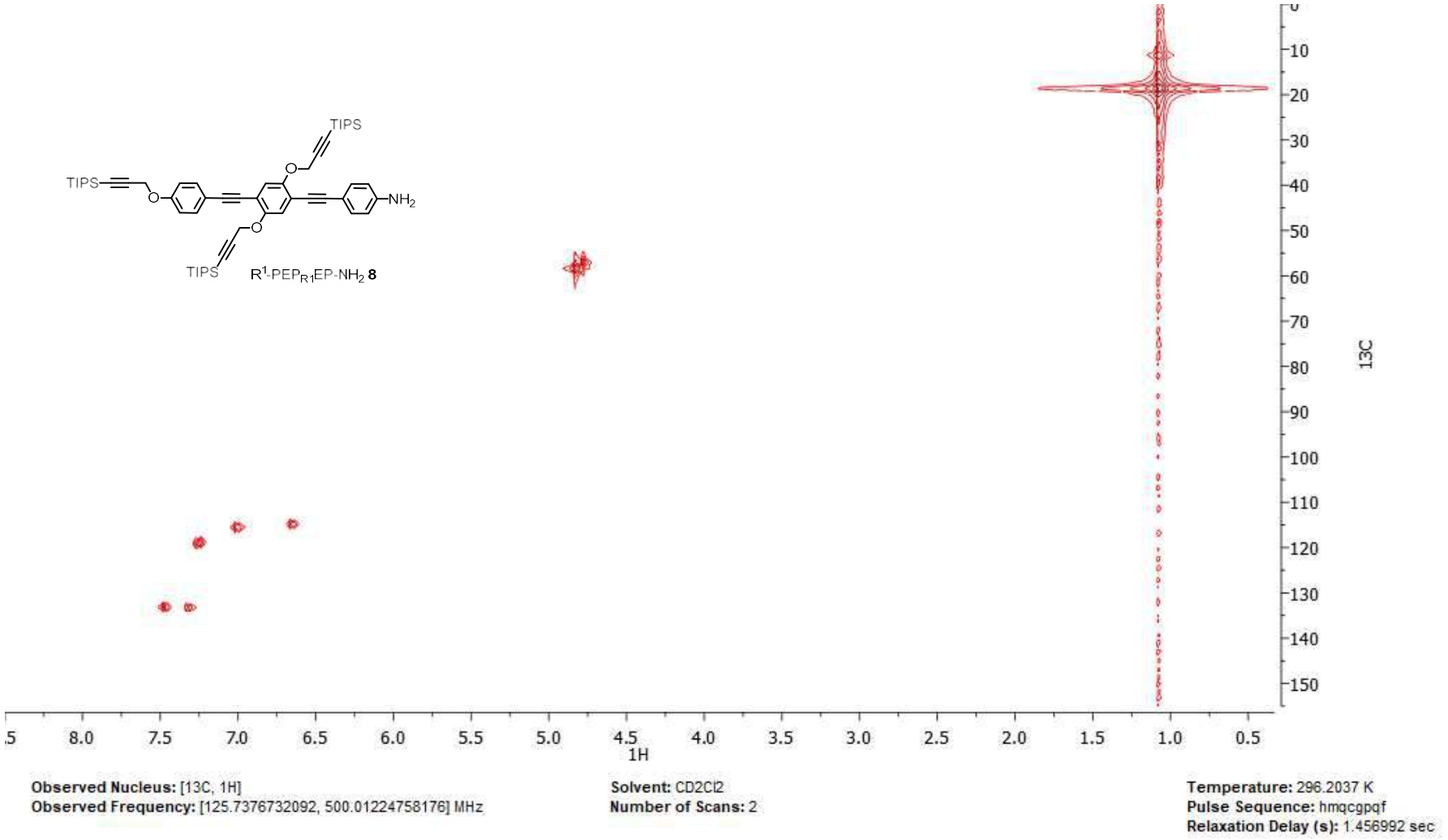

Figure Sb10f. HMQC NMR spectrum of R^1-$PEP_{R1}EP$-NH_2 **8** in CD_2Cl_2.

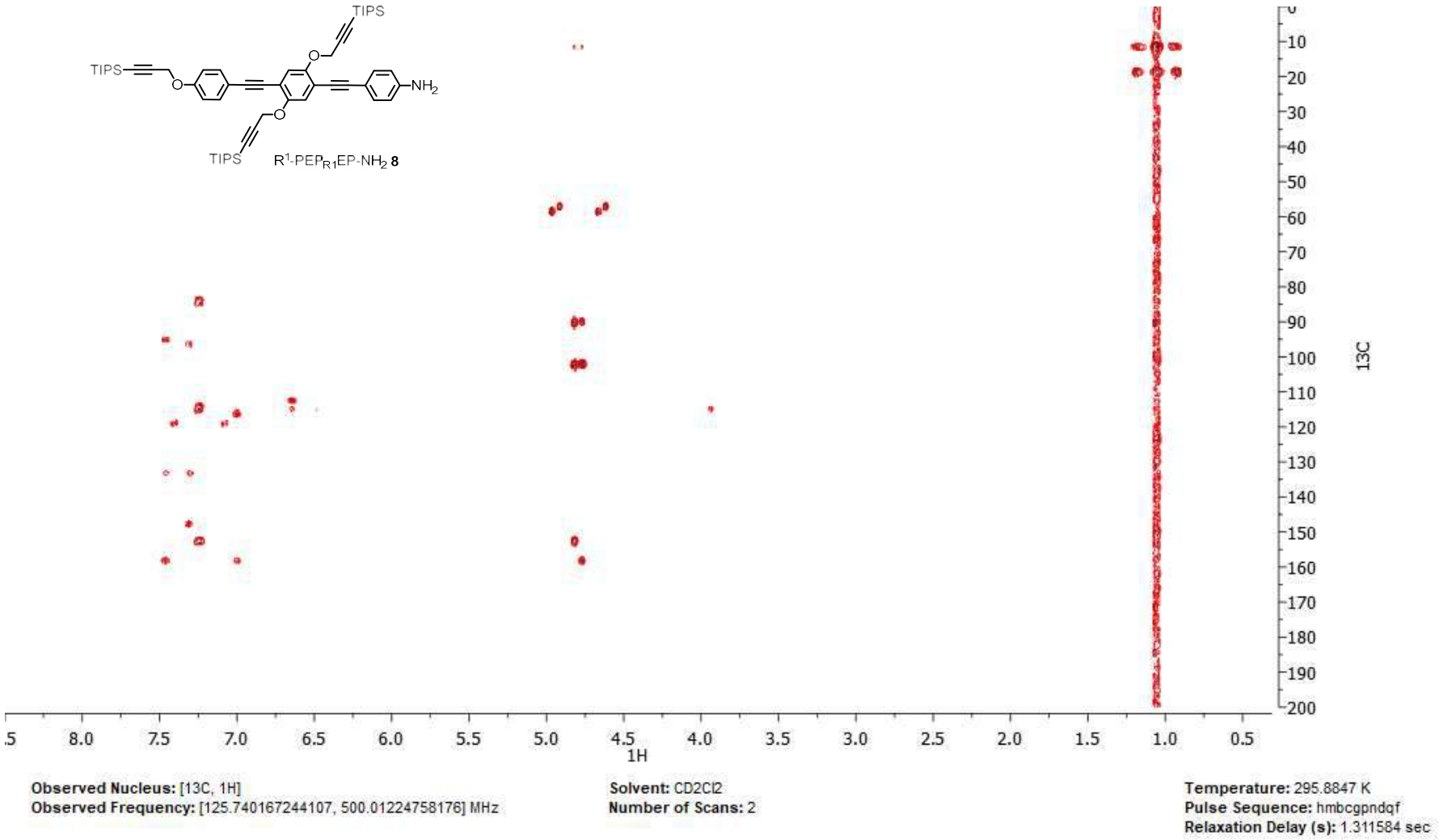

Figure Sb10g. HMBC NMR spectrum of R^1-$PEP_{R1}EP$-NH_2 **8** in CD_2Cl_2.

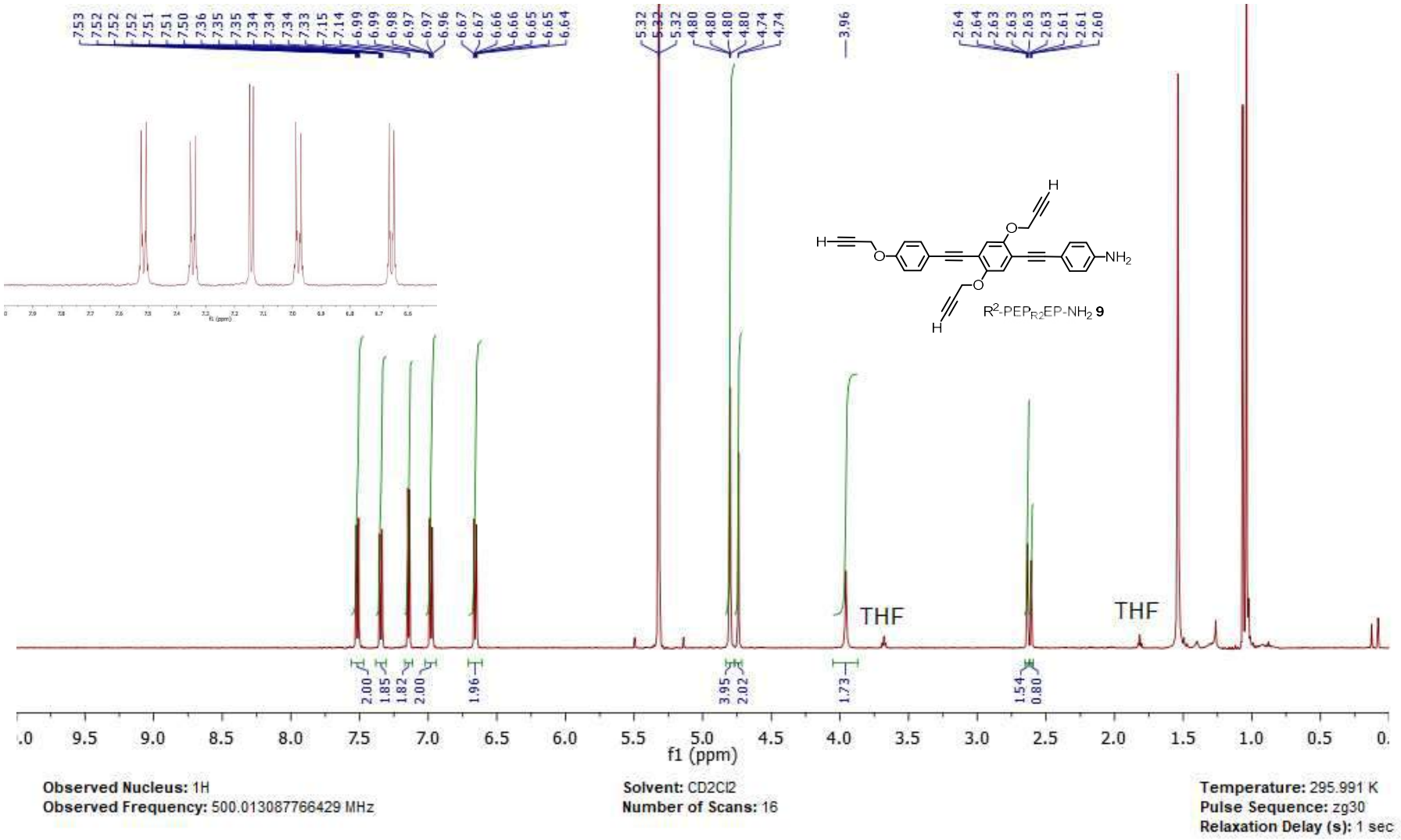

Figure Sb11. ^{1}H NMR spectrum of R^2-$PEP_{R2}EP$-NH_2 **9** in CD_2Cl_2.

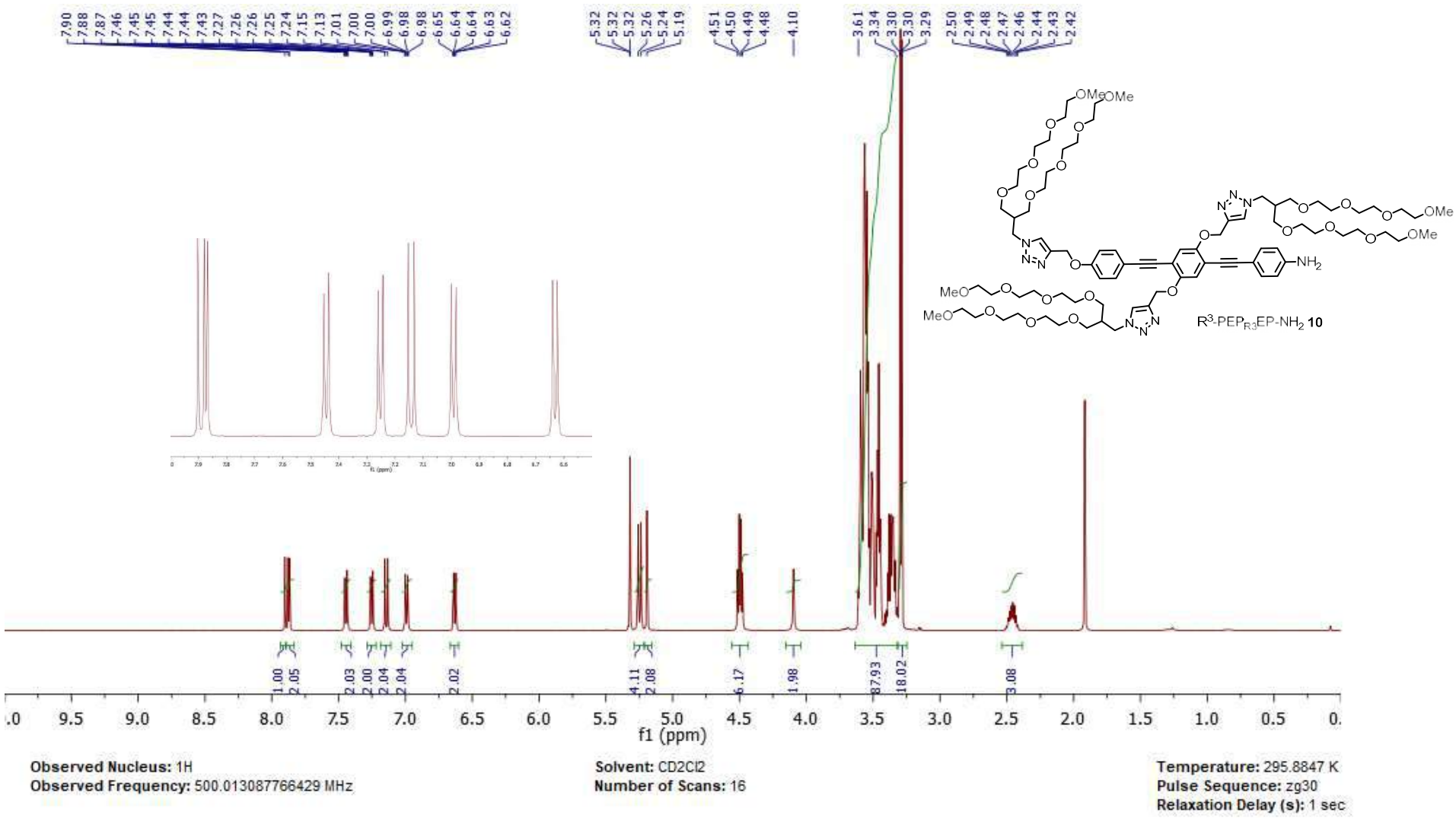

Figure Sb12a. ^{1}H NMR spectrum of R^{3}-PEP$_{R3}$EP-NH$_2$ **10** in CD_2Cl_2.

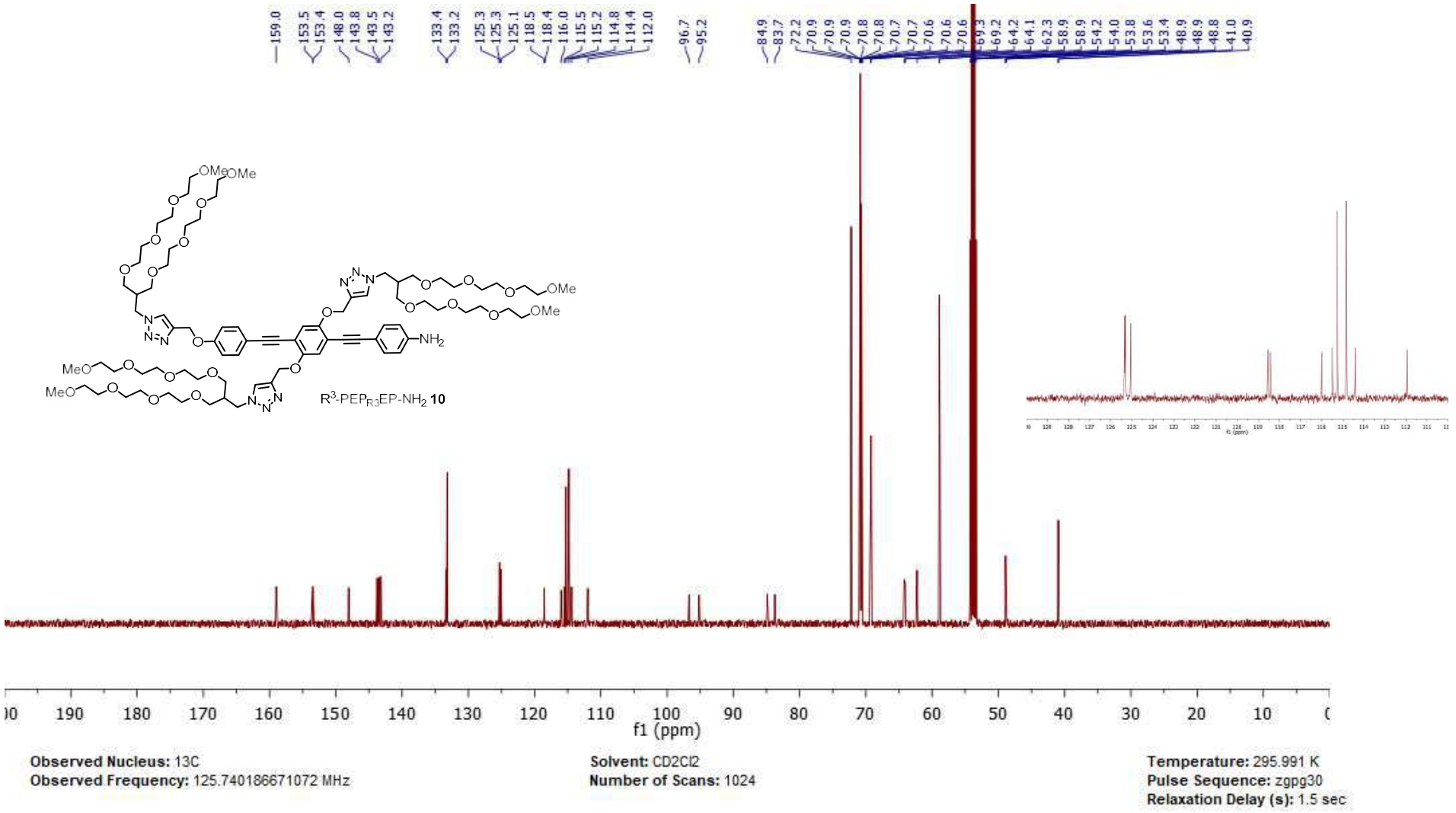

Figure Sb12b. ^{13}C NMR spectrum of R^3-$PEP_{R3}EP$-NH_2 **10** in CD_2Cl_2.

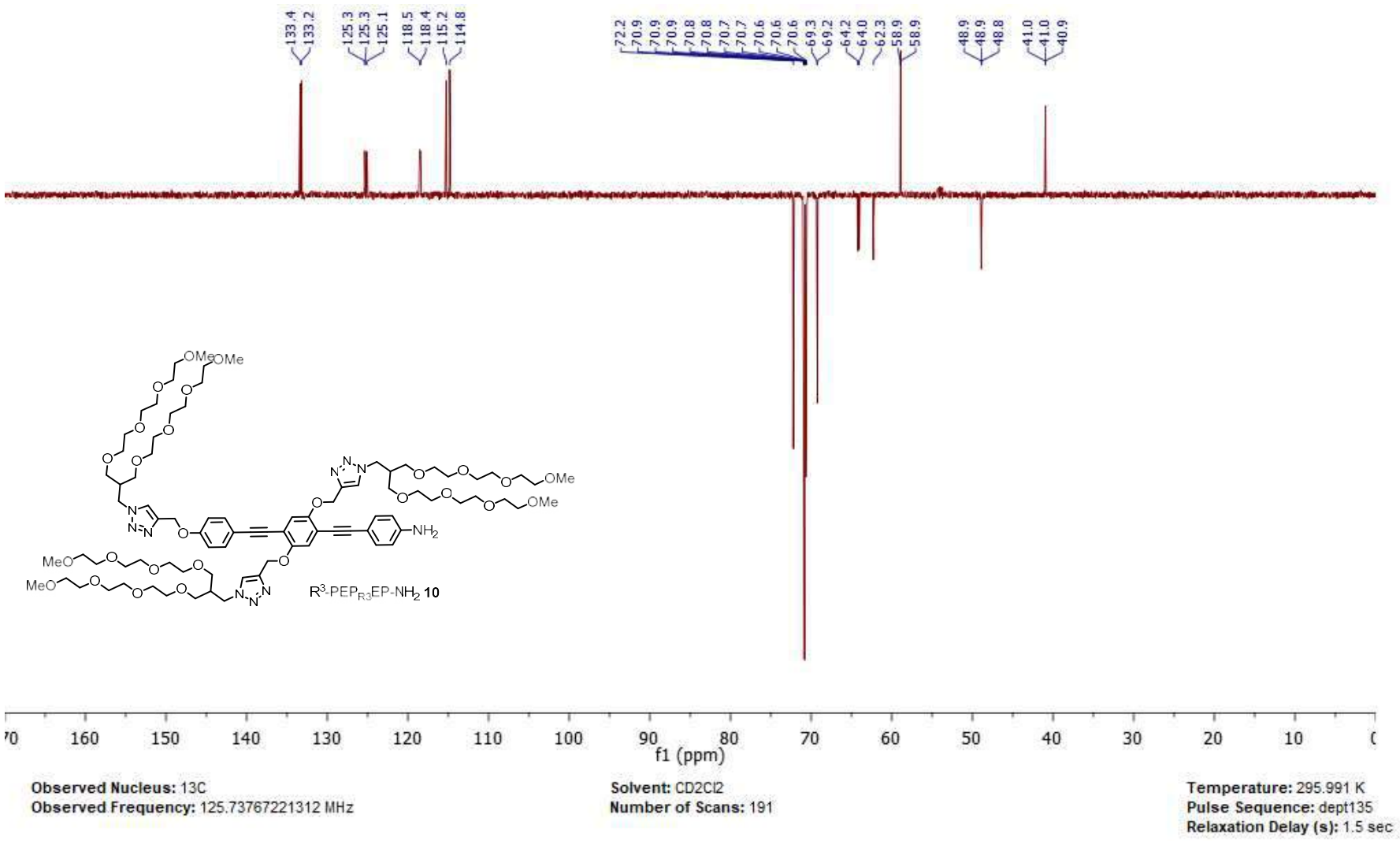

Figure Sb12c. ^{13}C DEPT-135 NMR spectrum of R^3-$PEP_{R3}EP$-NH_2 **10** in CD_2Cl_2.

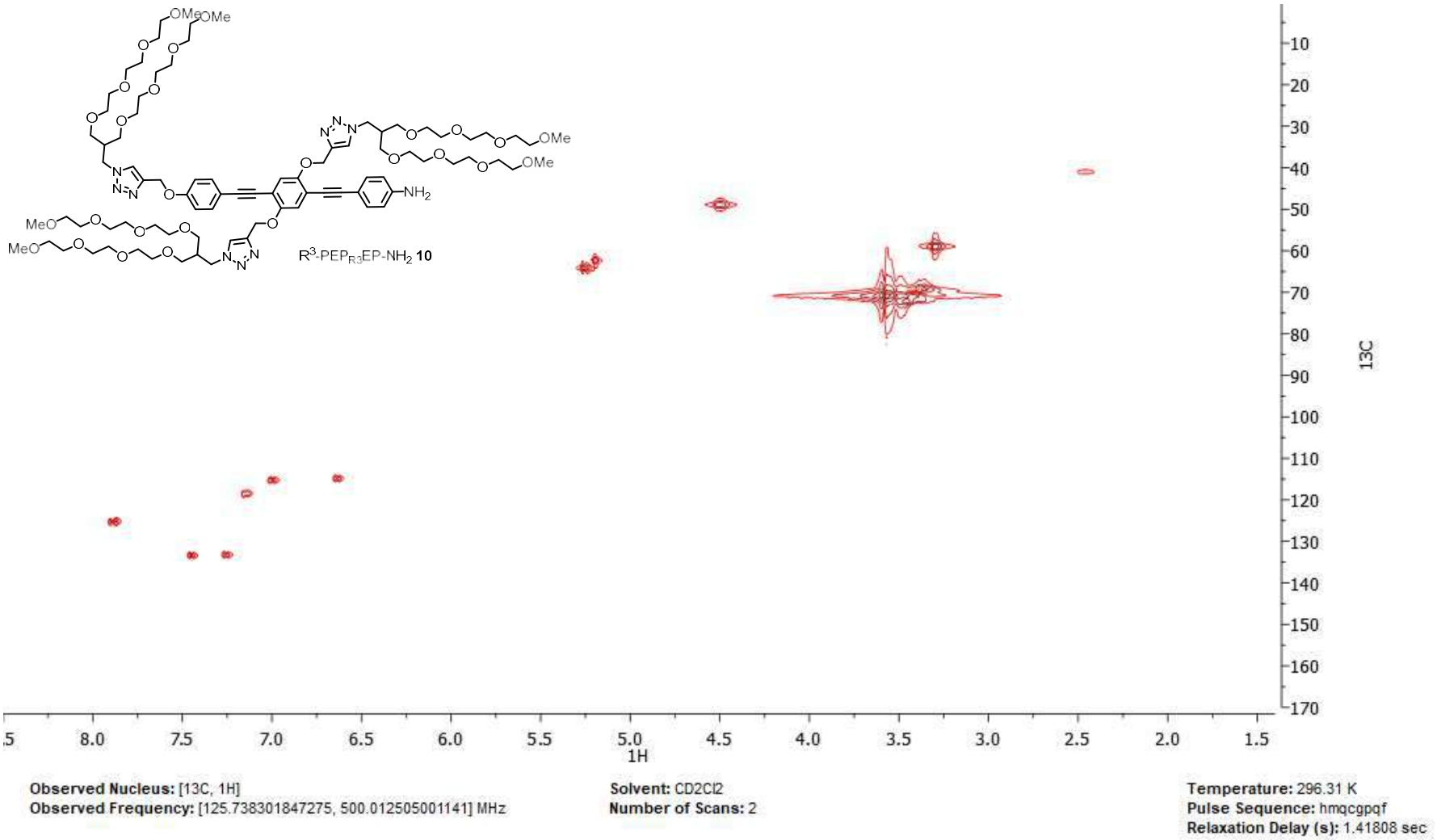

Figure Sb12d. HMQC NMR spectrum of R^3-$PEP_{R3}EP$-NH_2 **10** in CD_2Cl_2.

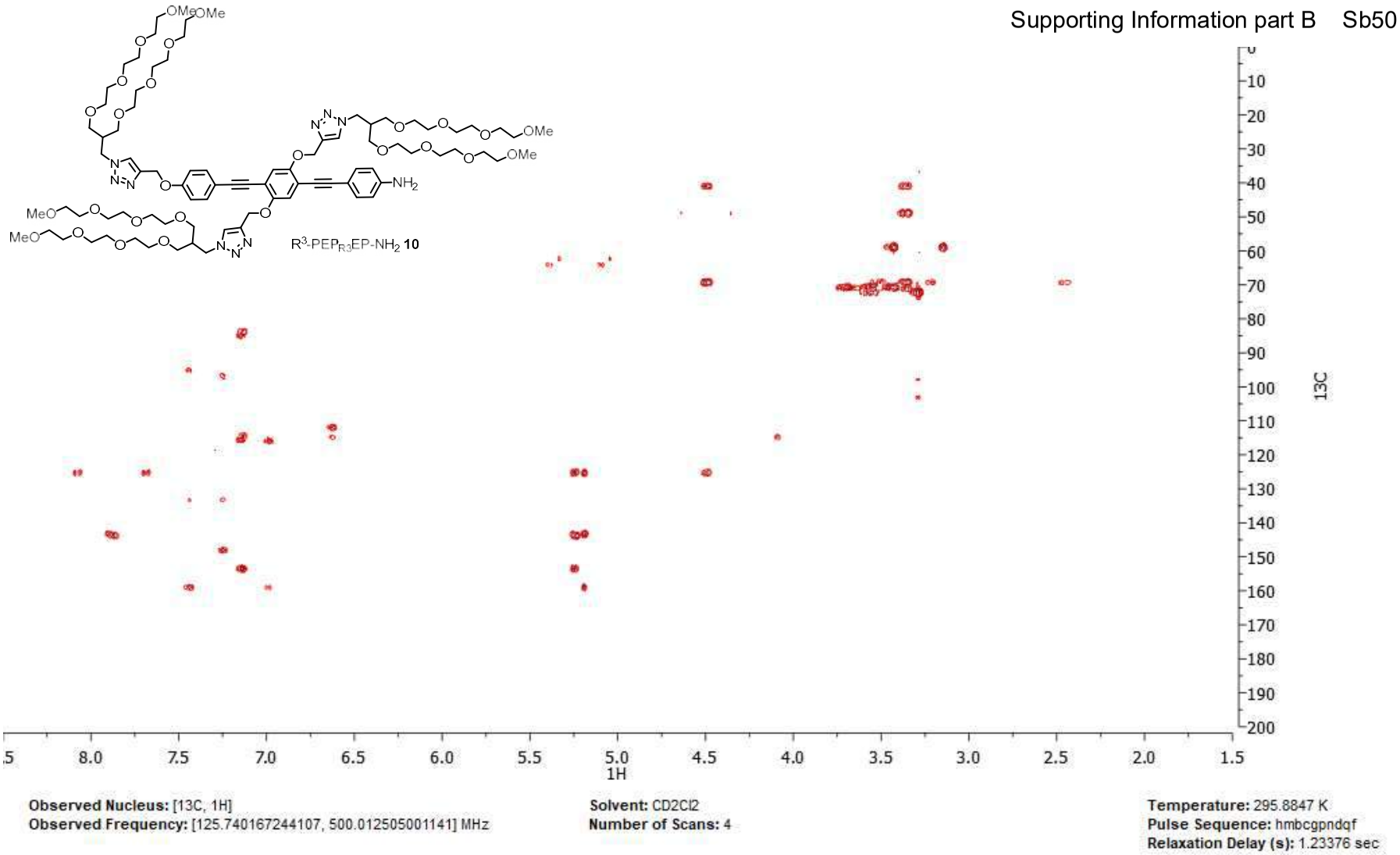

Figure Sb12e. HMBC NMR spectrum of R^3-$PEP_{R3}EP$-NH_2 **10** in CD_2Cl_2.

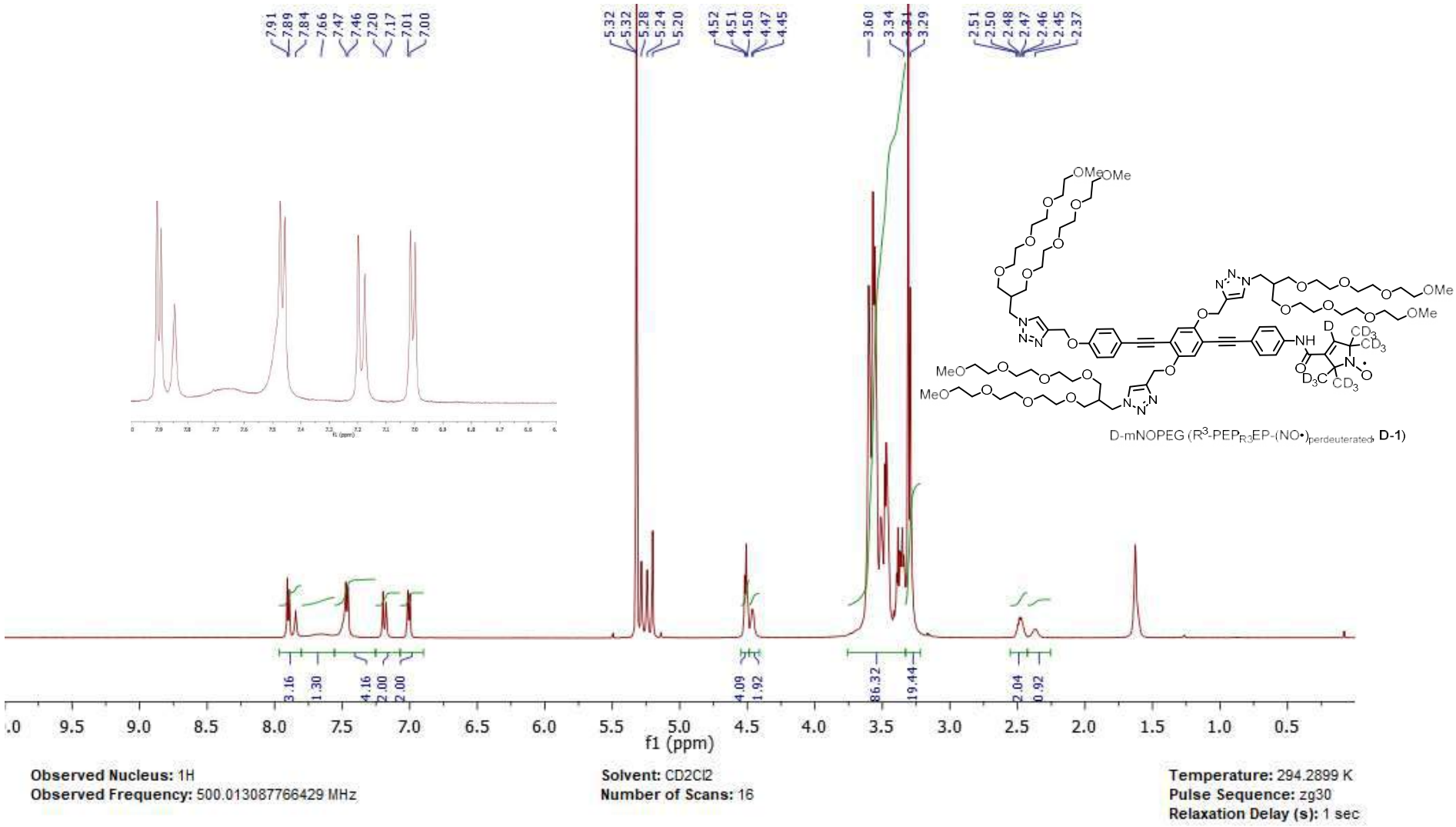

Figure Sb13. ^{1}H NMR spectrum of D-mNOPEG (R^3-$PEP_{R3}EP$-$(NO\bullet)_{perdeuterated}$, **D-1**) in CD_2Cl_2.